A Generalized Orthotropic Elasto-Plastic

Material Model for Impact Analysis

by

Canio Hoffarth

A Dissertation Presented in Partial Fulfillment
of the Requirements for the Degree
Doctor of Philosophy

Approved August 2016 by the
Graduate Supervisory Committee:

Subramaniam Rajan, Chair
Robert Goldberg
Narayanan Neithalath
Barzin Mobasher
Yongming Liu

ARIZONA STATE UNIVERSITY

December 2016

ABSTRACT

Composite materials are now beginning to provide uses hitherto reserved for metals in structural systems such as airframes and engine containment systems, wraps for repair and rehabilitation, and ballistic/blast mitigation systems. These structural systems are often subjected to impact loads and there is a pressing need for accurate prediction of deformation, damage and failure. There are numerous material models that have been developed to analyze the dynamic impact response of polymer matrix composites. However, there are key features that are missing in those models that prevent them from providing accurate predictive capabilities. In this dissertation, a general purpose orthotropic elasto-plastic computational constitutive material model has been developed to predict the response of composites subjected to high velocity impacts. The constitutive model is divided into three components – deformation model, damage model and failure model, with failure to be added at a later date. The deformation model generalizes the Tsai-Wu failure criteria and extends it using a strain-hardening-based orthotropic yield function with a non-associative flow rule. A strain equivalent formulation is utilized in the damage model that permits plastic and damage calculations to be uncoupled and capture the nonlinear unloading and local softening of the stress-strain response. A diagonal damage tensor is defined to account for the directionally dependent variation of damage. However, in composites it has been found that loading in one direction can lead to damage in multiple coordinate directions. To account for this phenomena, the terms in the damage matrix are semi-coupled such that the damage in a particular coordinate direction is a function of the stresses and plastic strains in all of the coordinate directions. The overall framework is driven by experimental tabulated temperature and rate-

dependent stress-strain data as well as data that characterizes the damage matrix and failure. The developed theory has been implemented in a commercial explicit finite element analysis code, LS-DYNA®, as MAT213. Several verification and validation tests using a commonly available carbon-fiber composite, Toyobo's T800/F3900, have been carried and the results show that the theory and implementation are efficient, robust and accurate.

DEDICATION

To my family and friends, especially my parents, Mike and Yolanda Hoffarth, for all of

their love and support that helped me throughout my studies.

ACKNOWLEDGMENTS

TABLE OF CONTENTS

LIST OF TABLES

Table   Page

LIST OF FIGURES

NOMENCLATURE

$\mathbf{C}$ = elastic stiffness matrix;

$f(\sigma)$ = yield function with respect to the stress state;

F_k = coefficients in vector portion of yield function;

F_{ij} = coefficients in tensor portion of yield function;

h = plastic potential function;

$\left.\dfrac{\partial h}{\partial \boldsymbol{\sigma}}\right|_{n+1}^{i}$ = gradient of plastic potential function for iteration i of time step $n+1$;

H_{ij} = constant coefficients of plastic potential function;

$\mathbf{q}$ = vector of yield stresses in various coordinate directions;

$\mathbf{q}_{n+1}^{i+1}$ = vector of yield stresses for iteration $i+1$ of time step $n+1$;

$\dot{W}^{p}$ = plastic work rate;

$\Delta\boldsymbol{\varepsilon}$ = strain increment tensor;

$\boldsymbol{\sigma}$ = stress tensor;

$\boldsymbol{\sigma}_n$ = stress tensor at time step n;

$\boldsymbol{\sigma}_{n+1}^{i+1}$ = stress tensor for iteration $i+1$ at time step $n+1$;

σ_e = effective stress;

σ_{ij} = stress components;

σ_{ij}^{c} = compressive yield stresses;

σ_{ij}^{t} = tensile yield stresses;

$\sigma_{ij}'^{45}$ = yield stress from 45° off-axis test in i-j plane;

v_{ij} = elastic Poisson's ratio in ij direction;

v_{ij}^{p} = plastic Poisson's ratio in ij direction;

$\mathbf{d}$ = deformation rate tensor;

d_{ij} = deformation rate components;

$\mathbf{M}$ = damage tensor;

M_{ij} = damage components;

$\boldsymbol{\sigma}_{eff}$ = undamaged (effective) stress tensor;

σ_{ij}^{eff} = undamaged (effective) stress components;

$\varepsilon_{i\text{-}j}^{45}$ = yield strain from 45° test in *i-j* plane;

$\dot{\boldsymbol{\varepsilon}}^{p}$ = plastic strain rate tensor;

$\dot{\varepsilon}_{e}^{p}$ = effective plastic strain rate;

$d\varepsilon_{e}^{p}$ = increment of effective plastic strain;

$\dot{\varepsilon}_{ij}^{p}$ = components of plastic strain rate;

$d\varepsilon_{ij}^{p}$ = components of increments of plastic strain;

$\dot{\lambda}$ = scalar plastic multiplier equal to effective plastic strain rate;

λ_{n} = effective plastic strain for time step *n*;

$\Delta\lambda_{n+1}^{i+1}$ = increment of effective plastic strain for iteration *i+1* of time step *n+1*;

E_{ii} = elastic modulus in the *ii* direction;

G_{ij} = elastic shear modulus in the *i-j* plane;

E_{ii}^{djj} = elastic modulus in the *ii* direction due to damage from loading in the *jj* direction;

A_{ii}^{djj} = effective area in the *i-i* plane due to damage from loading in the *jj* direction;

d_{ij}^{kl} = damage in the *kl* direction due to loading along *ij*;

E_{ii}^{eff} = effective (undamaged) elastic modulus in the *ii* direction;

G_{ij}^{eff} = effective (undamaged) elastic shear modulus in the *ij* direction;

$\hat{\mathbf{d}}$ = vector of damage parameters;

$\hat{\mathbf{d}}_{n+1}$ = vector of damage parameters at time step *n+1*;

Chapter 1: Introduction

Composite materials are now beginning to provide uses hitherto reserved for
metals in structural systems such as airframes and engine containment systems, wraps for
repair and rehabilitation, and ballistic/blast mitigation systems. While material models
exist that can be used to simulate the response of a variety of materials in these
demanding structural applications under impact conditions, the more mature material
models have focused on simulating the response of standard materials such as metals (
(Moreira and Ferron 2007), (Ganjiani, Naghdabadi and Asghari 2012), (Buyuk 2014)),
elastomers (Bergstrom 2005) and wood (Tabiei and Wu 2000). A conceptual diagram
showing the constituent parts of a general composite material model is shown in Fig. 1.
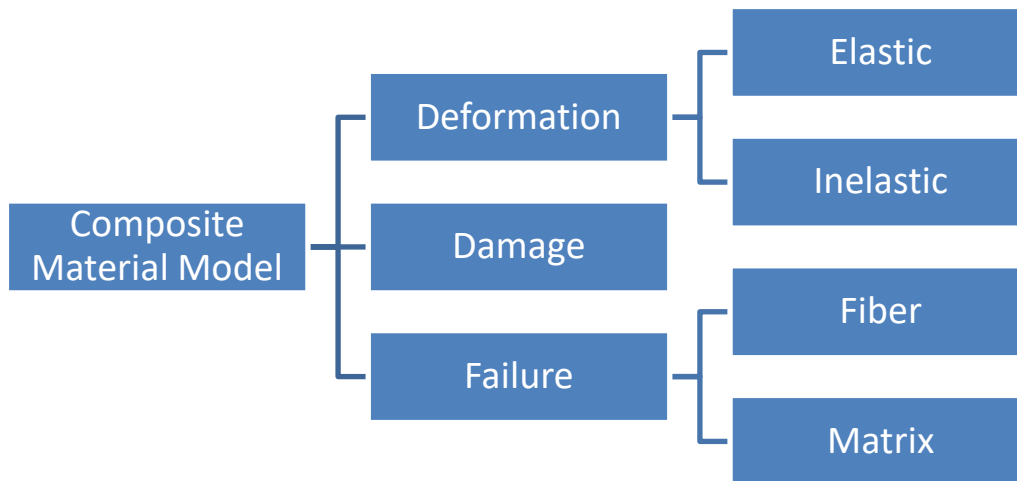
Fig. 1. Components of a General Fiber-Reinforced Composite Material Model

The use of composites in aerospace applications requires an emphasis on the capabilities
of a material model to handle impact analysis in a finite element analysis software, such

as LS-DYNA®, ABAQUS®, ANSYS®, etc. This work focuses on implementation of composite impact modeling in LS-DYNA.

LS-DYNA Composite Material Models: Commercial finite element programs support a variety of material models for the analysis of composites. For example, LS-DYNA® (Hallquist 2013) currently contains several material models. However, the models are tailored specifically for a class of applications and have limitations - purely elastic, no rate sensitivity, implementation for solid elements only, limited damage and failure characterization, etc. Details are shown in Table 1.

Table 1. Summary of LS-DYNA® Composite Material Models

Material ID	Composite Architecture	Damage	Failure	Element Type	Rate sensitivity
MAT_22	Orthotropic	No damage	Brittle failure, Chang-Chang (Chang and Chang 1987b)	Solids and Shells	None
MAT_54	Arbitrary orthotropic (unidirectional layers)	Includes damage	Tension: Chang-Chang (Chang and Chang 1987b) Compression: Matzenmiller et al. (Matzenmiller, Lubliner and Taylor 1995)	Thin shells only	None
MAT_55	Arbitrary orthotropic (unidirectional layers)	Includes damage	Tension: Tsai-Wu (Tsai and Wu 1971) Compression: Matzenmiller et al. (Matzenmiller, Lubliner and Taylor 1995)	Thin shells only	None
MAT_58	Orthotropic (unidirectional	Includes damage	Includes failure	Shells and	None

	layers, complete laminates, woven fabrics)	(Matzenmiller et al. (Matzenmiller, Lubliner and Taylor 1995))		thick shells	
MAT_59	Orthotropic	Includes damage	Includes failure	Solids and shells	None
MAT_116	Composite layups	No damage	No failure	Shells only	None
MAT_117	Composite layups	No damage	No failure	Shells only	None
MAT_118	Composite layups	No damage	No failure	Shells only	None
MAT_158	Orthotropic (unidirectional layers, complete laminates, woven fabrics)	Includes damage	Includes failure (Matzenmiller et al. (Matzenmiller, Lubliner and Taylor 1995))	Shells and thick shells only	Includes rate effects (viscous stress tensor)
MAT_161 /162*	Orthotropic (unidirectional and woven fabric layers)	Includes damage	Includes failure (Hashin/ Matzenmiller et al. (Matzenmiller, Lubliner and Taylor 1995))	Solids and shells	Includes rate effects
MAT_219	Orthotropic (fiber reinforced composite laminates with transversely isotropic layers)	Includes damage (CODAM2, (Hallquist 2013))	Includes failure	Solids and shells	None
MAT_221	Orthotropic	Includes damage (simplified; Maire-Chaboche, (Hallquist 2013))	Includes failure	Solids only	None

MAT_223	Orthotropic	Includes damage (advanced; Maire-Chaboche)	Includes failure	Solids only	None
MAT_261	Orthotropic (laminated fiber-reinforced)	Includes damage	Includes failure (Pinho et al. (Pinho, Iannucci and Robinson 2006) , (Pinho, Iannucci and Robinson 2006))	Solids and shells	None
MAT_262	Orthotropic (laminated fiber-reinforced)	Includes damage	Includes failure (Maimi et al. (Maimi, Camanho, et al. 2007), (Maimi, Camanho, et al. 2007))	Solids and shells	None

MAT_22 employs the Chang-Chang failure model (Chang and Chang 1987b) using combinations of different stress to failure strength ratios to predict fiber or matrix based failure. It assumes linear elastic response with brittle failure and has limited nonlinear shear response capabilities. MAT_54/55 is built upon MAT_22 by allowing for a more comprehensive nonlinear response. There is a reduction in the elastic constants of the composite which are selectively modified based on the failure mode. The model can simulate a gradual unloading up to ultimate failure. Unlike MAT_22 and MAT_54, MAT_55 uses the Tsai-Wu failure criterion (Tsai and Wu 1971), with the fiber failure modes the same as the Chang-Chang criteria, but with different matrix failure modes. The continuum damage model developed by Matzenmiller et al. (Matzenmiller, Lubliner and Taylor 1995) is utilized in MAT_58, where the material stress-stain curves are generated based on specified failure stresses and strains of the material in each of the

coordinate directions. Strain rate is not considered, but an adaptation of the material

model, MAT_158, includes strain rate dependence in the material response (Hallquist

2013). The strain rate effect is modeled using a viscous stress tensor based on an

isotropic Maxwell model consisting of up to six terms of a shear moduli Prony series

expansion that is superimposed on the rate independent stress tensor of the composite,

creating an isotropic strain rate effect. MAT_161 utilizes continuum damage mechanics

(Yen 2002) to determine the initiation of fiber or matrix based failure using a stress to

strength ratio in the different coordinate directions. MAT_162 is a generalization of the

failure model in MAT_161. It uses the same damage mechanics approach as in MAT_58

to simulate the nonlinear response following the initiation of damage (Matzenmiller,

Lubliner and Taylor 1995). The UBC Composite Damage Model (CODAM) is

implemented in MAT_219 (Williams, Vaziri and Poursartip 2003). CODAM uses a sub-

laminate-based continuum damage mechanics formulation in which a strain to failure

strain ratio is used to predict the initiation of damage through different failure modes.

Damage accumulation and reduction of elastic moduli are tracked separately with

functions based on the different failure modes and coordinate directions. In MAT_221,

the orthotropic elastic response is the same as in MAT_22. However, it includes the

capabilities for simplified damage and composite failure models with functions based on

current strains, damage initiation strains and failure strains that are used to reduce the

elastic moduli in different coordinate directions through a damage mechanics approach

(Hallquist 2013). The damage and failure model developed by Pinho et al. (Pinho,

Iannucci and Robinson 2006) (Pinho, Iannucci and Robinson 2006), is implemented in

MAT_261, where different functions are used for each failure mode that are then

combined into a constitutive model through fracture mechanics concepts. Finally, a different approach to generating damage functions in different coordinate directions is employed in MAT_262 through an energy method rather than a strength technique (max. strain), but still within the context of a continuum damage mechanics formulation (Maimi, Camanho, et al. 2007) (Maimi, Camanho, et al. 2007).

Deformation Modeling: The deformations in a composite are computed using a constitutive relationship that relates the stress and strain components. In general, this response is nonlinear and can be accounted for by forming an elasto-plastic constitutive relationship. This nonlinear relationship can also be modeled using damage mechanics. Constitutive material models for composites have been developed for specific types of composites, such as fiber-reinforced composites (Cho, et al. 2010), unidirectional composites (Micallef, et al. 2013) and triaxial braided composites (Roberts, et al. 2009). The approach of using plasticity to account for the nonlinear response of a composite has been implemented by Sun and Chen (Sun and Chen 1989), in which a general quadratic plastic function was used to define the plasticity model for characterizing the nonlinear response of unidirectional carbon fiber based polymer matrix composites under plane stress conditions. Similarly, a plasticity-based constitutive model was developed by Vaziri et al. (Vaziri, Olson and Anderson 1991) for fiber-reinforced composites (FRC) that is able to predict the response of a single FRC layer for unidirectional and bidirectional fiber orientations, from elastic and plastic response to brittle and ductile failure. This model too is restricted to two-dimensional applications due to its plane stress assumption and does not account for a reduction in the unloading/reloading modulus (associated with the damage of the composite) during the plastic response.

Holzapfel and Gasser (Holzapfel and Gasser 2001) present a viscoelastic model for FRC materials but limit the applications to soft matrix materials. Lourenco et al. (Lourenco, Borst and Rots 1997) discuss an elasto-plastic model for orthotropic materials developed to describe the inelastic response associated with the softening behavior of the material under plane stress conditions. Other composite material models have been developed that are only applicable for certain limited conditions such as elastic-brittle behavior (Wang, et al. 2015) or ceramic matrix composites (Santhosh, et al. 2016).

Damage Modeling: Damage in composite material models is usually tracked as a function of the degree of failure, but in reality is a progression of micro-cracking, and is taken as maximum damage when the ultimate failure criteria are met. The continuum damage model developed by Matzenmiller et al (Matzenmiller, Lubliner and Taylor 1995), uses the initiation and accumulation of damage to model the nonlinear response of a composite by implementing damage parameters to reduce the effective stiffness of the material. There are other models that incorporate plasticity theory within the context of a damage model ((Barbero 2013), (Ladeveze and Le Dantec 1992), (Fouinneteau and Pickett 2007), (Song, et al. 2010)). In these models, the damage mechanics portion of the models are dominant and the plasticity theory is just added on to the basic damage model. It should be noted that perhaps it would be more efficient to incorporate features such as strain rate dependence in a consistent manner by utilizing plasticity theory as the basis of the model and adding in damage to account for nonlinear unloading and strain softening. With the current state-of-the-art in composite damage modeling, various finite element modeling approaches are needed to accurately model damage and failure phenomena. For example, in mesolevel modeling where individual layers are modeled separately but

individual fibers are not, different failure modes such as delamination, fiber failure and matrix failure can be modeled using the extended finite element method (XFEM) and cohesive zone elements (Van der Meer 2012). Similarly, complex composites such as triaxially-braided polymer composites require other approaches. For example, since damage propagates along fiber directions, one approach would be to build the braid architecture within the finite element model. In (Cheng 2006), the braided composite is modeled as a series of layered shell elements where each element is a laminated composite with the appropriate fiber-layup. A more complex model can be used to account for in-plane shifting of fibers in adjacent plies (Littell, et al. 2010).

Likewise, Xiao's composite material model (Xiao 2009) utilizes damage mechanics where the unloading response associated with damage affecting the energy absorption or dissipation in the model is used in extending the capabilities of MAT_58 to account for more complex damage conditions. Wu and Yao (Wu and Yao 2010) use a phenomological approach to track the progressive degradation of the structural properties based on a fatigue damage model developed by Chen and Hwang (Chen and Hwang 2009). Some experimental investigation has been done in regards to composite damage sources. For example, a punch shear test is used (Gama, et al. 2004) to define damage and delamination that may occur between each ply such as in plain weave composites, and the experimental results have been compared with simulations using LS-DYNA composite material model, MAT_162.

Failure Modeling: The failure of composites can be modeled at different scale levels. Pinho and co-workers (Pinho, Iannucci and Robinson 2006) use a micromechanical model to characterize failure - individual fiber pullout/failure, matrix

cracking and inter-ply delamination. At the macro-scale level, strain to failure strain ratios or stress to strength ratios in different coordinate directions have been used to determine the initiation and type of failure (Yen 2002). A multi-modal failure method has been implemented in the damage and failure model developed by Pinho et al (Pinho, Iannucci and Robinson 2006) (Pinho, Iannucci and Robinson 2006), in which separate models are used for different failure mechanisms including fiber tension failure, fiber kinking failure, matrix tensile failure and matrix compression failure. Failure has also been modeled for composite materials in terms of fracture initiated by imperfections assumed to be preexisting in bands between the fibers and matrix (Ozbolt, Lackovic and Krolo 2011). Additionally, others (Johnson, Pickett and Rozycki 2001) account for in-ply damage sources and delamination. Localized damage in composites, subjected to impact loads, has been modeled and analyzed using a meso-scale approach (Allix 2001), by determining a characteristic damage length and prescribing the size of the meso-constituent equivalent to that length. Recently, a new method has been developed to analyze deformation in structures containing discontinuities in the displacements, called the peridynamic model of solid mechanics, which has been implemented to analyze impact damage in composite laminates (Xu, et al. 2008).

Dissertation Objectives: While there is a need for a robust, efficient, accurate, general purpose constitutive material model that can be used across the large expanse of composite material classes , especially for the case of impact analysis, this is a challenging task given the wide array of performance conditions needed to capture the behavior accurately. While some models assume that the nonlinear response of a composite is due to either plasticity or damage, in reality the actual nonlinear material

9

behavior is due to a combination of both, and an improved model should include both contributions. This dissertation focuses on the development and implementation of a material model for predicting the deformation, damage and failure of fiber-reinforced composites. The developed model is implemented using a smeared (homogenized) approach using tabulated experimental data. The experimental data includes both laboratory experiments as well as virtual tests. For the deformation model, the commonly used Tsai-Wu composite failure criteria has been generalized and extended to a strain-hardening plasticity model with a quadratic yield function and a non-associative flow rule. For the damage model, a strain equivalent formulation has been developed, which allows the plasticity and damage calculations to be uncoupled, and the plasticity calculations to take place in the effective stress space. In traditional damage mechanics models such as the one developed by (Matzenmiller, Lubliner and Taylor 1995), a load in a particular coordinate direction is assumed to result in a stiffness reduction only in the direction of the applied load. However, as will be described in more detail later in this dissertation, a semi-coupled formulation is developed in which a load in one direction results in a stiffness reduction in all of the coordinate directions.

The primary objectives of the dissertation are presented below.

    i.   Model the elasto-plastic behavior of an orthotropic composite in three dimensions by using a Tsai-Wu based yield surface to determine if yielding has occurred. Carry out the plasticity calculations using a radial return algorithm with non-associative flow, represented by a modified Tsai-Wu quadratic function for the flow law.

ii. Account for the strain rate and temperature dependent material behavior in the constitutive model.

iii. Implement orthotropic damage that captures nonlinear unloading and local softening of the stress-strain response in the material model so that plastic and damage calculations can be uncoupled.

iv. Implement the constitutive model as MAT213 in LS-DYNA for solid elements.

v. Perform verification tests to ensure that the implementation is correct.

vi. Validate the developed constitutive model using coupon level test results as well as results from impact tests on unidirectional composite panels.

Chapter 2: Material Model Theory and Development

In this chapter the theoretical details of the constitutive model are presented. Details include those dealing with computation of the elasto-plastic deformation that is temperature and strain rate dependent, as well as the strain equivalent semi-coupled damage model.

2.1 Orthotropic 3D Elasto-Plastic Composite Material Model

The material deformation law in the model can be used to compute the elastic and permanent deformations of a composite with a full three-dimensional implementation suitable for solid and shell elements. Current development of the model includes a complete elasto-plastic deformation model, with strain rate and temperature effects, and damage, with failure capabilities to be added later. A quadratic function is used to define the yield surface. The Tsai-Wu failure criterion (Tsai and Wu 1971) has been generalized and is used as the orthotropic three-dimensional yield function for the plasticity model as

$$f(\sigma) = a + \begin{pmatrix} F_1 & F_2 & F_3 & 0 & 0 & 0 \end{pmatrix} \begin{bmatrix} \sigma_{11} \\ \sigma_{22} \\ \sigma_{33} \\ \sigma_{12} \\ \sigma_{23} \\ \sigma_{31} \end{bmatrix} + \begin{bmatrix} \sigma_{11} \\ \sigma_{22} \\ \sigma_{33} \\ \sigma_{12} \\ \sigma_{23} \\ \sigma_{31} \end{bmatrix}^T \begin{bmatrix} F_{11} & F_{12} & F_{13} & 0 & 0 & 0 \\ F_{12} & F_{22} & F_{23} & 0 & 0 & 0 \\ F_{13} & F_{23} & F_{33} & 0 & 0 & 0 \\ 0 & 0 & 0 & F_{44} & 0 & 0 \\ 0 & 0 & 0 & 0 & F_{55} & 0 \\ 0 & 0 & 0 & 0 & 0 & F_{66} \end{bmatrix} \begin{bmatrix} \sigma_{11} \\ \sigma_{22} \\ \sigma_{33} \\ \sigma_{12} \\ \sigma_{23} \\ \sigma_{31} \end{bmatrix} \quad (2.1)$$

where $a = -1$, the 1-2-3 subscripts refer to the principal material directions, and σ_{ii} represents the stresses and the F_{ii} terms are the yield function coefficients based on the current yield stress values in the various coordinate directions. The use of varying yield function coefficients allows for evolution of the yield surface and hardening can be precisely defined in each of the material directions. The normal coefficient values can be

12

determined by simplifying the yield function for the case of unidirectional tension and

compression as

$$F_i \sigma_{ii}^T + F_{ii} \left(\sigma_{ii}^T \right)^2 = 1$$
$$F_i \sigma_{ii}^C + F_{ii} \left(\sigma_{ii}^C \right)^2 = 1 \quad \text{for } i = 1, 2, 3 \qquad (2.2)$$

where F_i and F_{ii} are the linear and nonlinear coefficients, respectively. The two

expressions in Eqn. (2.2) can then be used to solve for the uniaxial yield coefficients, in

terms of the compressive and tensile yield stresses as

$$F_i = \frac{1}{\sigma_{ii}^T} - \frac{1}{\sigma_{ii}^C}$$

$$F_{ii} = \frac{1}{\sigma_{ii}^T \sigma_{ii}^C} \qquad (2.3)$$

The shear coefficient values can be determined in the same manner, by simplifying the

yield function for the case of shear loading in each coordinate direction as

$$F_{ii} \sigma_{ij}^2 = 1$$

$$F_{kk} = \frac{1}{\sigma_{ij}^2} \quad \text{for } i, j = 1, 2, 3, k = i + 3 \qquad (2.4)$$

where F_{ii} are the yield function coefficients and σ_{ij} are the shear stresses. The equations

can be written with the uniaxial coefficients as

$$F_1 = \frac{1}{\sigma_{11}^T} - \frac{1}{\sigma_{11}^C} \qquad F_{11} = \frac{1}{\sigma_{11}^T \sigma_{11}^C} \qquad F_{44} = \frac{1}{\sigma_{12}^2}$$

$$F_2 = \frac{1}{\sigma_{22}^T} - \frac{1}{\sigma_{22}^C} \qquad F_{22} = \frac{1}{\sigma_{22}^T \sigma_{22}^C} \qquad F_{55} = \frac{1}{\sigma_{23}^2} \qquad (2.5)$$

$$F_3 = \frac{1}{\sigma_{33}^T} - \frac{1}{\sigma_{33}^C} \qquad F_{33} = \frac{1}{\sigma_{33}^T \sigma_{33}^C} \qquad F_{66} = \frac{1}{\sigma_{31}^2}$$

The stress components of the yield function coefficients correspond to the current yield

stresses associated with the normal and shear tests (the methods of determining these

13

values are discussed below), where the superscript T indicates the tensile yield stress and the superscript C denotes the absolute value of the compressive yield stress. The off-axis coefficients, required to capture the interactive effects in the yield stresses, can be determined using the results of 45° off-axis tests in various coordinate directions. For example, consider a uniaxial 45° off-axis tensile test of a unidirectional composite, or any uniaxial tensile test performed at a 45° angle from the longitudinal (1-direction) material axis in the 1-2 plane, for a multi-ply laminated or textile composite. The stresses in the local material axes can be determined using the stress transformation equations (Daniel and Ishai 2006) and calculated using the following equations.

$$
\begin{aligned}
\sigma_{11} &= 0.5\sigma^{45} \\
\sigma_{22} &= 0.5\sigma^{45} \\
\sigma_{12} &= -0.5\sigma^{45}
\end{aligned}
\tag{2.6}
$$

The σ^{45} term in Eqn. (2.6) is the uniaxial yield stress in the structural loading direction obtained from the 45° off-axis tensile test. Substituting Eqn. (2.6) into Eqn. (2.1) and solving results in an expression for the off-axis yield function coefficient, F_{12} as

$$
F_{12} = \frac{2}{\left(\sigma_{12}^{45}\right)^2} - \frac{F_1 + F_2}{\sigma_{12}^{45}} - \frac{1}{2}\left(F_{11} + F_{22} + F_{44}\right)
\tag{2.7}
$$

Expressions for the other two off-axis yield coefficients, F_{13} and F_{23}, can be determined using similar procedures for 45° off-axis tests in the 1-3 and 2-3 planes, with the expressions for the yield coefficients defined as

$$
F_{23} = \frac{2}{\left(\sigma_{23}^{45}\right)^2} - \frac{F_2 + F_3}{\sigma_{23}^{45}} - \frac{1}{2}\left(F_{22} + F_{33} + F_{55}\right)
\tag{2.8}
$$

$$
F_{13} = \frac{2}{\left(\sigma_{13}^{45}\right)^2} - \frac{F_1 + F_3}{\sigma_{13}^{45}} - \frac{1}{2}\left(F_{11} + F_{33} + F_{66}\right)
\tag{2.9}
$$

14

A non-associative flow rule is used to define the evolution of the plastic strain

components, with the plastic potential for the flow rule calculated as

$$h = \sqrt{H_{11}\sigma_{11}^2 + H_{22}\sigma_{22}^2 + H_{33}\sigma_{33}^2 + 2H_{12}\sigma_{11}\sigma_{22} + 2H_{23}\sigma_{22}\sigma_{33} + 2H_{31}\sigma_{33}\sigma_{11} + H_{44}\sigma_{12}^2 + H_{55}\sigma_{23}^2 + H_{66}\sigma_{31}^2} \qquad (2.10)$$

where the H_{ij} terms are the independent flow rule coefficients assumed to be constant,

and σ_{ij} are the current stress values. The procedure for determining the flow rule

coefficient values is discussed later. In order to ensure convexity of the flow surface, the

flow rule coefficients must satisfy specific conditions (Yang and Feng 1984). A general

quadratic failure/yield function, similar to the Tsai-Wu criterion used for the yield surface

in this model, can be written as

$$f(\boldsymbol{\sigma}) = a + \mathbf{b}^T \boldsymbol{\sigma} + \boldsymbol{\sigma}^T \mathbf{P} \boldsymbol{\sigma} \qquad (2.11)$$

where $\boldsymbol{\sigma}^T = \left(\sigma_{11}, \sigma_{22}, \sigma_{33}, \sigma_{12}, \sigma_{23}, \sigma_{31}\right)$, a is a scalar, $\mathbf{b}$ is a vector and $\mathbf{P}$ is a matrix. In

general, $\mathbf{b}$ is comprised of six independent coefficients, whereas $\mathbf{P}$ contains 36

coefficients, 21 of which are independent due to symmetry. The flow rule can be written

in the form of the quadratic function as

$$h^2 = H_{11}\sigma_{11}^2 + H_{22}\sigma_{22}^2 + H_{33}\sigma_{33}^2 + 2H_{12}\sigma_{11}\sigma_{22} + 2H_{23}\sigma_{22}\sigma_{33} + 2H_{31}\sigma_{33}\sigma_{11} + H_{44}\sigma_{12}^2 + H_{55}\sigma_{23}^2 + H_{66}\sigma_{31}^2$$

$$h^2 = \begin{bmatrix} \sigma_{11} \\ \sigma_{22} \\ \sigma_{33} \\ \sigma_{12} \\ \sigma_{23} \\ \sigma_{31} \end{bmatrix}^T \begin{bmatrix} H_{11} & H_{12} & H_{13} & 0 & 0 & 0 \\ H_{12} & H_{22} & F_{23} & 0 & 0 & 0 \\ H_{13} & H_{23} & H_{33} & 0 & 0 & 0 \\ 0 & 0 & 0 & H_{44} & 0 & 0 \\ 0 & 0 & 0 & 0 & H_{55} & 0 \\ 0 & 0 & 0 & 0 & 0 & H_{66} \end{bmatrix} \begin{bmatrix} \sigma_{11} \\ \sigma_{22} \\ \sigma_{33} \\ \sigma_{12} \\ \sigma_{23} \\ \sigma_{31} \end{bmatrix} = \boldsymbol{\sigma}^T \mathbf{H} \boldsymbol{\sigma} \qquad (2.12)$$

with $\mathbf{H}$ being the matrix of flow law coefficients and representing $\mathbf{P}$ from the general

form of the quadratic yield function. To ensure convexity of the quadratic function, the

coefficients $\mathbf{b}$ and $\mathbf{P}$ must have constraints. Assuming two distinct stress states $\boldsymbol{\sigma}$ and

$\boldsymbol{\sigma}'$, the convex combination of the two vectors is

15

$$\bar{\sigma} = \alpha\sigma + (1-\alpha)\sigma' \quad 0 \leq \alpha \leq 1 \tag{2.13}$$

and to ensure convexity of f, must satisfy the inequality

$$f(\bar{\sigma}) \leq \alpha f(\sigma) + (1-\alpha) f(\sigma') \tag{2.14}$$

where the yield function value determined at the convex combination of the two stress states, must be within the convex combination of the yield function values evaluated at each stress state (remain within the convex hull). Thus, substituting Eqn. (2.13) into Eqn. (2.11), the inequality, Eqn. (2.14) is reduced to the following equations

$$a + \mathbf{b}^T\bar{\sigma} + \bar{\sigma}^T\mathbf{P}\bar{\sigma} \leq \alpha\left[a + \mathbf{b}^T\sigma + \sigma^T\mathbf{P}\sigma\right] + (1-\alpha)\left[a + \mathbf{b}^T\sigma' + \sigma'^T\mathbf{P}\sigma'\right]$$

or

$$\begin{aligned}
&a + \mathbf{b}^T\left[\alpha\sigma + (1-\alpha)\sigma'\right] \\
&+ \left[\alpha\sigma + (1-\alpha)\sigma'\right]^T \mathbf{P}\left[\alpha\sigma + (1-\alpha)\sigma'\right]
\end{aligned} \leq \begin{aligned}
&\alpha\left[a + \mathbf{b}^T\sigma + \sigma^T\mathbf{P}\sigma\right] \\
&+ (1-\alpha)\left[a + \mathbf{b}^T\sigma' + \sigma'^T\mathbf{P}\sigma'\right]
\end{aligned}$$

or

$$\begin{aligned}
&a + \alpha\mathbf{b}^T\sigma + \mathbf{b}^T\sigma' - \alpha\mathbf{b}^T\sigma' \\
&+ \left[\alpha\sigma^T + \sigma'^T - \alpha\sigma'^T\right]\left[\alpha\mathbf{P}\sigma + \mathbf{P}\sigma' - \alpha\mathbf{P}\sigma'\right]
\end{aligned} \leq \begin{aligned}
&\alpha a + \alpha\mathbf{b}^T\sigma + \alpha\sigma^T\mathbf{P}\sigma \\
&+ a + \mathbf{b}^T\sigma' + \sigma'^T\mathbf{P}\sigma' - \alpha a - \alpha\mathbf{b}^T\sigma' - \alpha\sigma'^T\mathbf{P}\sigma'
\end{aligned}$$

or

$$\alpha\sigma^T\mathbf{P}\sigma' - \alpha^2\sigma^T\mathbf{P}\sigma' + \alpha\sigma'^T\mathbf{P}\sigma - \alpha\sigma'^T\mathbf{P}\sigma' - \alpha^2\sigma'^T\mathbf{P}\sigma - \alpha^2\sigma'^T\mathbf{P}\sigma' \leq 0$$

$$-\alpha\left[-\sigma^T\mathbf{P}\sigma' + \alpha\sigma^T\mathbf{P}\sigma' - \sigma'^T\mathbf{P}\sigma + \sigma'^T\mathbf{P}\sigma' + \alpha\sigma'^T\mathbf{P}\sigma + \alpha\sigma'^T\mathbf{P}\sigma'\right] \leq 0$$

$$-\sigma^T\mathbf{P}\sigma' + \alpha\sigma^T\mathbf{P}\sigma' - \sigma'^T\mathbf{P}\sigma + \sigma'^T\mathbf{P}\sigma' + \alpha\sigma'^T\mathbf{P}\sigma + \alpha\sigma'^T\mathbf{P}\sigma' \geq 0$$

$$(1-\alpha)(\sigma - \sigma')^T\mathbf{P}(\sigma - \sigma') \geq 0$$

or

$$(\sigma - \sigma')^T\mathbf{P}(\sigma - \sigma') \geq 0 \tag{2.15}$$

for all $\boldsymbol{\sigma}$ and $\boldsymbol{\sigma}'$. This implies that $\mathbf{P}$ must be positive semidefinite implying that the diagonal components of $\mathbf{P}$ must be nonnegative

$$\mathbf{P}_{ii} \geq 0 \quad i = 1, 2, ..., 6 \tag{2.16}$$

and the off-diagonal components of $\mathbf{P}$ must satisfy the following condition.

$$\mathbf{P}_{ii}\mathbf{P}_{jj} - \mathbf{P}_{ij}^2 \geq 0 \quad i = 1, 2, ..., 6, \quad j = i+1, ..., 6 \tag{2.17}$$

The two constraints in Eqns. (2.16) and (2.17) can then be written in terms of the flow law coefficients as

$$\begin{aligned}
H_{11} &\geq 0 \\
H_{22} &\geq 0 \\
H_{33} &\geq 0 \\
H_{44} &\geq 0 \\
H_{55} &\geq 0 \\
H_{66} &\geq 0 \\
H_{11}H_{22} - H_{12}^2 &\geq 0 \\
H_{33}H_{22} - H_{23}^2 &\geq 0 \\
H_{11}H_{33} - H_{31}^2 &\geq 0
\end{aligned} \tag{2.18}$$

with the coefficients determined using a procedure described later.

The plastic potential function in Eqn. (2.10) is used in the flow law with the usual normality hypothesis of classical plasticity assumed to apply, where the plasticity variable, λ, is a scalar plastic multiplier (Khan and Huang 1995). Thus, the plastic strains are defined in terms of the plastic multiplier, flow potential and stresses as

$$\dot{\boldsymbol{\varepsilon}}^p = \dot{\lambda}\frac{\partial h}{\partial \boldsymbol{\sigma}}$$

$$\dot{\varepsilon}_{11}^p = \frac{\dot{\lambda}}{2h}\left(2H_{11}\sigma_{11} + 2H_{12}\sigma_{22} + 2H_{13}\sigma_{33}\right)$$

$$\dot{\varepsilon}_{22}^p = \frac{\dot{\lambda}}{2h}\left(2H_{12}\sigma_{11} + 2H_{22}\sigma_{22} + 2H_{23}\sigma_{33}\right)$$

$$\dot{\varepsilon}_{33}^p = \frac{\dot{\lambda}}{2h}\left(2H_{13}\sigma_{11} + 2H_{23}\sigma_{22} + 2H_{33}\sigma_{33}\right) \tag{2.19}$$

$$\dot{\varepsilon}_{12}^p = \frac{\dot{\lambda}}{2h}H_{44}\sigma_{12}$$

$$\dot{\varepsilon}_{23}^p = \frac{\dot{\lambda}}{2h}H_{55}\sigma_{23}$$

$$\dot{\varepsilon}_{31}^p = \frac{\dot{\lambda}}{2h}H_{66}\sigma_{31}$$

where ε_{jj}^p are the individual plastic strain components, with the shear components

representing tensorial, not engineering, strain. Using the expressions for the plastic

strains, in Eqn. (2.19), and defining the "plastic Poisson's ratios" in terms of these plastic

strains, the coefficients of the flow potential function, H_{ij}, can be defined as (uniaxial

testing in the 1 direction)

$$\sigma_{11} \neq 0$$

$$\nu_{12}^p = -\frac{\dot{\varepsilon}_{22}^p}{\dot{\varepsilon}_{11}^p} = -\frac{H_{12}}{H_{11}} \tag{2.20}$$

$$\nu_{13}^p = -\frac{\dot{\varepsilon}_{33}^p}{\dot{\varepsilon}_{11}^p} = -\frac{H_{13}}{H_{11}}$$

From uniaxial testing in the 2 direction, we have

$$\sigma_{22} \neq 0$$

$$\nu_{21}^p = -\frac{\dot{\varepsilon}_{11}^p}{\dot{\varepsilon}_{22}^p} = -\frac{H_{12}}{H_{22}} \tag{2.21}$$

$$\nu_{23}^p = -\frac{\dot{\varepsilon}_{33}^p}{\dot{\varepsilon}_{22}^p} = -\frac{H_{23}}{H_{22}}$$

From uniaxial testing in the 3 direction, we have

$$\sigma_{33} \neq 0$$

$$v^p_{32} = -\frac{\dot{\varepsilon}^p_{22}}{\dot{\varepsilon}^p_{33}} = -\frac{H_{23}}{H_{33}} \tag{2.22}$$

$$v^p_{31} = -\frac{\dot{\varepsilon}^p_{11}}{\dot{\varepsilon}^p_{33}} = -\frac{H_{13}}{H_{33}}$$

which are useful in creating a procedure for characterizing the coefficient values. A

general shape of the yield and flow surfaces, for a plane stress case, are shown in Fig. 2

and Fig. 3, respectively (values are set for example only). Note that

$$F_1 = -0.75, \quad F_2 = 3.0, \quad F_{11} = 0.5, \quad F_{22} = 2.0, \quad F_{12} = -0.5, \quad F_{44} = 5$$

and

$$H_{11} = H_{22} = 1.0, \quad H_{12} = -0.101, \quad H_{44} = 3.0 \ .$$

(a)   (b)
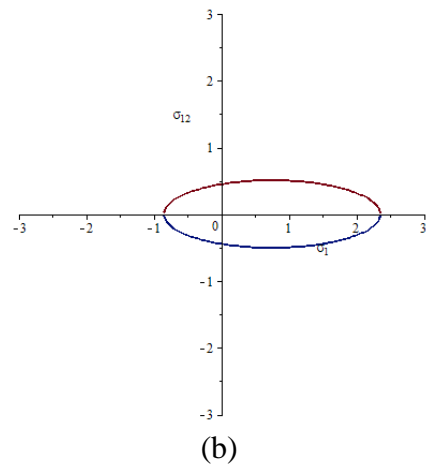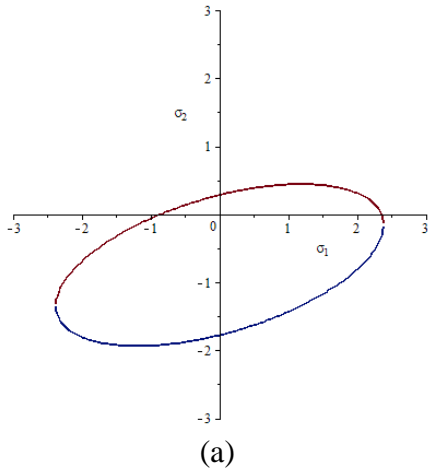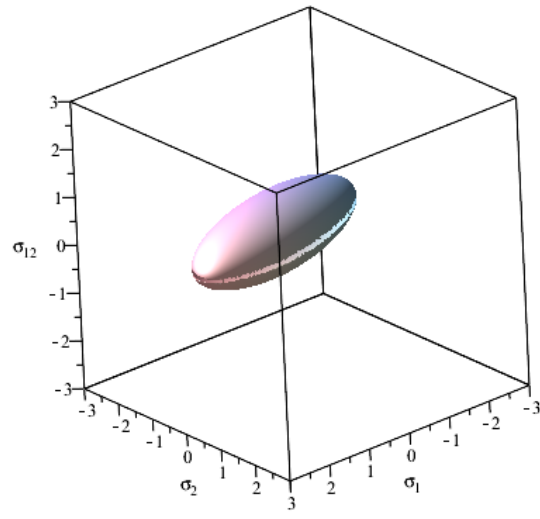
(c)

Fig. 2. Example Yield Surface for Plane Stress Case (a) 2D: $\sigma_1 - \sigma_2$ Plane (b) 2D:
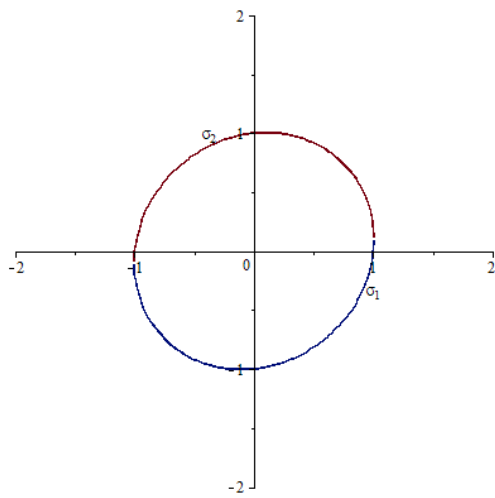
$\sigma_1 - \sigma_{12}$ Plane (c) 3D Plot

(a)
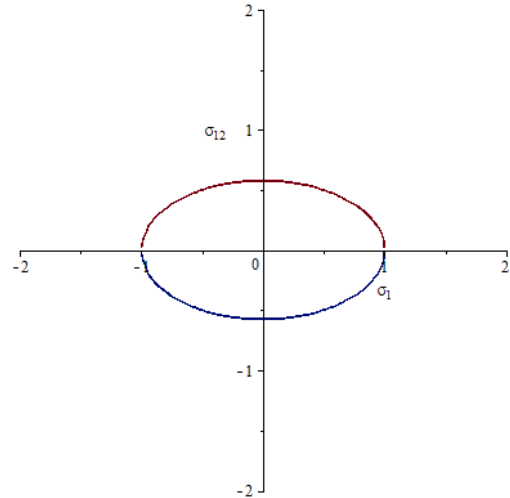
(b)
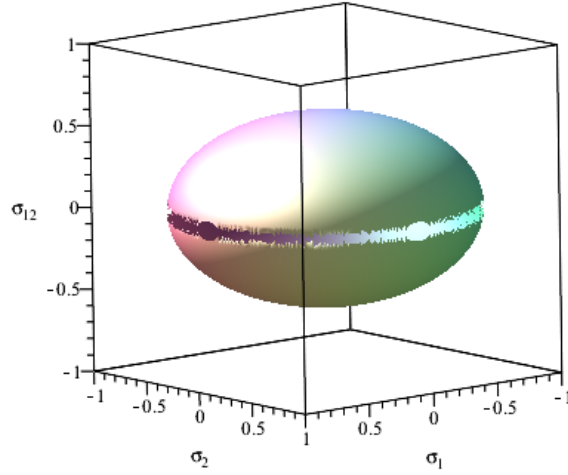
(c)

Fig. 3. Example Flow Surface for Plane Stress Case (a) 2D: $\sigma_1 - \sigma_2$ Plane (b) 2D: $\sigma_1 - \sigma_{12}$

Plane (c) 3D Plot

At this point, it is important to note that the flow law contains only the quadratic terms, whereas the yield function also includes the linear terms and hence is able to differentiate between tension and compression that the flow law cannot. Including the linear terms in flow law would make plastic Poisson's ratio dependent on stress, and in turn the flow law coefficients. For example, the uniaxial plastic strains would be defined as

$$\dot{\varepsilon}_{11}^p = \frac{\dot{\lambda}}{2h}\left(H_1 + 2H_{11}\sigma_{11} + 2H_{12}\sigma_{22} + 2H_{13}\sigma_{33}\right)$$

$$\dot{\varepsilon}_{22}^p = \frac{\dot{\lambda}}{2h}\left(H_2 + 2H_{12}\sigma_{11} + 2H_{22}\sigma_{22} + 2H_{23}\sigma_{33}\right) \qquad (2.23)$$

$$\dot{\varepsilon}_{33}^p = \frac{\dot{\lambda}}{2h}\left(H_3 + 2H_{13}\sigma_{11} + 2H_{23}\sigma_{22} + 2H_{33}\sigma_{33}\right)$$

where H_i would be the linear flow law coefficients. Thus, considering a uniaxial test in the 1-direction, the plastic Poisson's ratios would be defined as

21

$$\sigma_{11} \neq 0$$

$$\nu_{12}^p = -\frac{\dot{\varepsilon}_{22}^p}{\dot{\varepsilon}_{11}^p} = -\frac{H_{12} + H_2}{H_{11} + H_1}$$

$$\nu_{13}^p = -\frac{\dot{\varepsilon}_{33}^p}{\dot{\varepsilon}_{11}^p} = -\frac{H_{13} + H_3}{H_{11} + H_1}$$

(2.24)

This stress dependency, needed to solve for the additional parameters, on the flow law coefficients would most likely result in erratic behavior of the model. The flow law coefficients could be assumed to vary based on the current stress and strain state, similar to the yield function coefficients, but would require the development of conditions to define the evolution of the flow law, which may be difficult to construct using experimental data. This might include normalizing the flow rule coefficients with respect to a common variable, similar to the effective plastic strain used for the yield surface. In doing so, the plastic Poisson's ratios used to calculate the flow rule coefficients is Eqn. (2.24), would need to be defined as a function of the effective plastic strain, and the flow rule coefficients would be calculated based on the varying values of the plastic Poisson's ratios (the following theory and implementation assumes constant plastic Poisson's ratios and therefore constant flow rule coefficients).

Expressions for the effective stress and effective plastic strain can now be written using the flow law and the principle of the equivalence of plastic work (Khan and Huang 1995). Taking a vector product of the stress and plastic strain tensors, results in the plastic potential function h being multiplied by the plastic multiplier λ. The principle of the equivalence of plastic work defines the vector product of the stress and the plastic strain to be equal to the product of the effective stress and effective plastic strain. Therefore, the effective stress can be defined by the plastic potential function h and the

effective plastic strain can be defined by the plastic multiplier λ. This process can be shown as

$$\dot{W}_p = \boldsymbol{\sigma} : \dot{\boldsymbol{\varepsilon}}^p = \boldsymbol{\sigma} : \lambda \frac{\partial h}{\partial \boldsymbol{\sigma}} = h\dot{\lambda} = \sigma_e : \dot{\varepsilon}_e^p, \qquad (2.25)$$

where $\dot{W}_p$ is the plastic work, σ_e is the effective stress and ε_e^p is the effective plastic strain.

It is common, in plasticity constitutive equations, to use analytical functions to define the evolution of stresses as a function of the (effective) plastic strain components in order to compute the current value of the yield stresses required to evaluate the yield function. Alternatively, tabulated stress-strain curves can be used to track the changes of the yield stresses in each coordinate direction. In this dissertation, experimental stress versus plastic strain curves generated for each yield stress value (uniaxial tension and compression curves in each of the normal directions (1-2-3), shear curves in each of the shear directions, 1-2, 2-3, 3-1, and 45° off-axis tension curves in the 1-2, 2-3 and 3-1 planes) are used as tabulated stress-strain curves. The off-axis tests are required to calculate the interaction terms $\left(F_{12}, F_{13}, F_{23} \right)$ defined in Eqns. (2.7), (2.8) and (2.9). This approach eliminates the use of curve fitting approximations since tabulated stress-strain curves are used to track the evolution of the deformation response.

The tabulated stress-strain data can be generated from actual laboratory testing or supplemented using appropriate numerical experiments simulated in stand-alone codes (virtual testing). Though there are twelve required stress-strain curves for the model, the actual number of tests may be smaller based on the composite architecture. A unidirectional composite has transverse isotropy and hence requires only four tension and

23

compression tests (1 and 2/3 directions), only two shear tests (1-2/3, 2-3) and only two

45° off-axis tests (1-2/3, 2-3). However, the 45° off-axis test in the 2-3 plane is not

necessary, as the response is approximately equal to that of the uniaxial tension test in the

2/3 direction (as deduced from transverse isotropy). Thus, the number of required tests

for a uniaxial composite can be reduced from twelve to seven, and a similar

simplification approach can be used for other composites with some degree of symmetric

architecture. A summary of reducing experimental tests for few special cases is shown in

Table 2.

Table 2. Reduction of Experimental Testing Based on Composite Architecture

Label	Experimental Test	Material Type			
		Isotropic	Plane Stress (2-D, thin shell))	Transversely Isotropic in 2-3 (Unidirectional Fiber Composite)	Transversely Isotropic in 1-2 (Plain Weave Composite)
T1	Tension (1-direction)	Needed	Needed	Needed	Needed
T2	Tension (2-direction)	Same as T1	Needed	Needed	Same as T1
T3	Tension (3-direction)	Same as T1	Not Needed	Same as T2	Needed
C1	Compression (1-direction)	Needed	Needed	Needed	Needed
C2	Compression (2-direction)	Same as C1	Needed	Needed	Same as C1
C3	Compression (3-direction)	Same as C2	Not Needed	Same as C2	Needed
S12	Shear (1-2 direction)	Not Needed	Needed	Needed	Needed
S23	Shear (2-3 direction)	Not Needed	Not Needed	Needed	Needed
S13	Shear (1-3 direction)	Not Needed	Not Needed	Same as S12	Same as S23
O12	Off-axis Tension (45°, 1-2 plane)	Not Needed	Needed	Needed	Needed

		Not Needed	Not Needed	Same as T2	Needed
O23	Off-axis Tension/Compression (45°, 2-3 plane)	Not Needed	Not Needed	Same as T2	Needed
O13	Off-axis Tension/Compression (45°, 1-3 plane)	Not Needed	Not Needed	Same as O12	Same as O23
	Total Number of Tests to Perform	2	6	7	8

The effective plastic strain is used as the tracking parameter for the evolution of the deformation response by determining the yield stresses from each of the tabulated input curves as a function of the effective plastic strain at each time step. Therefore, the tabulated stress-strain curves must be normalized and converted to stress versus effective plastic strain. This is achieved by using the principle of the equivalence of plastic work to relate the plastic strain increment to the effective plastic strain increment. The effective plastic strain can then be written in terms of the plastic strain and flow potential function as (for a unidirectional loading in the 1-direction)

$$
\begin{aligned}
\sigma_{ij}d\varepsilon_{ij}^p &= \sigma_e d\varepsilon_e^p = h d\varepsilon_e^p \\
\sigma_{11}d\varepsilon_{11}^p &= h d\varepsilon_e^p \\
\sigma_{11}d\varepsilon_{11}^p &= \sqrt{H_{11}}\sigma_{11}d\varepsilon_e^p \\
d\varepsilon_e^p &= \frac{\sigma_{11}d\varepsilon_{11}^p}{\sqrt{H_{11}}\sigma_{11}} \\
\varepsilon_e^p &= \int \frac{\sigma_{11}d\varepsilon_{11}^p}{\sqrt{H_{11}}\sigma_{11}}
\end{aligned}
\tag{2.26}
$$

where σ_{11} is the unidirectional stress, $d\varepsilon_{11}^p$ is the plastic strain increment in the loading direction and $d\varepsilon_e^p$ is the effective plastic strain increment. The expression for the effective plastic strain in Eqn. (2.26) can be rewritten as $\varepsilon_e^p = \int \frac{\sigma_{11}d\varepsilon_{11}^p}{h}$, in which it is

clear that the effective plastic strain can be computed as the incremental area of the stress versus plastic strain curve divided by the current effective stress value. An example of this transformation is shown in Fig. 4.

$$\varepsilon_{11}^{p} = \varepsilon_{11} - \frac{\sigma_{11}}{E_{11}}$$

$$\varepsilon_{e}^{p} = \int \frac{\sigma_{11} d\varepsilon_{11}}{h}$$

User provided load curves are true stress versus true plastic strain

Internally stored is true stress versus effective plastic strain
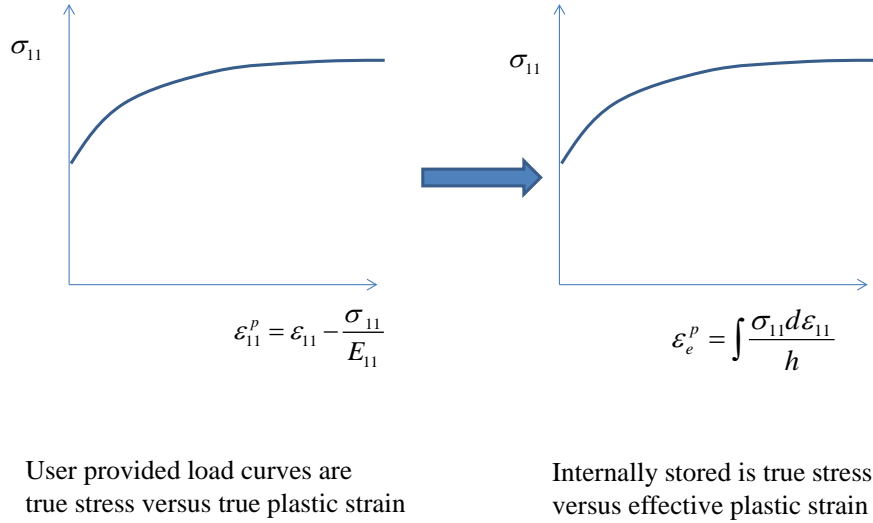
Fig. 4. Conversion of Stress Versus Plastic Strain Curves to Stress Versus Effective Plastic Strain Curves

The computation of the effective plastic strain is achieved using a numerical algorithm based on the radial return method. From the updated value of the effective plastic strain, the yield stress values and the overall stress state can be determined (details of the numerical implementation are explained later in this dissertation). The revised stresses are computed using a typical elastic constitutive equation in which the flow law is used to describe the plastic strains as

$$\dot{\boldsymbol{\sigma}} = \mathbf{C} : \left(\dot{\boldsymbol{\varepsilon}} - \dot{\boldsymbol{\varepsilon}}^{\mathbf{p}} \right) = \mathbf{C} : \left(\dot{\boldsymbol{\varepsilon}} - \dot{\lambda} \frac{\partial h}{\partial \boldsymbol{\sigma}} \right) \tag{2.27}$$

where $\mathbf{C}$ is the standard elastic stiffness matrix, $\boldsymbol{\sigma}$ is the total strain. The effective plastic strain rate, $\dot{\lambda}$ is calculated using a combination of the consistency condition (the

stress state must remain on the subsequent yield surface, during the plastic deformation) and elastic constitutive equation as

$$
\dot{f} = \frac{\partial f}{\partial \boldsymbol{\sigma}} \dot{\boldsymbol{\sigma}} + \frac{\partial f}{\partial \mathbf{q}} \dot{\mathbf{q}} = 0
$$

$$
\dot{f} = \frac{\partial f}{\partial \boldsymbol{\sigma}} \left(\mathbf{C} : \dot{\boldsymbol{\varepsilon}} - \mathbf{C} : \dot{\lambda} \frac{\partial h}{\partial \boldsymbol{\sigma}} \right) + \frac{\partial f}{\partial \mathbf{q}} \dot{\lambda} \frac{d\mathbf{q}}{d\lambda} = 0 \qquad (2.28)
$$

$$
\dot{\lambda} = \frac{\dfrac{\partial f}{\partial \boldsymbol{\sigma}} \mathbf{C} : \dot{\boldsymbol{\varepsilon}}}{\dfrac{\partial f}{\partial \boldsymbol{\sigma}} \mathbf{C} : \dfrac{\partial h}{\partial \boldsymbol{\sigma}} + \dfrac{\partial f}{\partial \mathbf{q}} \dfrac{d\mathbf{q}}{d\lambda}}
$$

where f is the yield function defined in Eqn. (2.1) and $\mathbf{q}$ is the vector of yield stresses, determined from the input stress-strain data written as

$$
\mathbf{q}^T = \begin{bmatrix} \sigma_{11}^T & \sigma_{22}^T & \sigma_{33}^T & \sigma_{11}^C & \sigma_{22}^C & \sigma_{33}^C & \sigma_{12} & \sigma_{23} & \sigma_{31} & \sigma_{45-12}^C & \sigma_{45-23}^C & \sigma_{45-31}^C \end{bmatrix} \quad (2.29)
$$

The derivative of the $\mathbf{q}$ vector with respect to the effective plastic strain, λ, can be determined using a chain rule expansion based on the plastic strain as

$$
\frac{d\mathbf{q}}{d\lambda} = \frac{d\mathbf{q}}{d\boldsymbol{\varepsilon}^p} \frac{d\boldsymbol{\varepsilon}^p}{d\lambda} \qquad (2.30)
$$

where the derivative of the yield stress vector with respect to the plastic strain is the instantaneous slope of the stress versus plastic strain curve and the derivative of the plastic strain with respect to the effective plastic strain is determined from the flow law, both corresponding to each of the twelve input stress-strain curves. However, special consideration must be taken in the off-axis case for which the flow law must first be converted to the material axis coordinate system and then the plastic strains must be converted to the structural axis system. To do so, the off-axis test is first converted to stress vs. plastic strain in the structural axis system, then converted to stress vs. effective

plastic strain, as demonstrated in Fig. 4. However, the flow law h is defined in terms of the material axis system of the off-axis test (1-2 case, for example) as

$$\left(h \right)_{45-12} = \sqrt{H_{11}\sigma_{11}^2 + H_{22}\sigma_{22}^2 + 2H_{12}\sigma_{11}\sigma_{22} + H_{44}\sigma_{12}^2}$$

but the material axis stresses can be written in terms of the structural axis stress,

$$\sigma_{11} = 0.5\sigma$$
$$\sigma_{22} = 0.5\sigma$$
$$\sigma_{12} = -0.5\sigma$$

resulting in a simplified function of the off-axis case for the flow law as defined in Eqn. (2.31).

$$\left(h \right)_{45-12} = 0.5\sigma_{45-12}\sqrt{H_{11} + H_{22} + 2H_{12} + H_{44}} \tag{2.31}$$

This is done, in order to compute the correct derivative of the plastic strain with respect to the effective plastic strain, as the input for the off-axis tests is assumed to be in the structural coordinate system. Furthermore, the secant method is used with the radial return method to compute the necessary value of the effective plastic strain increment.

2.2 Characterization of Flow Law Coefficients

The flow law coefficients, introduced in the previous section, need to be characterized based on the data obtained from experimental stress-strain curves or virtual testing, with the procedures detailed in this section defined for quasi-static, room temperature tests. For example, if the mechanical properties of composite constituents are known, stress-strain curves can be generated through virtual tests conducted using either high fidelity finite element analysis, e.g. Virtual Testing System Software (VTSS)

(Harrington and Rajan 2014) developed at ASU, or analytical tools such as the

micromechanics code MAC-GMC (Bednarcyk and Arnold 2002) developed at NASA

Glenn.

The procedure for the determination of the flow law coefficients for a general

composite is presented here beginning with a unidirectional composite. In the case of a

unidirectional carbon fiber composite, it is reasonable to assume that the plastic strain in

the fiber direction (1 direction) is equal to zero for all values of stress due to the linear

elastic behavior of the carbon fiber (Sun and Chen 1989). From the second expression in

Eqn. (2.19), it is clear that the plastic strain can only be zero if the flow law coefficients

H_{11}, H_{12}, and H_{13} are all equal to zero. In the same regard, the response in the transverse

(2-direction) composite direction can show some degree of nonlinearity, and for a

unidirectional load in the 2 direction, it is reasonable to assume the value of the effective

stress, h, to be equal to the applied stress, σ_{22}. Then, the plastic potential function, Eqn.

(2.10) , can be simplified for the case of a uniaxial applied load in the 2-direction as

$$h = \sqrt{H_{22}\sigma_{22}^2} = \sqrt{H_{22}}\sigma_{22} \tag{2.32}$$

and from the assumption that the effective stress, h, is equal to the applied stress, σ_{22},

the flow law coefficient, H_{22}, must be equal to one. Due to the transverse isotropy in the

unidirectional composite, the flow law coefficient, H_{33}, can be assumed to be one as

well, and using these known values of the flow law coefficients, the remaining value,

H_{23}, can be determined using Eqn. (2.21) as

$$H_{23} = -H_{22}v_{23}^p = -v_{23}^p \tag{2.33}$$

The flow law coefficients are assumed to be constant, which requires a constant value of the plastic Poisson's ratio, and can be determined as an average value from unidirectional transverse tension test data. The flow law coefficient for in-plane shear, H_{44}, can be calculated using a similar procedure (Sun and Chen 1989), in which the plastic potential function in Eqn. (2.10), and plastic strain definition, in Eqn. (2.19), are simplified for a pure shear loading case in the 1-2 plane as

$$h = \sigma_e = \sigma_{12}\sqrt{H_{44}}$$

$$d\varepsilon_{12}^p = \frac{d\lambda}{2h}H_{44}\sigma_{12} = \frac{d\varepsilon_e^p}{2\sigma_{12}\sqrt{H_{44}}}H_{44}\sigma_{12}$$

$$= 0.5d\varepsilon_e^p\sqrt{H_{44}}$$

$$or, d\varepsilon_e^p = \frac{d\varepsilon_{12}^p}{0.5\sqrt{H_{44}}}$$

(2.34)

Therefore, the shear coefficient, H_{44}, can be determined by fitting the effective stress versus effective plastic strain curve, for the in-plane shear, to the overall effective stress versus effective plastic strain curve, based on the transverse tension test for a unidirectional carbon fiber composite using Eqn. (2.34). The coefficient, H_{55}, can be determined using a similar fitting approach using shear loading in the 2-3 plane, or using transverse isotropy of the composite, the effective stress for an off-axis test in the 2-3 plane can be calculated and used to determine the coefficient, H_{55}, from H_{23}, as

$$H_{55} = 2\left(1+v_{23}^p\right) = 2\left(1-H_{23}\right)$$

(2.35)

Finally, the last flow law coefficient, H_{66}, can be set equal to H_{44}, using transverse isotropy.

In the general case, such as a triaxially braided composite, similar procedures can be used to determine the flow law coefficients taking the tension test in the 1-direction as the baseline case. The flow law coefficient, H_{11}, can be determined by simplifying Eqn. (2.10) for unidirectional applied stress in the 1-direction as

$$h = \sqrt{H_{11}\sigma_{11}^2} = \sqrt{H_{11}}\sigma_{11} \tag{2.36}$$

From Eqn. (2.36), it is clear that the coefficient, H_{11}, is equal to one. Thus, the relationships of the other flow law coefficients, from Eqns. (2.20), (2.21) and (2.22), can be rewritten in terms of the known coefficient, H_{11}. First, modifying Eqns. (2.20), (2.21) and (2.22) by assuming a value for H_{11} and eliminating H_{11} yields

$$\begin{bmatrix} 0 & 0 & 0 & 1 & 0 \\ \nu_{21}^p & 0 & 1 & 0 & 0 \\ \nu_{23}^p & 0 & 0 & 0 & 1 \\ 0 & \nu_{32}^p & 0 & 0 & 1 \\ 0 & \nu_{31}^p & 0 & 1 & 0 \end{bmatrix} \begin{Bmatrix} H_{22} \\ H_{33} \\ H_{12} \\ H_{13} \\ H_{23} \end{Bmatrix} = \begin{Bmatrix} -\nu_{13}^p H_{11} \\ 0 \\ 0 \\ 0 \\ 0 \end{Bmatrix}. \tag{2.37}$$

These equations are linearly independent and one can solve for the five unknown coefficients. Pivoting the rows results in

$$\begin{bmatrix} \nu_{23}^p & 0 & 0 & 0 & 1 \\ 0 & \nu_{31}^p & 0 & 1 & 0 \\ \nu_{21}^p & 0 & 1 & 0 & 0 \\ 0 & 0 & 0 & 1 & 0 \\ 0 & \nu_{32}^p & 0 & 0 & 1 \end{bmatrix} \begin{Bmatrix} H_{22} \\ H_{33} \\ H_{12} \\ H_{13} \\ H_{23} \end{Bmatrix} = \begin{Bmatrix} 0 \\ 0 \\ 0 \\ -\nu_{13}^p H_{11} \\ 0 \end{Bmatrix}. \tag{2.38}$$

Now that the diagonals are all non-zero, a Gauss-Jordan elimination can be performed to obtain an analytical expression for the five remaining flow rule coefficients, which yields

$$
\begin{bmatrix} 1 & 0 & 0 & 0 & 0 \\ 0 & 1 & 0 & 0 & 0 \\ 0 & 0 & 1 & 0 & 0 \\ 0 & 0 & 0 & 1 & 0 \\ 0 & 0 & 0 & 0 & 1 \end{bmatrix} \begin{Bmatrix} H_{22} \\ H_{33} \\ H_{12} \\ H_{13} \\ H_{23} \end{Bmatrix} = \begin{Bmatrix} \dfrac{v^p_{32}v^p_{13}}{v^p_{23}v^p_{31}} H_{11} \\[2ex] \dfrac{v^p_{13}}{v^p_{31}} H_{11} \\[2ex] -\dfrac{v^p_{21}v^p_{32}v^p_{13}}{v^p_{23}v^p_{31}} H_{11} \\[2ex] -v^p_{13}H_{11} \\[2ex] \dfrac{v^p_{32}v^p_{13}}{v^p_{31}} H_{11} \end{Bmatrix}.
\tag{2.39}
$$

Therefore, the coefficients can be rewritten in terms of the plastic Poisson's ratios and

H_{11} (equal to one) as

$$
\begin{aligned}
H_{12} &= -v^p_{12}H_{11} = -v^p_{12} \\[1ex]
H_{13} &= -v^p_{13}H_{11} = -v^p_{13} \\[1ex]
H_{22} &= \frac{v^p_{12}}{v^p_{21}} H_{11} = \frac{v^p_{12}}{v^p_{21}} \\[1ex]
H_{23} &= \frac{-v^p_{23}v^p_{12}}{v^p_{21}} H_{11} = \frac{-v^p_{23}v^p_{12}}{v^p_{21}} \\[1ex]
H_{33} &= \frac{v^p_{13}}{v^p_{31}} H_{11} = \frac{v^p_{13}}{v^p_{31}}
\end{aligned}
\tag{2.40}
$$

where the shown coefficients are based solely on the plastic Poisson's ratios. The final

three flow law coefficients H_{44}, H_{55} and H_{66}, are determined using the same fit technique

as in the simplified case, but each shear curve must be fit with the 1-direction test acting

as the baseline. These are calculated by fitting the effective stress versus effective plastic

strain curves of the shear tests with the baseline uniaxial test. In order to fit the shear

curves with the uniaxial curve and find the optimal flow rule coefficient value, H^*_{ll}, the

difference between the two curves is minimized as

$$f(\mathrm{H}_{ll}) = \sum_{k=1}^{n} \left[\left(\hat{\sigma}_{ii} \right)_k - \left(\hat{\sigma}_{ij} \right)_k \right]^2 \qquad (2.41)$$

such that

$$H_{ll}^{\min} \le H_{ll}^{*} \le H_{ll}^{\max}$$

where n is the number of data points in the master curve, $\left(\hat{\sigma}_{ii} \right)_k$ is the kth effective stress

value from the baseline curve and $\left(\hat{\sigma}_{ij} \right)_k$ is the effective stress value for the shear curve.

2.3 Convexity of the Yield Surface

The current yield stresses are determined using a curve search of a set of input

stress-strain curves. Each of the 12 input curves is stored as stress versus total effective

plastic strain, thus allowing the model to describe different hardening properties in each

direction. By tracking the effective plastic strain in the deformation model, the evolution

of the yield stresses in the various coordinate directions can then be correlated to the

current value of the effective plastic strain. The Tsai-Wu based yield function, used as

the yield surface to track plasticity, is quite general and can result in both convex and

concave yield surfaces. The yield surface used in the elasto-plastic deformation model

must be convex, as the radial return procedure employed for the numerical

implementation of the model utilizes the value of the yield function to determine if the

stress state has returned to the yield surface. It should be noted that plasticity theory in

general requires a convex yield surface (R. Goldberg, K. Carney and P. DuBois, et al.

2016). If the original input parameters do not produce an appropriate convex yield

surface, a convex correction procedure must be implemented. An example of a non-

convex yield surface that is modified to render it convex is shown in Fig. 5. The off-axis stress values were corrected, as explained later, to make the surface convex.
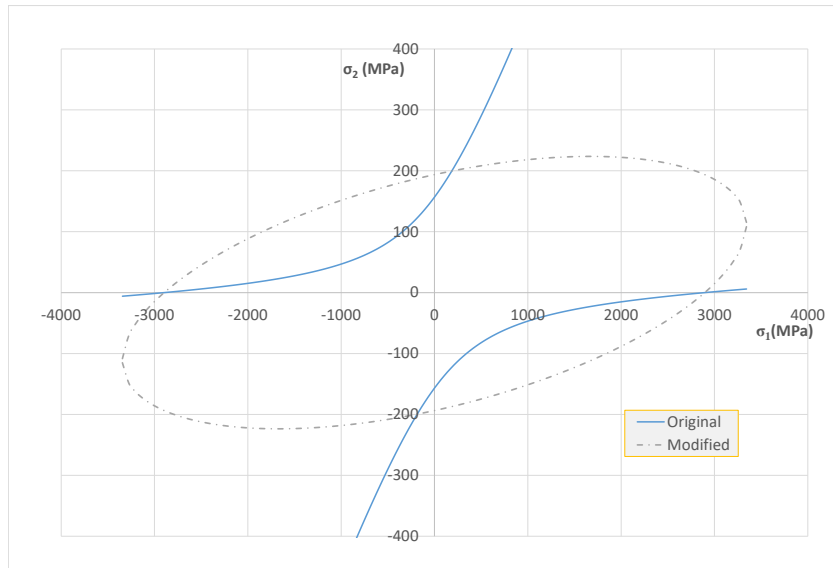
(a)
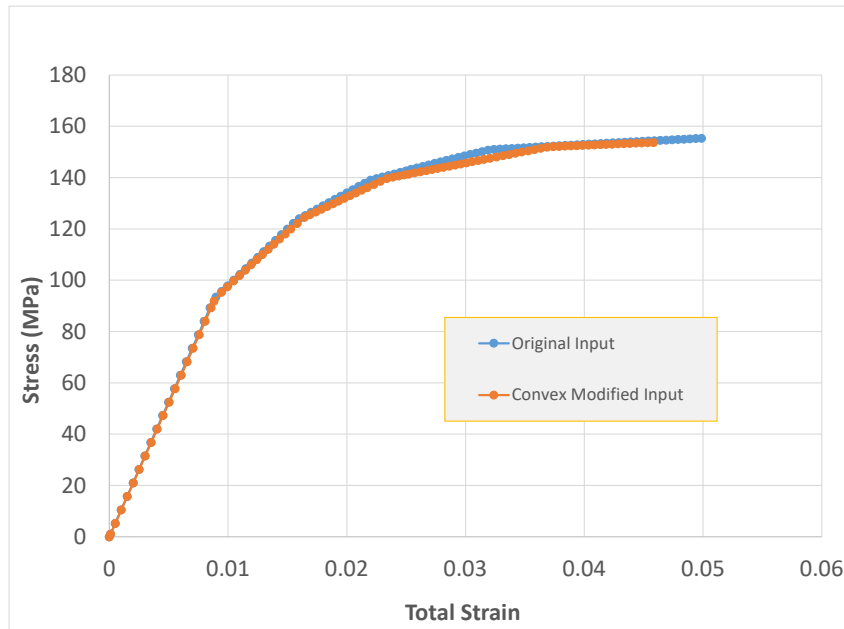
(b)

Fig. 5. (a) Non-Convex and Modified Convex Yield Surfaces (b) Modification of Original Stress-Strain Curve to Yield a Fully Convex Stress-Strain Curve

34

In order for the yield surface to remain convex, the following conditions must be met (adapted from Eqn. (2.18), derived for convexity of the plastic potential function):

$$F_{11} \geq 0, F_{22} \geq 0, F_{33} \geq 0, F_{44} \geq 0, F_{55} \geq 0, F_{66} \geq 0$$
$$F_{11}F_{22} - F_{12}^2 \geq 0, F_{33}F_{22} - F_{23}^2 \geq 0, F_{11}F_{33} - F_{31}^2 \geq 0 \tag{2.42}$$

Note that the diagonal terms are always positive and the final three conditions must be satisfied. One way of ensuring convexity is by modifying the off-axis terms (F_{12}, F_{23}, F_{31}) while retaining the original values of the diagonal terms (F_{11}, F_{22}, F_{33}).

The convexity satisfying conditions of the shear terms can be represented as

$$F_{ij} \leq \sqrt{F_{ii}F_{jj}} \tag{2.43}$$

However, by making the condition more restrictive, the modified off-axis values can be found such that the convexity condition is satisfied more readily, and in a form that is more commonly used in the original Tsai-Wu failure criterion, as

$$F_{ij}' = -\frac{1}{2}\sqrt{F_{ii}F_{jj}} \tag{2.44}$$

Allowing for the off-axis yield stress values to be modified for convexity, the right-hand sides of Eqns. (2.7), (2.8) and (2.9) can be set equal to the value obtained from Eqn. (2.44) thus allowing for the determination of a modified yield stress in a particular direction. For example, for the case of the off-axis tension test in the 1-2 plane, the modified value of the yield stress required to ensure the yield stress is convex can be determined as follows:

$$F'_{12} = \frac{2}{\left(\sigma'^{45}_{12}\right)^2} - \frac{F_1 + F_2}{\sigma'^{45}_{12}} - \frac{1}{2}\left(F_{11} + F_{22} + F_{44}\right)$$

$$\frac{2}{\left(\sigma'^{45}_{12}\right)^2} - \frac{F_1 + F_2}{\sigma'^{45}_{12}} - \frac{1}{2}\left(F_{11} + F_{22} + F_{44}\right) - F'_{12} = 0$$

$$2 - \left(F_1 + F_2\right)\sigma'^{45}_{12} - \frac{1}{2}\left(F_{11} + F_{22} + F_{44}\right)\left(\sigma'^{45}_{12}\right)^2 - F'_{12}\left(\sigma'^{45}_{12}\right)^2 = 0$$

$$a\left(\sigma'^{45}_{12}\right)^2 + b\sigma'^{45}_{12} - 2 = 0 \tag{2.45}$$

where

$$a = F'_{12} + \frac{1}{2}\left(F_{11} + F_{22} + F_{44}\right)$$
$$b = F_1 + F_2$$

and σ'^{45}_{12} is the corrected off-axis yield stress value. If the tension and compression

responses are the same (yield stress values the same for a given direction), the linear

coefficients $\left(F_1, F_2, F_3\right)$ are equal to zero and Eqn. (2.45) can be simplified as

$$\sigma'^{45}_{12} = \sqrt{\frac{2}{a}} \tag{2.46}$$

This convexity must be ensured through all time steps and iterations. In practice, at any

point where the yield function is determined, convexity must first be checked and if non-

convex, the required off-axis yield coefficients and stresses for convexity are calculated

based on Eqns. (2.44) and (2.46).

2.4 Temperature and Strain Rate Dependencies

Strain rate and temperature dependent material response is incorporated into the

elasto-plastic material model using tabulated experimental input data derived from the

same 12 tests detailed earlier. These effects are important for impact simulation due to the high load rate and associated increased localized temperatures at the point of impact. If strain rate and/or temperature effects need to be modeled, multiple curves, for each of the 12 experimental tests, performed at different strain rates are used as input data for the model. All of the strain rate and temperature dependent curves are modified the same way as described earlier and converted to stress versus effective plastic strain, explained in Chapter 3. The interpolation is necessary between the different strain rate curves, based on the strain rate at a given time step, when updating the yield stresses during the plasticity algorithm, in Eqn. (2.30). Additionally, the elastic moduli are interpolated based on the strain rate and temperature dependent input data.

For the case of the off-axis curves, the strain rate associated with the principal material directions (PMD) are not readily available. Thus, the strain rates associated with the off-axis tests must be calculated using a transformation of the material axis system strain rate values. The material model subroutine (MAT213) receives the deformation rate tensor in the global X-Y-Z coordinate system from the finite element analysis (LS-DYNA). Within the MAT213 subroutine, the tensor components are transformed to the PMDs (1-2-3 system) as

$$\mathbf{d} = \begin{bmatrix} d_{11} & d_{22} & d_{33} & d_{12} & d_{23} & d_{13} \end{bmatrix} \tag{2.47}$$

The deformation rate tensor can be written in terms of the small incremental strain tensor if the magnitudes of the displacement gradients are small, $\left| \partial u_i / \partial x_j \right| \ll 1$. Thus the deformation rate tensor can be written as

$$\dot{\boldsymbol{\varepsilon}} = \begin{bmatrix} \dot{\varepsilon}_{11} & \dot{\varepsilon}_{22} & \dot{\varepsilon}_{33} & \dot{\varepsilon}_{12} & \dot{\varepsilon}_{23} & \dot{\varepsilon}_{13} \end{bmatrix} = \begin{bmatrix} d_{11} & d_{22} & d_{33} & 0.5d_{12} & 0.5d_{23} & 0.5d_{13} \end{bmatrix} \tag{2.48}$$

37

The transformation of the principal strain rates can be performed to obtain the associated 45° off-axis terms as

$$\dot{\boldsymbol{\varepsilon}}'_{3\times3} = \mathbf{a}_{3\times3}\dot{\boldsymbol{\varepsilon}}_{3\times3}\mathbf{a}^T_{3\times3} \tag{2.49}$$

where the transformation tensor $\mathbf{a}$ can be defined for each off-axis case as

$$\mathbf{a}^{45}_{1-2} = \begin{bmatrix} 0.707 & 0.707 & 0 \\ -0.707 & 0.707 & 0 \\ 0 & 0 & 1 \end{bmatrix} \tag{2.50}$$

$$\mathbf{a}^{45}_{2-3} = \begin{bmatrix} 1 & 0 & 0 \\ 0 & 0.707 & 0.707 \\ 0 & -0.707 & 0.707 \end{bmatrix} \tag{2.51}$$

$$\mathbf{a}^{45}_{1-3} = \begin{bmatrix} 0.707 & 0 & -0.707 \\ 0 & 1 & 0 \\ 0.707 & 0 & 0.707 \end{bmatrix} \tag{2.52}$$

The corresponding diagonal component of the resulting transformed strain rate tensors, $\dot{\boldsymbol{\varepsilon}}'$, are needed to define the corresponding resultant off-axis strain rates and are calculated using Eqns. (2.50), (2.51) and (2.52) in Eqn. (2.49). Therefore, the resultant strain rates for the off-axis tests, given strain rates in the principal axis can be written as

$$\dot{\varepsilon}^{45}_{1\text{-}2} = \dot{\varepsilon}'_{11} = 0.5\dot{\varepsilon}_{11} + \dot{\varepsilon}_{12} + 0.5\dot{\varepsilon}_{22} \tag{2.53}$$

$$\dot{\varepsilon}^{45}_{2\text{-}3} = \dot{\varepsilon}'_{22} = 0.5\dot{\varepsilon}_{22} + \dot{\varepsilon}_{23} + 0.5\dot{\varepsilon}_{33} \tag{2.54}$$

$$\dot{\varepsilon}^{45}_{1\text{-}3} = \dot{\varepsilon}'_{33} = 0.5\dot{\varepsilon}_{11} + \dot{\varepsilon}_{13} + 0.5\dot{\varepsilon}_{33} \tag{2.55}$$

The input curves for the principal directions account for compression and tension for use in defining the yield surface. Hence care must be taken when using the strain rates corresponding to the three principal directions (Eqn. (2.48)), since they can be either positive (tension) or negative (compression). Thus, if the PMD strain rate is positive,

38

then the tension strain rate value is taken as that, whereas the compression strain rate value would be zero (quasi-static) and vice-versa. This procedure is outlined below.

$$if \ \dot{\varepsilon}_{ii} > 0 \ then \ \dot{\varepsilon}_{ii}^t = \dot{\varepsilon}_{ii} \ and \ \dot{\varepsilon}_{ii}^c = 0$$
$$elseif \ \dot{\varepsilon}_{ii} < 0 \ then \ \dot{\varepsilon}_{11}^c = \dot{\varepsilon}_{11} \ and \ \dot{\varepsilon}_{ii}^t = 0$$
$$else \ \dot{\varepsilon}_{ii}^t = 0 \ and \ \dot{\varepsilon}_{ii}^c = 0$$

2.5 Incorporation of Damage in the Elasto-Plastic Material Model

2.5.1 Introduction of Damage Formulation

The material model is modified to include orthotropic damage. This is achieved by using a tensorial damage framework that permits the anisotropic damage necessary for many composites (Matzenmiller, Lubliner and Taylor 1995). A simplified compliance tensor, from a full 3D case, for a plane stress case can be defined as (from classic continuum damage mechanics formulation)

$$\mathbf{H(\omega)} = \begin{bmatrix} \dfrac{1}{(1-\omega_{11})E_{\parallel}} & \dfrac{v_{21}}{(1-\omega_{22})E_{\parallel}} & 0 \\ \dfrac{v_{12}}{(1-\omega_{11})E_{\perp}} & \dfrac{1}{(1-\omega_{22})E_{\perp}} & 0 \\ 0 & 0 & \dfrac{1}{(1-\omega_{12})G} \end{bmatrix} \quad (2.56)$$

where $\mathbf{H}$ is the damaged compliance tensor, $\mathbf{\omega}$ is the vector of non-negative damage parameters consisting of ω_{ij}, $E_{\parallel}$ is the elastic modulus in the longitudinal direction, $E_{\perp}$ is the elastic modulus in the transverse direction, and v_{ij} are the elastic Poisson's ratios. The damage is coupled in terms of the principal material directions in order to allow for

modeling of composites that show such behavior. However, the damage is decoupled from plasticity, assuming the damage does not affect the plastic strain tensor, and is achieved by using the principle of strain equivalence as opposed to energy equivalence. The damage is then plastic damage and is a function of the plastic deformation, or effective plastic strain. For example, considering uncoupled scalar damage, the effective stress, defined as the undamaged stress state, can be written as

$$\boldsymbol{\sigma}_{eff}^{n} = \frac{\boldsymbol{\sigma}^{n}}{1-d^{n}} \tag{2.57}$$

where $\boldsymbol{\sigma}_{eff}$ is the effective stress state, $\boldsymbol{\sigma}$ is the calculated (assuming no damage) stress state, d is the damage parameter and the superscript n denotes the current time step. However, using deformation mechanics to model the nonlinear composite material response, the effective stress can be written in terms of plasticity, from Eqn. (2.27), as

$$\dot{\boldsymbol{\sigma}}_{eff} = \mathbf{C}\left(\dot{\boldsymbol{\varepsilon}} - \dot{\boldsymbol{\varepsilon}}_{p}\right) \tag{2.58}$$

where each term has been previously described. Thus, the damage evolution can be defined as a function of the plastic strain and effective stress due to plasticity as $d^{n+1} = f\left(\varepsilon_{p}^{n+1}, \boldsymbol{\sigma}_{eff}^{n+1}\right)$, from which the evolution of the stress state can be defined as

$$\boldsymbol{\sigma}^{n+1} = \boldsymbol{\sigma}_{eff}^{n+1}\left(1-d^{n+1}\right) \tag{2.59}$$

An example for a perfectly plastic response with damage is shown for a uniaxial case in Fig. 6.
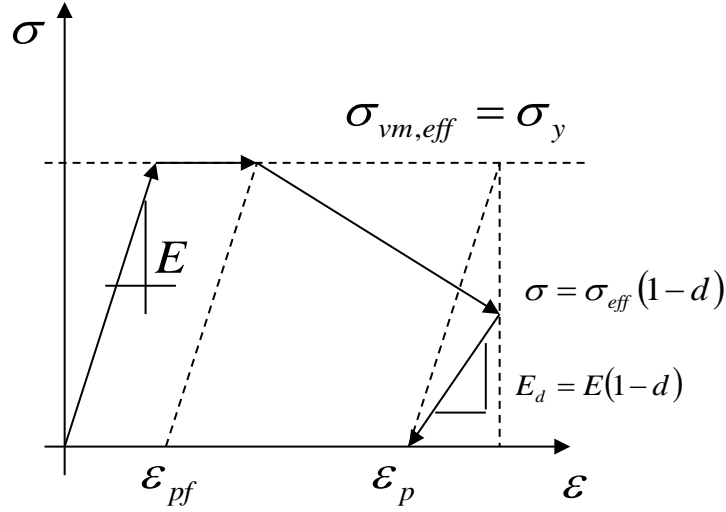
Fig. 6. Elastic-Perfectly Plastic Response With Damage

The strain equivalence of the damage parameter can be shown by substituting Eqn. (2.58)

into Eqn. (2.59), with the strains unchanged between the damaged and undamaged state

with a damaged and undamaged constitutive matrix, resulting in

$$\boldsymbol{\sigma} = \boldsymbol{\sigma}_{eff} \left(1 - d\right)$$
$$\boldsymbol{\sigma} = \left[\mathbf{C}\left(\dot{\boldsymbol{\varepsilon}} - \dot{\boldsymbol{\varepsilon}}_p\right)\right]\left(1 - d\right)$$
$$\boldsymbol{\sigma} = \left(1 - d\right)\mathbf{C}\left(\dot{\boldsymbol{\varepsilon}} - \dot{\boldsymbol{\varepsilon}}_p\right)$$

$$\mathbf{C}_d = \left(1 - d\right)\mathbf{C} \tag{2.60}$$

where $\mathbf{C}_d$ is the damaged 3D constitutive matrix for scalar damage. The incremental

stress is written in terms of the incremental damage effective stress as

$$\boldsymbol{\sigma} = \boldsymbol{\sigma}_{eff}\left(1 - d\right) \quad \rightarrow \quad \boldsymbol{\sigma}_{eff} = \frac{\boldsymbol{\sigma}}{1 - d}$$
$$\dot{\boldsymbol{\sigma}} = \dot{\boldsymbol{\sigma}}_{eff}\left(1 - d\right) - \frac{\dot{d}}{1 - d}\boldsymbol{\sigma} \quad \rightarrow \quad \dot{\boldsymbol{\sigma}}_{eff} = \mathbf{C}\left(\dot{\boldsymbol{\varepsilon}} - \dot{\boldsymbol{\varepsilon}}_p\right)$$
$$\Rightarrow \dot{\boldsymbol{\sigma}} = \mathbf{C}\left(\dot{\boldsymbol{\varepsilon}} - \dot{\boldsymbol{\varepsilon}}_p\right)\left(1 - d\right) - \frac{\dot{d}}{1 - d}\boldsymbol{\sigma}$$

41

$$\dot{\boldsymbol{\sigma}} = \mathbf{C}_d \left(\dot{\boldsymbol{\varepsilon}} - \dot{\boldsymbol{\varepsilon}}_p \right) - \frac{\dot{d}}{1-d} \boldsymbol{\sigma} \tag{2.61}$$

In this framework, it is important to note that the damaged constitutive matrix represents the damaged modulus (secant modulus) and not tangent modulus, indicative of the plastic deformation.

2.5.2 Implemented Damage Model Overview

The deformation portion of the material model provides the majority of the capability of the model to simulate the nonlinear stress-strain response of the composite. However, in order to capture the nonlinear unloading and local softening of the stress-strain response often observed in composites (Barbero 2013), a complementary damage law is required. In the damage law formulation, strain equivalence is assumed (described above), in which for every time step the total, elastic and plastic strains in the actual and effective stress spaces are the same (Lemaitre and Desmorat 2005). The utilization of strain equivalence permits the plasticity and damage calculations to be uncoupled, as all of the plasticity computations can take place in the effective stress space.

In the damage model implemented here, the actual stresses are related to the effective (undamaged) stresses by use of a damage tensor $\mathbf{M}$.

$$\boldsymbol{\sigma} = \mathbf{M} \boldsymbol{\sigma}_{eff} \tag{2.62}$$

The effective stress rate tensor can be related to the total and plastic strain rate tensors by use of the standard elasto-plastic constitutive equation

$$\dot{\boldsymbol{\sigma}}_{eff} = \mathbf{C} \left(\dot{\boldsymbol{\varepsilon}} - \dot{\boldsymbol{\varepsilon}}_p \right) \tag{2.63}$$

42

where **C** is the standard elastic stiffness matrix and the actual total and plastic strain rate tensors are used due to the strain equivalence assumption.

2.5.3 Validation of Strain Equivalence Assumption

As discussed in the previous section, employing the strain equivalence assumption implies that the effective stresses result in the same deformations in the effective, undamaged material as would be caused by applying the actual stresses on the damaged material. In this way, the yield function, constitutive equation and flow rule specified in Eqns. (2.1), (2.19) and (2.63), respectively, can be written in terms of the effective stresses and applied in effective stress space.

For the strain equivalence formulation to be valid, the derivative of the plastic potential function (written in terms of the effective stresses) with respect to the effective stresses must equal the derivative of a damaged plastic potential (written in terms of the actual stresses) with respect to the actual stresses. This concept is expressed mathematically below.

$$\frac{\partial h\left(\boldsymbol{\sigma}_{eff}\right)}{\partial \boldsymbol{\sigma}_{eff}} = \frac{\partial h\left(\mathbf{M}^{-1}\boldsymbol{\sigma}\right)}{\partial \mathbf{M}^{-1}\boldsymbol{\sigma}} = \frac{\partial h_d\left(\boldsymbol{\sigma}\right)}{\partial \boldsymbol{\sigma}} \tag{2.64}$$

Therefore, for the strain equivalence assumption to be valid, appropriate damaged versions of the elastic stiffness matrix, yield function and plastic potential function need to be developed such that the same strain state results whether the material is loaded in the actual or effective stress space.

To develop the damaged elastic stiffness matrix, first Eqn. (2.62) is differentiated and Eqn. (2.63) is substituted in leading to the following expression

$$\dot{\boldsymbol{\sigma}} = \mathbf{M}\dot{\boldsymbol{\sigma}}_{eff} + \dot{\mathbf{M}}\boldsymbol{\sigma}_{eff}$$

$$\dot{\boldsymbol{\sigma}} = \mathbf{MC}\left(\dot{\boldsymbol{\varepsilon}} - \dot{\boldsymbol{\varepsilon}}_p\right) + \dot{\mathbf{M}}\mathbf{M}^{-1}\boldsymbol{\sigma} \qquad (2.65)$$

For the case of elastic only loading the plastic strain rate and the time derivative of the

damage tensor are both set equal to zero, leading to the following results which define a

damaged elastic stiffness matrix $\mathbf{C}_d$

$$\dot{\boldsymbol{\sigma}} = \mathbf{MC}\dot{\boldsymbol{\varepsilon}}$$

$$\dot{\boldsymbol{\sigma}}_{eff} = \mathbf{C}\dot{\boldsymbol{\varepsilon}} \qquad (2.66)$$

$$\mathbf{C}_d = \mathbf{MC}$$

This damaged elastic stiffness matrix will generate the same strains under loading in

actual stress space as the undamaged stiffness matrix would in effective stress space.

In a similar fashion, as shown below, the yield function from Eqn. (2.1) can be written in

a quadratic form in terms of the effective stresses and converted to be in terms of the

actual stresses (using Eqn. (2.62)). A damaged yield function f_d can be defined as

$$f = \mathbf{f}^T\boldsymbol{\sigma}_{eff} + \boldsymbol{\sigma}_{eff}^T\mathbf{F}\boldsymbol{\sigma}_{eff} - 1 \le 0$$

$$f = \mathbf{f}^T\mathbf{M}^{-1}\boldsymbol{\sigma} + \boldsymbol{\sigma}^T\mathbf{M}^{-T}\mathbf{F}\mathbf{M}^{-1}\boldsymbol{\sigma} - 1 \le 0$$

$$\qquad (2.67)$$

$$f_d = \mathbf{f}_d^T\boldsymbol{\sigma} + \boldsymbol{\sigma}^T\mathbf{F}_d\boldsymbol{\sigma} - 1 \le 0$$

$$\mathbf{f}_d = \mathbf{M}^{-T}\mathbf{f}$$

$$\mathbf{F}_d = \mathbf{M}^{-T}\mathbf{F}\mathbf{M}^{-1}$$

To determine the damaged form of the plastic potential function, first the definition of the

plastic potential function given in Eqn. (2.10) is written in terms of effective stresses,

converted into a matrix form, and differentiated with respect to the effective stresses,

resulting in the following expression

$$h = \left(\boldsymbol{\sigma}_{eff}^T\mathbf{H}\boldsymbol{\sigma}_{eff}\right)^{0.5} \Rightarrow \frac{\partial h_{eff}}{\partial \boldsymbol{\sigma}_{eff}} = \frac{1}{2h}2\mathbf{H}\boldsymbol{\sigma}_{eff} = \frac{1}{2\left(\boldsymbol{\sigma}^T\mathbf{M}^{-T}\mathbf{H}\mathbf{M}^{-1}\boldsymbol{\sigma}\right)^{0.5}}2\mathbf{H}\left[\mathbf{M}^{-1}\boldsymbol{\sigma}\right] \quad (2.68)$$

44

where the effective stresses have been converted back into the actual stresses and the **H** matrix is the collection of coefficients for the plastic potential function, written as

$$\mathbf{H} = \begin{bmatrix} H_{11} & H_{12} & H_{31} & 0 & 0 & 0 \\ H_{12} & H_{22} & H_{23} & 0 & 0 & 0 \\ H_{31} & H_{32} & H_{33} & 0 & 0 & 0 \\ 0 & 0 & 0 & H_{44} & 0 & 0 \\ 0 & 0 & 0 & 0 & H_{55} & 0 \\ 0 & 0 & 0 & 0 & 0 & H_{66} \end{bmatrix} \tag{2.69}$$

By applying the results of Eqn. (2.68) in Eqn. (2.19), the plastic strain rate tensor in actual stress space can be defined and a damaged version of the **H** matrix defined in Eqn. (2.69) can be derived as

$$\dot{\boldsymbol{\varepsilon}}_p = \frac{\dot{\lambda}}{2h}2\mathbf{H}\boldsymbol{\sigma}_{eff} = \frac{\dot{\lambda}}{2\left(\boldsymbol{\sigma}^T\mathbf{M}^{-T}\mathbf{H}\mathbf{M}^{-1}\boldsymbol{\sigma}\right)^{0.5}}2\mathbf{H}\left[\mathbf{M}^{-1}\boldsymbol{\sigma}\right] = \dot{\lambda}2\mathbf{H}_d\boldsymbol{\sigma}$$

$$\mathbf{H}_d = \frac{1}{2\left(\boldsymbol{\sigma}^T\mathbf{M}^{-T}\mathbf{H}\mathbf{M}^{-1}\boldsymbol{\sigma}\right)^{0.5}}\mathbf{H}\left[\mathbf{M}^{-1}\right] \tag{2.70}$$

For the strain equivalence assumption to be valid for the given plastic potential function based on the expression shown in Eqn. (2.64), a damaged version of the plastic potential function h_d needs to be defined such that the following expression is true.

$$\frac{\partial h_d\left(\boldsymbol{\sigma}\right)}{\partial \boldsymbol{\sigma}} = \frac{1}{2\left(\boldsymbol{\sigma}^T\mathbf{M}^{-T}\mathbf{H}\mathbf{M}^{-1}\boldsymbol{\sigma}\right)^{0.5}}2\mathbf{H}\left[\mathbf{M}^{-1}\boldsymbol{\sigma}\right] \tag{2.71}$$

By taking the derivative of the proposed function with respect to the actual stresses, the required expression (shown in Eqn. (2.71)) is obtained thus demonstrating that the strain equivalence assumption can be employed.

$$h_d = \mathbf{M}^T\left(\boldsymbol{\sigma}^T\mathbf{M}^{-T}\mathbf{H}\mathbf{M}^{-1}\boldsymbol{\sigma}\right)^{0.5}$$

$$\frac{\partial h_d}{\partial \boldsymbol{\sigma}} = \mathbf{M}^T\frac{1}{2\left(\boldsymbol{\sigma}^T\mathbf{M}^{-T}\mathbf{H}\mathbf{M}^{-1}\boldsymbol{\sigma}\right)^{0.5}}2\mathbf{M}^{-T}\mathbf{H}\left[\mathbf{M}^{-1}\boldsymbol{\sigma}\right]$$

$$\frac{\partial h_d}{\partial \boldsymbol{\sigma}} = \frac{1}{2\left(\boldsymbol{\sigma}^T \mathbf{M}^{-T} \mathbf{H} \mathbf{M}^{-1} \boldsymbol{\sigma}\right)^{0.5}} 2\mathbf{H}\left[\mathbf{M}^{-1}\boldsymbol{\sigma}\right] \tag{2.72}$$

Since an appropriate damage stiffness matrix, yield function and plastic potential function can be defined in the actual (damaged) stress space, the strain equivalence assumption is thus determined to be valid for the deformation and damage model developed in this effort.

2.5.4 Definition and Characterization of Damage Tensor

As specified in Eqn. (2.62), the effective and actual stresses are related through a damage tensor. Given the usual assumption that the actual stress tensor and the effective stress tensor are symmetric, Eqn. (2.62) can be rewritten in the following form, where the damage tensor $\mathbf{M}$ is assumed to have a maximum of 36 independent components.

$$\begin{pmatrix} \sigma_{11} \\ \sigma_{22} \\ \sigma_{33} \\ \sigma_{12} \\ \sigma_{23} \\ \sigma_{31} \end{pmatrix} = \left[\mathbf{M}\right] \begin{pmatrix} \sigma_{11}^{eff} \\ \sigma_{22}^{eff} \\ \sigma_{33}^{eff} \\ \sigma_{12}^{eff} \\ \sigma_{23}^{eff} \\ \sigma_{31}^{eff} \end{pmatrix} \tag{2.73}$$

The damage tensor is assumed to be diagonal, leading to the following form

$$\left[\mathbf{M}\right] = \begin{bmatrix} M_{11} & 0 & 0 & 0 & 0 & 0 \\ 0 & M_{22} & 0 & 0 & 0 & 0 \\ 0 & 0 & M_{33} & 0 & 0 & 0 \\ 0 & 0 & 0 & M_{44} & 0 & 0 \\ 0 & 0 & 0 & 0 & M_{55} & 0 \\ 0 & 0 & 0 & 0 & 0 & M_{66} \end{bmatrix} \tag{2.74}$$

46

A diagonal damage tensor is commonly used in composite damage mechanics theories ((Matzenmiller, Lubliner and Taylor 1995), (Barbero 2013)), and is desirable since a uniaxial load in the actual stress space would result in a uniaxial load in the effective stress space. However, using a diagonal damage tensor generally implies that loading the composite in a particular coordinate direction only leads to a stiffness reduction in the direction of the load. However, several recent experimental studies ((Ogasawara, et al. 2005), (Salavatian and Smith 2014), Salem and Wilmoth, unpublished data, 2015) have shown that in actual composites, particularly those with complex fiber architectures, a load in one coordinate direction can lead to stiffness reductions in multiple coordinate directions. To account for this damage interaction while maintaining a diagonal damage tensor, each term in the diagonal damage matrix should be a function of the plastic strains in each of the normal and shear coordinate directions, as follows for the example of the M_{11} term for the plane stress case

$$M_{11} = M_{11}\left(\varepsilon_{11}^{p}, \varepsilon_{22}^{p}, \varepsilon_{12}^{p}\right) \tag{2.75}$$

To explain this concept further, assume a plastic strain is applied in the 1-direction to an undamaged specimen, with an original area A_{11} perpendicular to the 1 axis and an original area A_{22} perpendicular to the 2-axis. The undamaged modulus in the 1-direction is E_{11} and the undamaged modulus in the 2-direction is equal to E_{22}. The specimen is damaged due to the plastic strain. The original specimen is unloaded and reloaded elastically in the 1-direction. Due to the damage, the reloaded specimen has a reduced area in the x-direction of A_{11}^{d11} and a reduced modulus in the 1-direction of E_{11}^{d11}.

The reduced area and modulus are a function of the damage induced by the plastic strain in the 1-direction as follows

$$
\begin{aligned}
E_{11}^{d11} &= \left(1 - d_{11}^{11}\left(\varepsilon_{11}^{p}\right)\right)E_{11} \\
A_{11}^{d11} &= \left(1 - d_{11}^{11}\left(\varepsilon_{11}^{p}\right)\right)A_{11}
\end{aligned}
\tag{2.76}
$$

where d_{11}^{11} is the damage in the 1-direction due to a load in the 1-direction, which can be generalized as d_{ij}^{kl}, where the damage is in kl due to loading along ij. Alternatively, if the damaged specimen is reloaded elastically in the 2-direction, due to the assumed damage coupling the reloaded specimen would have a reduced area in the 2-direction of A_{22}^{d11} and a reduced modulus in the 2-direction of E_{22}^{d11} due to the load in the 1-direction. The reduced area and modulus are again a function of the damage induced by the plastic strain in the 1-direction as follows

$$
\begin{aligned}
E_{22}^{d11} &= \left(1 - d_{11}^{22}\left(\varepsilon_{11}^{p}\right)\right)E_{22} \\
A_{22}^{d11} &= \left(1 - d_{11}^{22}\left(\varepsilon_{11}^{p}\right)\right)A_{22}
\end{aligned}
\tag{2.77}
$$

where d_{11}^{22} is the damage in the 2-direction due to a load in the 1-direction. Similar arguments can be made and equations developed for the situation where the original specimen is loaded plastically in the 2-direction.

For the case of multiaxial loading, the semi-coupled formulation needs to account for the fact that as the load is applied in a particular coordinate direction, the loads are acting on damaged areas due to the loads in the other coordinate directions, and the load in particular direction is just adding to the damaged area. For example, if one loaded the material in the 2-direction first, the reduced area in the 1-direction would be equal to A_{11}^{d22} and the reduced modulus in the 1-direction would be equal to E_{11}^{d22}. If one would

then subsequently load the material in the 1-direction, the baseline area in the 1-direction would not equal the original area A_{11}, but the reduced area A_{11}^{d22}. Likewise, the baseline modulus in the 1-direction would not be equal to the original modulus E_{11}, but instead the reduced modulus E_{11}^{d22}. Therefore, the loading in the 1-direction would result in the following further reduction in the area and modulus in the 1-direction

$$
\begin{aligned}
E_{11}^{d11} &= \left(1-d_{11}^{11}\left(\varepsilon_{11}^{p}\right)\right)E_{11}^{d22} = \left(1-d_{11}^{11}\left(\varepsilon_{11}^{p}\right)\right)\left(1-d_{22}^{11}\left(\varepsilon_{22}^{p}\right)\right)E_{11} \\
A_{11}^{d11} &= \left(1-d_{11}^{11}\left(\varepsilon_{11}^{p}\right)\right)A_{11}^{d22} = \left(1-d_{11}^{11}\left(\varepsilon_{11}^{p}\right)\right)\left(1-d_{22}^{11}\left(\varepsilon_{22}^{p}\right)\right)A_{11}
\end{aligned}
\tag{2.78}
$$

These results suggest that the relation between the actual stress and the effective stress should be based on a multiplicative combination of the damage terms as opposed to an additive combination of the damage terms. For example, in the case of plane stress, the relation between the actual and effective stresses could be expressed as follows

$$
\begin{aligned}
\sigma_{11} &= \left(1-d_{11}^{11}\right)\left(1-d_{22}^{11}\right)\left(1-d_{12}^{11}\right)\sigma_{11}^{eff} \\
\sigma_{22} &= \left(1-d_{11}^{22}\right)\left(1-d_{22}^{22}\right)\left(1-d_{12}^{22}\right)\sigma_{22}^{eff} \\
\sigma_{12} &= \left(1-d_{11}^{12}\right)\left(1-d_{22}^{12}\right)\left(1-d_{12}^{12}\right)\sigma_{12}^{eff}
\end{aligned}
\tag{2.79}
$$

Note that for the full three-dimensional case, the stress in a particular coordinate direction is a function of the damage due to loading in all of the coordinate directions (1, 2, 3, 12, 31 and 23). By using a polynomial to describe the damage, the coupled terms represent the reduction to the degree of damage resulting from the fact that in a multiaxial loading case the area reductions are combined.

There are two primary items needed for model characterization and input for the damage portion of the material model. First of all, the values of the various damage parameter terms d_{ij}^{kl} need to be defined in a tabulated manner as a function of the effective plastic strain. In addition, the various input stress-strain curves need to be

49

converted into plots of effective (undamaged) stress versus effective plastic strain. As an example of how this process could be carried out, assume that a material is loaded unidirectionally in the 1-direction. At multiple points once the actual stress-strain curve has become nonlinear, the total strain ε_{11}, actual stress σ_{11} and average local, damaged modulus E_{11}^{d11} can be measured. Assuming that the original, undamaged modulus E_{11} is known, since the damage in the 1-direction is assumed to be only due to load in the 1-direction (due to the uniaxial load), the damage parameters and effective stress in the 1-direction can be computed at a particular point along the stress-strain curve as follows

$$1 - d_{11}^{11} = \frac{E_{11}^{d11}}{E_{11}}$$

$$M_{11} = 1 - d_{11}^{11}$$

$$\sigma_{11}^{eff} = \frac{\sigma_{11}}{M_{11}}$$

$$\varepsilon_{11}^{p} = \varepsilon_{11} - \frac{\sigma_{11}^{eff}}{E_{11}} \tag{2.80}$$

These values need to be determined at multiple points in order to fully characterize the evolution of damage as the plastic strain increases.

With this information, an effective stress versus plastic strain $\left(\varepsilon_{11}^{p} \right)$ plot can be generated. From this plot, the effective plastic strain corresponding to the plastic strain in the 1-direction at any particular point can be determined by using the equations shown below, which are based on applying the principal of the equivalence of plastic work in combination with Eqn. (2.10), simplifying the expressions for the case of unidirectional loading in the 1-direction (R. Goldberg, K. Carney and P. DuBois, et al. 2014).

$$h = \sqrt{H_{11}\left(\sigma_{11}^{eff}\right)^2}$$

$$\varepsilon_e^p = \int \frac{\sigma_{11}^{eff} d\varepsilon_{11}^p}{h}$$

(2.81)

From this data, plots of the effective stress in the 1-direction versus the effective plastic

strain as well as plots of the damage parameter d_{11}^{11} as a function of the effective plastic

strain can be generated. By measuring the damaged modulus in the other coordinate

directions at each of the measured values of plastic strain in the 1-direction, the value of

the damage parameters $d_{11}^{22}, d_{11}^{12}, d_{11}^{33}$, etc. can be determined as a function of the plastic

strain in the 1-direction, and thus as a function of the effective plastic strain. Similar

procedures can be carried out for the case of plastic loading in the other coordinate

directions to determine the other needed damage terms.

To convert the 45º off-axis stress-strain curves into plots of the effective

(undamaged) stress versus effective plastic strain, the total and plastic strain (permanent

strain after unload) in the structural axis x-direction needs to be measured at multiple

points along the stress-strain curve. Given the undamaged modulus E_{xx}, and utilizing the

strain equivalence hypothesis, the effective stress in the structural axis system x-direction

can be computed as follows:

$$\sigma_{xx}^{eff} = E_{xx}\left(\varepsilon_{xx} - \varepsilon_{xx}^p\right)$$

(2.82)

Given the effective stress in the structural axis system, the effective stresses in the

material axis system can be generated by use of stress transformation equations. Using

the material axis system stresses, the plastic potential function and effective plastic strain

corresponding to each value of plastic strain can be determined using the principal of the

51

equivalence of plastic work in combination with Eqn. (2.10) as shown below (R.

Goldberg, K. Carney and P. DuBois, et al. 2014).

$$\sigma_{11}^{eff} = 0.5\sigma_{xx}^{eff}$$
$$\sigma_{22}^{eff} = 0.5\sigma_{xx}^{eff}$$
$$\sigma_{12}^{eff} = -0.5\sigma_{xx}^{eff}$$
$$h = 0.5\sigma_{xx}^{eff}\sqrt{H_{11} + H_{22} + 2H_{12} + H_{44}}$$
$$\varepsilon_e^p = \int \frac{\sigma_{xx}^{eff} d\varepsilon_{xx}^p}{h} \tag{2.83}$$

Chapter 3: Numerical Implementation

In this chapter details of the numerical implementation of the theory discussed in Chapter 2, are shown and discussed. The focus is on the deformation including rate and temperature effects, and damage models.

The following sets of data are needed as input to the model:

1. Twelve true stress versus true strain curves at a prescribed strain rate and a prescribed temperature from (a) uniaxial tension tests in 1, 2 and 3-directions, (b) uniaxial compression tests in 1, 2 and 3-directions, (c) shear in 1-2, 2-3 and 3-1 planes, and (d) off-axis (e.g., 45 degrees) uniaxial tension or compression in 1-2, 2-3 and 3-1 planes are required in a tabulated x-y data form. The number of such data sets is a function of the material's behavior as a function of strain rate and temperature dependence.

2. The modulus of elasticity, Poisson's ratio and average plastic Poisson's ratio (averaged over the entire nonlinear portion of the stress-strain curve) obtained from the tension and compression tests are also required. The basic elastic properties are required for the elastic portion of the deformation analysis, and the plastic Poisson's ratios are needed to compute the coefficients in the plastic potential function.

3. Damage parameters, as a function of the total effective plastic strain, are required for the damage model, relating the damage in material direction with respect to a prescribed loading direction. The complete list of damage parameters is shown below. However, if there is no damage in a particular direction or damage coupling between two directions, the corresponding damage parameter can be

assumed to be zero. This reduces the total number of required damage parameters. The damage parameters required to fully define the damage tensor are listed in the Table 3 where tests in green are uncoupled and tests in yellow are coupled (stored and updated in $\hat{\mathbf{d}}$ vector).

Table 3. Damage Parameters

Input	Source	Input	Source
$d_{11}^{11}(\varepsilon_e^p)$	T1/C1 unload/reload in 1-direction	$d_{33}^{33}(\varepsilon_e^p)$	T3/C3 unload/reload in 3-direction
$d_{22}^{11}(\varepsilon_e^p)$	T2/C2 unload/reload in 1-direction	$d_{23}^{33}(\varepsilon_e^p)$	S23 unload/reload in 3-direction
$d_{33}^{11}(\varepsilon_e^p)$	T3/C3 unload/reload in 1-direction	$d_{13}^{33}(\varepsilon_e^p)$	S13 unload/reload in 3-direction
$d_{12}^{11}(\varepsilon_e^p)$	S12 unload/reload in 1-direction	$d_{11}^{12}(\varepsilon_e^p)$	T1/C1 unload/reload in 12-direction
$d_{13}^{11}(\varepsilon_e^p)$	S13 unload/reload in 1-direction	$d_{22}^{12}(\varepsilon_e^p)$	T2/C2 unload/reload in 12-direction
$d_{11}^{22}(\varepsilon_e^p)$	T1/C1 unload/reload in 2-direction	$d_{12}^{12}(\varepsilon_e^p)$	S12 unload/reload in 12-direction
$d_{22}^{22}(\varepsilon_e^p)$	T2/C2 unload/reload in 2-direction	$d_{22}^{23}(\varepsilon_e^p)$	T2/C2 unload/reload in 23-direction
$d_{33}^{22}(\varepsilon_e^p)$	T3/C3 unload/reload in 2-direction	$d_{33}^{23}(\varepsilon_e^p)$	T3/C3 unload/reload in 23-direction
$d_{12}^{22}(\varepsilon_e^p)$	S12 unload/reload in 2-direction	$d_{23}^{23}(\varepsilon_e^p)$	S23 unload/reload in 23-direction
$d_{23}^{22}(\varepsilon_e^p)$	S23 unload/reload in 2-direction	$d_{11}^{13}(\varepsilon_e^p)$	T1/C1 unload/reload in 13-direction
$d_{11}^{33}(\varepsilon_e^p)$	T1/C1 unload/reload in 3-direction	$d_{33}^{13}(\varepsilon_e^p)$	T3/C3 unload/reload in 13-direction
$d_{22}^{33}(\varepsilon_e^p)$	T2/C2 unload/reload in 3-direction	$d_{13}^{13}(\varepsilon_e^p)$	S13 unload/reload in 13-direction

The first six flow rule coefficients are computed directly from the assumed flow rule coefficient value and the plastic Poisson's ratios - see Eqn. (2.40). The last three flow rule coefficients (H_{44}, H_{55}, H_{66}) are calculated by using the fitting technique described in Eqn. (2.41).

Each set of the twelve input curves are normalized with respect to the effective plastic strain, where the effective plastic strain can be expressed in terms of the experimental stress versus total strain data. For the compressive response in the 1-direction, for example, this is written as

$$
\left.\begin{array}{l}
\sigma_{11}^{c}\left(\varepsilon_{11}^{p}=\varepsilon_{11}-\dfrac{\sigma_{11}^{c}}{E_{11}}\right) \\[2ex]
\varepsilon_{e}^{p}=\int\left(\sigma_{11}d\varepsilon_{11}^{p}/h\right)
\end{array}\right\} \Rightarrow \sigma_{11}^{c}\left(\varepsilon_{e}^{p}\right)
\tag{3.1}
$$

where σ_{11}^{c} is the experimental compressive true stress in the 1-direction, ε_{11} is the total true strain in the 1-direction, E_{11} is the elastic modulus in the 1-direction, ε_{11}^{p} is the true plastic strain in the 1-direction, ε_{e}^{p} is the effective plastic strain and h is the value of the effective stress, as shown in Eqn. (2.10).

Once the input curves are fully normalized, the plasticity algorithm is initiated. In the following, the subscript "n" refers to the value from the previous time step, the subscript "$n+1$" refers to the value from the current time step, the superscript "i" refers to the value from the previous iteration within a time step, the superscript "$i+1$" refers to the value from the current iteration, and the superscript "$i-1$" refers to the value from the 2nd iteration prior to the current iteration. To numerically implement the material model, a typical elastic stress update is applied as follows

$$
\boldsymbol{\sigma}_{n+1}=\boldsymbol{\sigma}_{n}+\mathbf{C}\Delta t:\left(\dot{\boldsymbol{\varepsilon}}-\dot{\boldsymbol{\varepsilon}}^{p}\right)
\tag{3.2}
$$

where $\mathbf{C}$ is the orthotropic elastic stiffness matrix, Δt is the time step, $\dot{\boldsymbol{\varepsilon}}$ is the total strain rate and $\dot{\boldsymbol{\varepsilon}}^{p}$ is the plastic strain rate as defined in Eqn. (2.19). The elastic stiffness matrix is written in terms of the compliance matrix as

55

$$\mathbf{C} = \mathbf{S}^{-1} = \begin{bmatrix} \dfrac{1}{E_{11}} & -\dfrac{v_{21}}{E_{22}} & -\dfrac{v_{31}}{E_{33}} & 0 & 0 & 0 \\ & \dfrac{1}{E_{22}} & -\dfrac{v_{32}}{E_{33}} & 0 & 0 & 0 \\ & & \dfrac{1}{E_{33}} & 0 & 0 & 0 \\ & & & \dfrac{1}{G_{23}} & 0 & 0 \\ & Sym & & & \dfrac{1}{G_{31}} & 0 \\ & & & & & \dfrac{1}{G_{12}} \end{bmatrix}^{-1} \tag{3.3}$$

where E_{ii} are the elastic moduli in the principal material directions, G_{ij} are the elastic

shear moduli and v_{ij} are the elastic Poisson's ratios. The elastic moduli values shown

above are interpolated based on the temperature and strain rate data. The current values

of the yield stresses used to determine the yield function coefficients are summarized into

a single vector, Eqn. (2.29), corresponding to data obtained from each of the 12 input

experimental test curves with the rate of change represented as

$$\dot{\mathbf{q}} = \dot{\lambda}\frac{d\mathbf{q}}{d\lambda} \tag{3.4}$$

The vector of yield stress values is updated during the strain hardening process,

adjusted yield stresses are checked for convexity, and if necessary the off-axis terms are

based on convexity conditions using Eqns. (2.44) and (2.46). The yield stresses in the

various coordinate directions are assumed to evolve as a function of the effective plastic

strain. Lastly, as defined in Eqn. (2.28) and expanded here, the plasticity consistency

condition is written in terms of the gradient of the yield function as

$$\dot{f} = \frac{\partial f}{\partial \boldsymbol{\sigma}}\dot{\boldsymbol{\sigma}} + \frac{\partial f}{\partial \mathbf{q}}\dot{\mathbf{q}} = 0 \tag{3.5}$$

which establishes the requirement for the stress state to remain on the yield surface; hence the inclusion of the yield stress vector. Eqns. (2.19) and (3.2) can be applied within Eqn. (3.5) to obtain the following expression

$$\dot{f} = \frac{\partial f}{\partial \boldsymbol{\sigma}} \left(\mathbf{C} : \dot{\boldsymbol{\varepsilon}} - \mathbf{C} : \lambda \frac{\partial h}{\partial \boldsymbol{\sigma}} \right) + \frac{\partial f}{\partial \mathbf{q}} \lambda \frac{d\mathbf{q}}{d\lambda} = 0$$

(3.5)a

where $\dot{\boldsymbol{\sigma}}$ is written in terms of the stiffness matrix and total and plastic strain rates, and the rate of change in the yield stresses has been expanded using Eqn. (3.4). As discussed earlier, due to the strain hardening formulation applied in the plasticity law, the plastic multiplier λ can be shown to be equal to the effective plastic strain. Solving for the effective plastic strain rate produces the following consistency equation, which is utilized within the numerical algorithm to compute an estimate used for the evolution of the effective plastic strain

$$\lambda = \frac{\dfrac{\partial f}{\partial \boldsymbol{\sigma}} \mathbf{C} : \dot{\boldsymbol{\varepsilon}}}{\dfrac{\partial f}{\partial \boldsymbol{\sigma}} \mathbf{C} : \dfrac{\partial h}{\partial \boldsymbol{\sigma}} + \dfrac{\partial f}{\partial \mathbf{q}} \dfrac{d\mathbf{q}}{d\lambda}}$$

(3.6)

To start the calculations for a particular time step, the current values of the yield stresses, set equal to the original yield stresses until initial yield occurs, and set equal to the yield stresses corresponding to the current value of the effective plastic strain after initial yield occurs, are set in the vector $\mathbf{q}$ shown in Eqn. (3.4). These current yield stresses are also used in Eqns. (2.5), (2.7), (2.8) and (2.9) to compute the initial estimate of the coefficients of the yield function for the time step. To compute the increment in effective plastic strain (and the resulting stress state) for a particular time step, a variation of the radial return algorithm, commonly used in plasticity analysis (Khan and Huang

57

1995), is employed. To initiate the algorithm, a perfectly elastic response is assumed. Therefore, an elastic predictor is used to compute an initial estimate for the stresses at the end of the time step as follows

$$\left(\boldsymbol{\sigma}\right)^e = \left(\boldsymbol{\sigma}\right)^n + \mathbf{C}\Delta t : \left(\dot{\boldsymbol{\varepsilon}}\right) \tag{3.7}$$

With the elastic trial stresses computed, a trial yield function value can be calculated from Eqn. (2.1) using the current values of the yield stresses to determine if the load step is elastic or plastic by applying the following expression:

$$f\left(\boldsymbol{\sigma}^e, \mathbf{q}^n\right) \leq 0 \ ?, \ if \ yes \Rightarrow elastic \begin{cases} \boldsymbol{\sigma}^{n+1} = \boldsymbol{\sigma}^e \\ \Delta\lambda = 0 \end{cases} \tag{3.8}$$

If the value of the yield function is less than zero, the time step is assumed to be an elastic time step, the values of the stresses at the end of the time step are set equal to the elastic trial stresses, and the algorithm continues to the next time step. If the value of the yield function is greater than zero, the time step is assumed to be a plastic time step, and the radial return algorithm must be employed to bring the stress state back to the yield surface by computing a converged value for the increment in effective plastic strain, $\Delta\lambda$. If the trial yield function is greater than zero, then $\Delta\lambda > 0$ must be true. The value of $\Delta\lambda_i$ (i is the iteration number) is determined using a secant iteration, with $\Delta\lambda_i^1 = 0$ for the first iteration (assuming a purely elastic response). An estimate for a second iterative value for the effective plastic strain is determined from the consistency equation, Eqn. (3.6), as

$$\Delta\lambda_i^2 = \frac{\left.\dfrac{\partial f}{\partial \boldsymbol{\sigma}}\right|_e : \left(\boldsymbol{\sigma}^e - \boldsymbol{\sigma}^n\right)}{\left.\dfrac{\partial f}{\partial \boldsymbol{\sigma}}\right|_e \mathbf{C} : \left.\dfrac{\partial h}{\partial \boldsymbol{\sigma}}\right|_e + \dfrac{\partial f}{\partial \mathbf{q}}\dfrac{d\mathbf{q}}{d\lambda}} \approx \frac{\left.\dfrac{\partial f}{\partial \boldsymbol{\sigma}}\right|_e : \left(\boldsymbol{\sigma}^e - \boldsymbol{\sigma}^n\right)}{\left.\dfrac{\partial f}{\partial \boldsymbol{\sigma}}\right|_e \mathbf{C} : \left.\dfrac{\partial h}{\partial \boldsymbol{\sigma}}\right|_e} \tag{3.9}$$

58

where the derivatives of $\mathbf{q}$ are taken as zero, meaning that the response is assumed to be perfectly plastic. If a negative estimate for the increment in effective plastic strain is computed, the effective plastic strain increment value is either set equal to the value of total effective plastic strain, if not zero (after initial yield is reached), or the absolute value of the strain increment (until initial yield is reached). The partial derivatives of the yield function and the plastic potential function with respect to the stresses can be evaluated from Eqns. (2.1) and (2.10), respectively, as

$$\frac{\partial f}{\partial \boldsymbol{\sigma}} = \begin{bmatrix} F_1 + 2F_{11}\sigma_{11} + 2F_{12}\sigma_{22} + 2F_{13}\sigma_{33} \\ F_2 + 2F_{12}\sigma_{11} + 2F_{22}\sigma_{22} + 2F_{23}\sigma_{33} \\ F_3 + 2F_{13}\sigma_{11} + 2F_{23}\sigma_{22} + 2F_{33}\sigma_{33} \\ F_{44}\sigma_{12} \\ F_{55}\sigma_{23} \\ F_{66}\sigma_{31} \end{bmatrix} \tag{3.10}$$

$$\frac{\partial h}{\partial \boldsymbol{\sigma}} = \frac{1}{2h} \begin{bmatrix} 2H_{11}\sigma_{11} + 2H_{12}\sigma_{22} + 2H_{13}\sigma_{33} \\ 2H_{12}\sigma_{11} + 2H_{22}\sigma_{22} + 2H_{23}\sigma_{33} \\ 2H_{13}\sigma_{11} + 2H_{23}\sigma_{22} + 2H_{33}\sigma_{33} \\ H_{44}\sigma_{12} \\ H_{55}\sigma_{23} \\ H_{66}\sigma_{31} \end{bmatrix} \tag{3.11}$$

By assuming a condition of perfect plasticity in the second iteration, the stress state is ensured to return to the interior of the yield surface, thus resulting in a negative value of the yield function. If a negative value of the yield function is not obtained, the estimate for the effective plastic strain increment is doubled and the process is repeated until a negative yield function value is reached. By utilizing this procedure for the first two iterations the solution is bounded, which helps to ensure a reasonable convergence

59

towards the actual increment in effective plastic strain for the time step. Once the

increment in effective plastic strain $\Delta\lambda$, is computed for the second iteration, the

corresponding stresses (including a plastic correction from the elastic trial stresses), can

be computed using a modified version of Eqn. (3.2), where the stiffness matrix

multiplied by the total strain is set equal to the elastic trial stress, and the plastic strain is

written in terms of the effective plastic strain increment and the gradient of the plastic

potential function evaluated using the elastic trial stresses.

$$\boldsymbol{\sigma}_{n+1} = \boldsymbol{\sigma}^e - \mathbf{C} : \Delta\lambda \left. \frac{\partial h}{\partial \boldsymbol{\sigma}} \right|_e \tag{3.12}$$

These modified stresses can then be used to compute a new estimate of the value

of the yield function for the second iteration of the secant iteration process. Given the

estimates of the effective plastic strain and value of the yield function for the first two

iterations, a secant process can be used to compute a revised estimate, to be used in a

third iteration, of the effective plastic strain

$$\Delta\lambda^3 = \Delta\lambda^1 - f^1 \frac{\Delta\lambda^2 - \Delta\lambda^1}{f^2 - f^1} \tag{3.13}$$

In the above equation the superscript represents the iteration number corresponding to the

given term. A revised estimate of the stresses for the third iteration within the time step

is calculated using a revised version of Eqn. (3.12), where the gradient of the plastic

potential function is computed using the stresses computed during the second iteration

and the effective plastic strain value computed for the third iteration is employed.

$$\boldsymbol{\sigma}\big|_{n+1}^3 = \boldsymbol{\sigma}^e - \mathbf{C} : \Delta\lambda^3 \left. \frac{\partial h}{\partial \boldsymbol{\sigma}} \right|_{\Delta\lambda^2} \tag{3.14}$$

Based on these revised stresses, the value of the yield function for the third

iteration is computed. At this point, convergence of the secant iteration can be checked by

applying the following conditions

$$
\begin{aligned}
&f_3 \approx 0 \Rightarrow \Delta\lambda = \Delta\lambda^3; \\
&f_3 > 0 \Rightarrow \begin{cases} \Delta\lambda^1 = \Delta\lambda^3, f^1 = f\big|_{n+1}^3 \\ \Delta\lambda^2 = \Delta\lambda^2, f^1 = f\big|_{n+1}^1 \end{cases}; \\
&f_3 < 0 \Rightarrow \begin{cases} \Delta\lambda^1 = \Delta\lambda^1, f^1 = f\big|_{n+1}^1 \\ \Delta\lambda^2 = \Delta\lambda^3, f^2 = f\big|_{n+1}^3 \end{cases}
\end{aligned}
\tag{3.15}
$$

If the value of the yield function is not less than some predefined tolerance, the secant

iteration process is continued. To continue the secant iterations, the increment of the

effective plastic strain used in the next iteration (now generalized to iteration "i+1"), is

computed using an expression similar to Eqn. (3.13)

$$
\Delta\lambda_{n+1}^{i+1} = \Delta\lambda^1 - f^1 \frac{\Delta\lambda^2 - \Delta\lambda^1}{f^2 - f^1}
\tag{3.16}
$$

where the values to be used in the expression are determined based on Eqn. (3.15). The

new estimate for the effective plastic strain is then used to determine a new set of updated

stresses as follows.

$$
\sigma\big|_{n+1}^{i+1} = \sigma_n + \mathbf{C} : \left[\Delta\varepsilon - \Delta\lambda_{n+1}^{i+1} \frac{\partial h}{\partial\sigma}\bigg|_{n+1}^{i} \right]
\tag{3.17}
$$

In this expression, the gradient of the plastic potential function is determined

based on the stresses computed in the previous increment. The rationale for computing

the gradient of the plastic potential function using stresses other than the trial elastic

stresses is based on the fact that due to the anisotropic hardening of the material the yield

61

surface rotates (besides just expanding) as additional plastic strain is applied. The

anisotropic strain hardening results from the fact that the changes in yield stresses in the

various coordinate directions are not necessarily proportional. This concept, which is

displayed schematically in Fig. 7 is discussed in more detail in (R. Goldberg, K. Carney

and P. DuBois, et al. 2016).
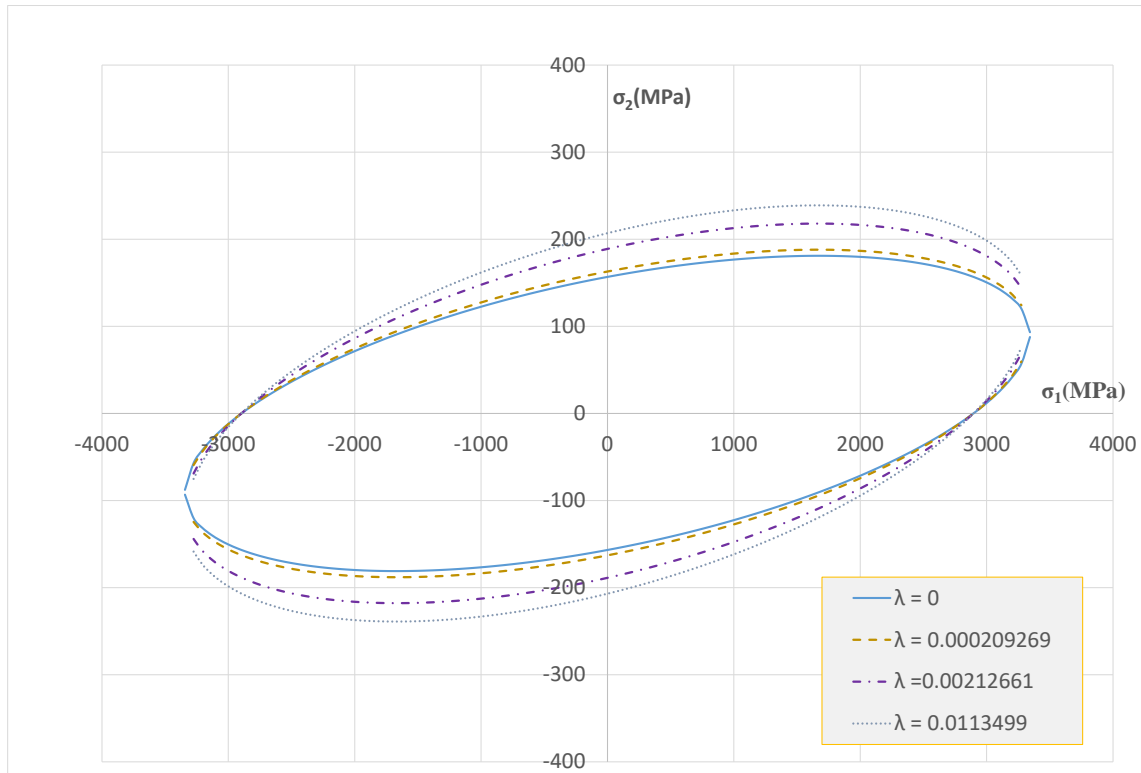
Fig. 7. Anisotropic Yield Surface Evolution in 1-2 Stress Space

After the revised stresses for the new iteration are computed, the yield function

value is evaluated with these updated stresses, and updated yield stresses are computed

based on the new estimate for the effective plastic strain and the input curves. Based on

the revised computed value for the yield function, $f\big|_{n+1}^{i+1}$, convergence is checked and

revised parameters required for the secant method computations of the increments of

effective plastic strain are determined based on the following revised version of Eqn. (3.15).

$$f\big|_{n+1}^{i+1} \approx 0 \Rightarrow \Delta\lambda = \Delta\lambda^{i+1};$$

$$f\big|_{n+1}^{i+1} > 0 \Rightarrow \begin{cases} \Delta\lambda^1 = \Delta\lambda^{i+1}, f^1 = f\big|_{n+1}^{i+1} \\ \Delta\lambda^2 = \Delta\lambda^i, f^2 = f\big|_{n+1}^i \end{cases};$$

$$f\big|_{n+1}^{i+1} < 0 \Rightarrow \begin{cases} \Delta\lambda^1 = \Delta\lambda^{i-1}, f^1 = f\big|_{n+1}^{i-1} \\ \Delta\lambda^2 = \Delta\lambda^{i+1}, f^2 = f\big|_{n+1}^{i+1} \end{cases}$$

(3.18)

If convergence is not reached, the process described in Eqn. (3.16) and Eqn. (3.17) is repeated for a new iteration. Once convergence is satisfied, the appropriate increment of effective plastic strain is known based on the iteration results and the stresses can be updated as

$$\boldsymbol{\sigma}_{n+1} = \boldsymbol{\sigma}^e - \mathbf{C} : \Delta\lambda \frac{\partial h}{\partial \boldsymbol{\sigma}}$$

(3.19)

where the stress values computed in the iteration prior to convergence being reached are used to compute the gradient of the plastic potential function. Finally, the yield stresses are updated as well, using the new value of the overall effective plastic strain, λ, in each input curve to determine the corresponding yield stress level, with respect to the temperature and strain rate, as

$$q_{n+1} = q\left(\lambda_n + \Delta\lambda, \dot{\varepsilon}, T\right)$$

(3.20)

3.1 Modification of Input Stress-Strain Curves for the Damage Model

The input stress-strain curves are converted to stress-effective plastic strain for the deformation plastic algorithm outlined earlier. However, in order to incorporate the same

63

plasticity algorithm with damage, the yield stresses must be determined in an undamaged state. Thus, the stress-strain curves must be converted from true stress (damaged state) to effective stress (undamaged state) before normalizing them with respect to the effective plastic strain. The conversion from true stress to effective stress requires the measurement of either the damaged modulus or plastic strain (by unloading the material to a state of zero stress) at several total strain values as shown in Table 4 for the normal stress-strain relationship.

Table 4. Damaged Modulus and Plastic Strain (Normal Stress-Strain Relationship)

Damaged Modulus	Plastic Strain
$d_{11}^{11} = 1 - \dfrac{E_{11}^{d11}}{E_{11}}$ $M_{11}^{11} = 1 - d_{11}^{11}$ $\sigma_{11}^{eff} = \dfrac{\sigma_{11}}{M_{11}^{11}}$ $\varepsilon_{11}^{p} = \varepsilon_{11} - \dfrac{\sigma_{11}^{eff}}{E_{11}}$	$\sigma_{11}^{eff} = E_{11}\left(\varepsilon_{11} - \varepsilon_{11}^{p}\right)$ $M_{11}^{11} = \dfrac{\sigma_{11}}{\sigma_{11}^{eff}}$ $d_{11}^{11} = 1 - M_{11}^{11}$

Using either approach, both the effective stress and damage parameter can be calculated at sampled values of the total strain. It is important to note here that the number of effective stress versus total strain points will be equal to the amount of unloading steps taken during experimentation. Therefore, the true stress versus total strain curve will have more points than the effective stress versus total strain curve. Hence the desired resolution of the modified data must be considered when determining the number of unloading steps; although interpolation of the damage parameter can be used between the experimentally obtained values. The procedure for the experimental tests to obtain the

uncoupled damage terms is described below, where the damaged modulus and plastic

strain are calculated at each of the unload/reload steps.

Load Steps (Fig. 8):

   a) Load to a damaged point, i.e. point 1.
   b) Unload to a stress-free state, i.e. point 2.
   c) Reload to a strain level past the point of the previously loaded state, i.e. load to
      point 3.
   d) Repeat steps b and c for the desired amount of damage points.
   e) Stop loading when specimen has failed.
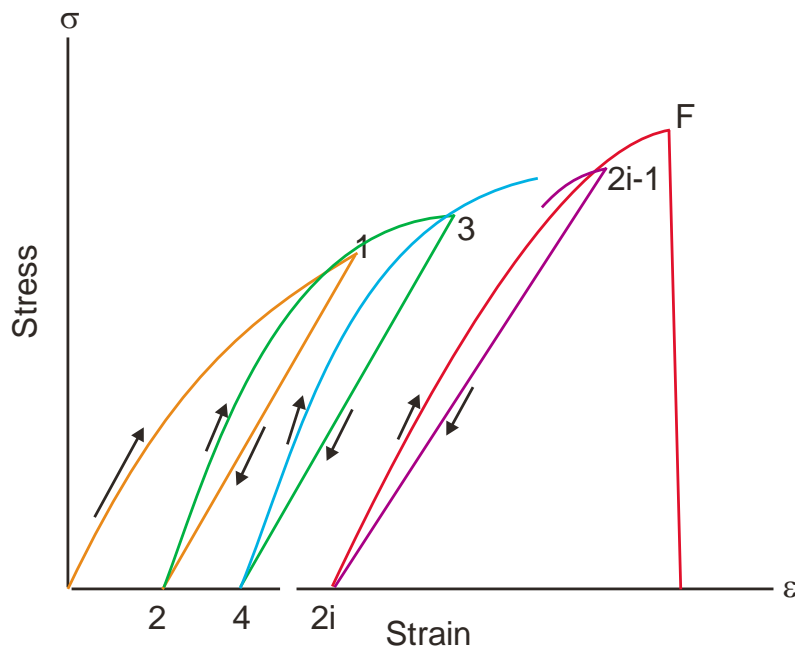
Fig. 8. Loading-Unloading Steps for Characterization of Uncoupled Damage Parameters

Next, the curves are normalized with respect to the effective plastic strain similar to the

deformation model. However, the total stress is replaced by the effective stress as shown

in Eqn. (2.81) for a uniaxial 1-direction loading. The effective stress and damage

parameters are then normalized with respect to the effective plastic strain. First, the

effective stress versus effective plastic strain must be calculated utilizing the damage

(considering only damage in test direction,) with respect to the total strain. Then, the

same process as shown in Eqn. (3.1) with a unidirectional 1-direction test as an example, can be expanded by using the effective stress in place of the true stress resulting in

$$\left.\begin{array}{rl} \sigma_{11}^{eff}\left(\varepsilon_{11}\right) = \dfrac{\sigma_{11}\left(\varepsilon_{11}\right)}{1 - d_{11}^{11}\left(\varepsilon_{11}\right)} & (a) \\[2ex] \sigma_{11}^{eff}\left(\varepsilon_{11}^{p} = \varepsilon_{11} - \dfrac{\sigma_{11}^{eff}}{E_{11}}\right) & (b) \\[2ex] \varepsilon_{e}^{p} = \int\left(\sigma_{11}^{eff} d\varepsilon_{11}^{p} / h\right) & (c) \end{array}\right\} \Rightarrow \sigma_{11}^{eff}\left(\varepsilon_{e}^{p}\right) \qquad\qquad (3.21)$$

where the effective stress is calculated based on the effective stress as well,

$h = \sqrt{H_{11}\left(\sigma_{11}^{eff}\right)^{2}}$. Once the stress-strain curves are converted to effective stress versus effective plastic strain, the damage parameters must also be normalized to the effective plastic strain by correlating the effective plastic stain from the normalized effective stress curves with the total strain values used to calculate the effective stress from the damage parameters. An illustration of the normalization of the effective stress and damage parameters is shown in Fig. 9, resulting in curves (tables) of effective stress and damage parameters as a function of effective plastic strain. The details of these steps are as follows:

1. Convert input stress versus strain curve into effective stress versus strain, using the input damage versus strain curve (in the corresponding material direction) and Eqn. (3.21)a.

2. Convert the effective stress versus strain curve to effective stress versus plastic strain using Eqn. (3.21)b.

3. Convert the effective stress versus plastic strain curve to effective stress versus effective plastic strain using Eqn. (3.21)c.

4. Normalize the input damage versus strain curves to damage versus effective plastic strain using the transformed strain to effective plastic strain relationship of the 12 input stress-strain curves. The damage parameter is normalized using the corresponding loading direction, i.e. for parameter d_{ij}^{kl} the loading direction ij would determine which of the 12 input curves to correlate to.
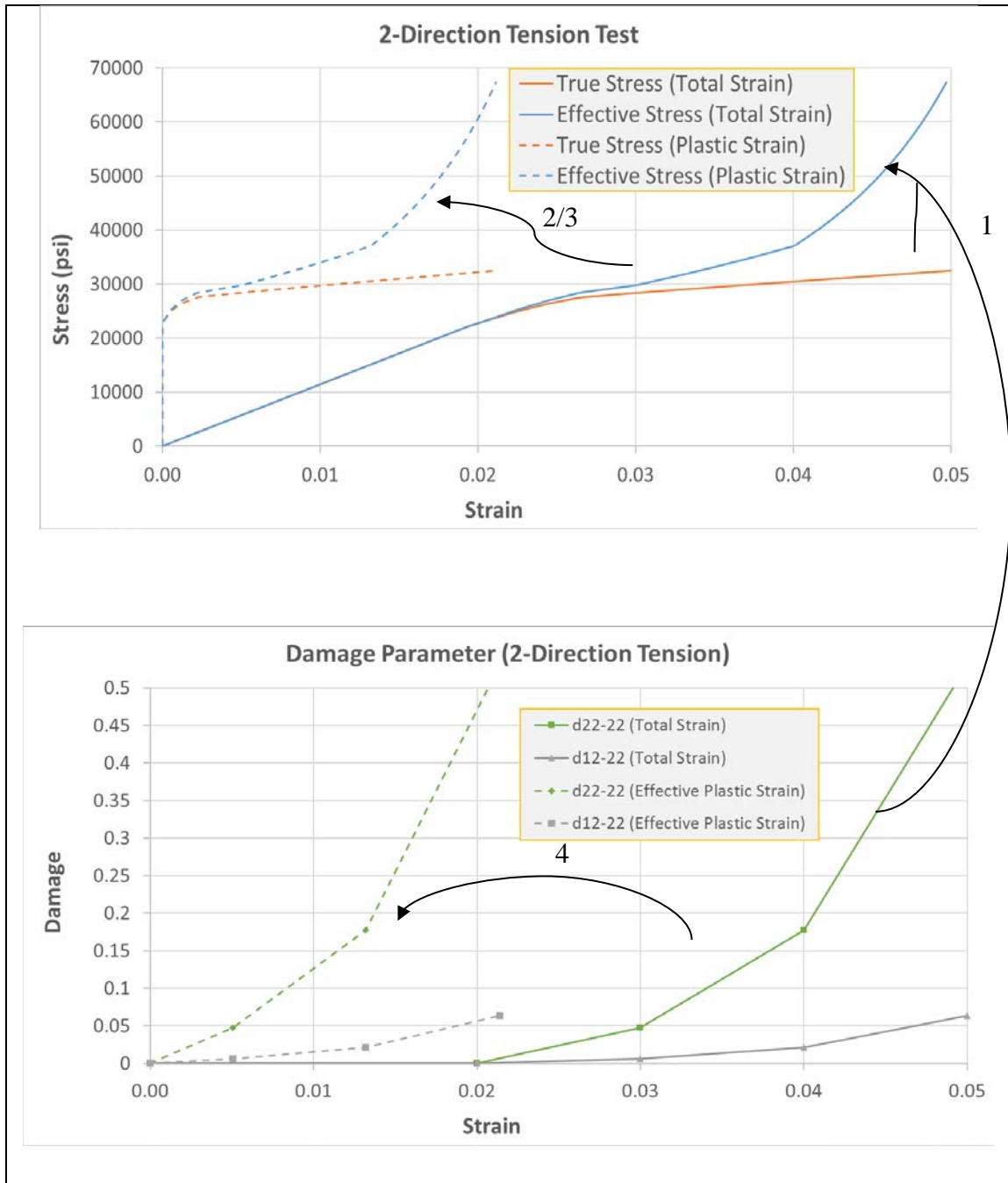
Fig. 9. Normalizing Input Stress vs. Strain and Damage vs. Strain Data to Effective

Plastic Strain

The same process for the unidirectional normal loading case can be applied to the

shear loading condition. As shown in Table 5, where the tensorial shear strains are used,

the procedure for the experimental tests to obtain the uncoupled shear damage terms is

shown in Fig. 8.

Table 5. Damaged Modulus and Plastic Strain (Shear Stress-Strain Relationship)

Damaged Modulus	Plastic Strain
$d_{12}^{12} = 1 - \dfrac{G_{12}^{d12}}{G_{12}}$ $M_{44}^{12} = 1 - d_{12}^{12}$ $\sigma_{12}^{eff} = \dfrac{\sigma_{12}}{M_{44}^{12}}$ $\varepsilon_{12}^{p} = \varepsilon_{12} - \dfrac{\sigma_{12}^{eff}}{2G_{12}}$	$\sigma_{12}^{eff} = 2G_{12}\left(\varepsilon_{12} - \varepsilon_{12}^{p}\right)$ $M_{44}^{12} = \dfrac{\sigma_{12}}{\sigma_{12}^{eff}}$ $d_{xy}^{xy} = 1 - M_{44}^{12}$

The effective stress is then normalized with respect to the effective plastic strain for the

shear case, similar to the unidirectional case, shown below.

$$h = \sqrt{H_{44}\left(\sigma_{12}^{eff}\right)^2}$$
$$\varepsilon_{e}^{p} = 2\left(\int \frac{\sigma_{12}^{eff}\,d\varepsilon_{12}^{p}}{h}\right)$$

(3.22)

The coupled damage parameters (from damaged moduli) can be determined by

elastically loading the damaged sample in the other directions after each unload step,

producing a normalized relationship between the coupled damage parameters with

respect to the effective plastic strain. The coupled damage terms are obtained by testing a

specimen in one direction to a damaged point (in the plastic/non-linear region), then

reloading in another direction elastically just enough to obtain a modulus value without

inducing any additional damage. The steps to obtain the coupled damage are described

below, which follow the same general procedure from the uncoupled tests, with an

additional reloading in the desired damage parameter direction.

69

Load Steps (Fig. 10):

a) Load to a damaged point in ij direction, i.e. point 1.
b) Unload to a stress-free state in the ij direction, i.e. point 2.
c) Change the loading direction to kl. Reload elastically in the kl direction, without inducing any additional damage.
d) Unload to a stress-free state in the kl direction.
e) Change the loading direction to ij. Reload to a strain level past the point of the previous unloading in the ij direction.
f) Repeat steps b-e for the desired amount of damage points.
g) Stop when specimen has failed in the ij direction.
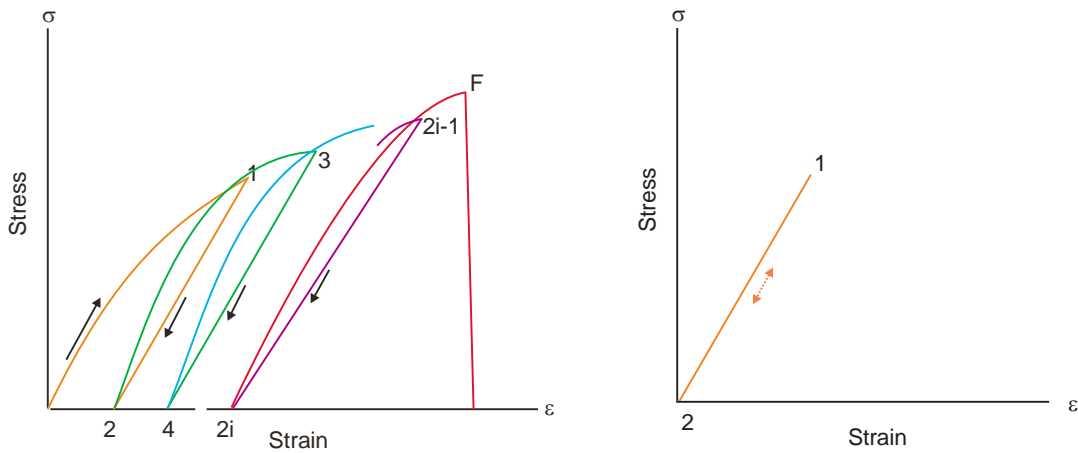
(a) Loading-unloading in the ij direction   (b) Elastic reloading-unloading in the kl direction

Fig. 10. Loading-Unloading Steps for Characterization of Coupled

Damage Parameter d_{ij}^{kl}

Finally, there are no damage parameters obtained from the off-axis tests as the damage parameters are used in the damage tensor to transform the damaged stress state to an undamaged state. However, for use in the plasticity algorithm, the input stress-strain curves from the off-axis test must be converted to effective (undamaged) stress versus effective plastic strain, matching the normal and shear input curves. The effective stress for the 45° off-axis tests is calculated in the structural loading direction as defined in Eqn. (2.82) which is then normalized to the effective plastic strain, with the material direction

70

stresses calculated in terms of the structural axis stresses for the determination of the plastic potential (see Eqn. (2.83)).

3.2 Damage Model for Stress Transformation

The developed damage theory has been tailored to be implemented around the current deformation model (plasticity algorithm), where the damage tensor $\mathbf{M}$ relates the true stresses to the effective stresses as shown in Eqn. (2.73). Note that $\mathbf{M}$ has a maximum of 36 individual components to account for full damage coupling. However, with this approach, a multi-directional loading in the true stress can result from a unidirectional loading in the effective stress which is undesirable. Therefore, a diagonal damage tensor is used with the coupling accounted for in the individual diagonal terms, shown below.

$$
\begin{pmatrix} \sigma_{11} \\ \sigma_{22} \\ \sigma_{33} \\ \sigma_{12} \\ \sigma_{23} \\ \sigma_{13} \end{pmatrix} = \begin{bmatrix} M_{11} & 0 & 0 & 0 & 0 & 0 \\ 0 & M_{22} & 0 & 0 & 0 & 0 \\ 0 & 0 & M_{33} & 0 & 0 & 0 \\ 0 & 0 & 0 & M_{44} & 0 & 0 \\ 0 & 0 & 0 & 0 & M_{55} & 0 \\ 0 & 0 & 0 & 0 & 0 & M_{66} \end{bmatrix} \begin{pmatrix} \sigma_{11}^{eff} \\ \sigma_{22}^{eff} \\ \sigma_{33}^{eff} \\ \sigma_{12}^{eff} \\ \sigma_{23}^{eff} \\ \sigma_{13}^{eff} \end{pmatrix} \tag{3.23}
$$

The six diagonal terms of the damage tensor are comprised of uncoupled and coupled damage terms defined as d_{ij}^{kl}, where the damage is in kl due to loading along ij. Furthermore, we assume:

(i) Normal damage is due to all normal and shear terms, e.g.

$$
\left(1 - d_{11}^{11}\left(\varepsilon_e^p\right)\right)\left(1 - d_{22}^{11}\left(\varepsilon_e^p\right)\right)\left(1 - d_{33}^{11}\left(\varepsilon_e^p\right)\right)\left(1 - d_{12}^{11}\left(\varepsilon_e^p\right)\right)\left(1 - d_{23}^{11}\left(\varepsilon_e^p\right)\right)\left(1 - d_{13}^{11}\left(\varepsilon_e^p\right)\right) = \frac{E_{11}^{dam}}{E_{11}} \tag{3.24}
$$

(ii) Shear damage is due to all normal and shear terms, e.g.

$$\left(1-d_{11}^{12}\left(\varepsilon_e^p\right)\right)\left(1-d_{22}^{12}\left(\varepsilon_e^p\right)\right)\left(1-d_{33}^{12}\left(\varepsilon_e^p\right)\right)\left(1-d_{12}^{12}\left(\varepsilon_e^p\right)\right)\left(1-d_{23}^{12}\left(\varepsilon_e^p\right)\right)\left(1-d_{13}^{12}\left(\varepsilon_e^p\right)\right)=\frac{G_{12}^{dam}}{G_{12}} \quad (3.25)$$

Using the given notation and assumptions, the expanded damage transformation with the six generalized damage terms are shown below.

$$\begin{aligned}
\sigma_{11} &= \left(1-d_{11}^{11}\left(\varepsilon_e^p\right)\right)\left(1-d_{22}^{11}\left(\varepsilon_e^p\right)\right)\left(1-d_{33}^{11}\left(\varepsilon_e^p\right)\right)\left(1-d_{12}^{11}\left(\varepsilon_e^p\right)\right)\left(1-d_{23}^{11}\left(\varepsilon_e^p\right)\right)\left(1-d_{13}^{11}\left(\varepsilon_e^p\right)\right)\sigma_{11}^{eff} \\
\sigma_{22} &= \left(1-d_{11}^{22}\left(\varepsilon_e^p\right)\right)\left(1-d_{22}^{22}\left(\varepsilon_e^p\right)\right)\left(1-d_{33}^{22}\left(\varepsilon_e^p\right)\right)\left(1-d_{12}^{22}\left(\varepsilon_e^p\right)\right)\left(1-d_{23}^{22}\left(\varepsilon_e^p\right)\right)\left(1-d_{13}^{11}\left(\varepsilon_e^p\right)\right)\sigma_{22}^{eff} \\
\sigma_{33} &= \left(1-d_{11}^{33}\left(\varepsilon_e^p\right)\right)\left(1-d_{22}^{33}\left(\varepsilon_e^p\right)\right)\left(1-d_{33}^{33}\left(\varepsilon_e^p\right)\right)\left(1-d_{12}^{11}\left(\varepsilon_e^p\right)\right)\left(1-d_{23}^{33}\left(\varepsilon_e^p\right)\right)\left(1-d_{13}^{33}\left(\varepsilon_e^p\right)\right)\sigma_{33}^{eff} \\
\sigma_{12} &= \left(1-d_{11}^{12}\left(\varepsilon_e^p\right)\right)\left(1-d_{22}^{12}\left(\varepsilon_e^p\right)\right)\left(1-d_{33}^{12}\left(\varepsilon_e^p\right)\right)\left(1-d_{12}^{12}\left(\varepsilon_e^p\right)\right)\left(1-d_{23}^{12}\left(\varepsilon_e^p\right)\right)\left(1-d_{13}^{12}\left(\varepsilon_e^p\right)\right)\sigma_{12}^{eff} \\
\sigma_{23} &= \left(1-d_{11}^{23}\left(\varepsilon_e^p\right)\right)\left(1-d_{22}^{23}\left(\varepsilon_e^p\right)\right)\left(1-d_{33}^{23}\left(\varepsilon_e^p\right)\right)\left(1-d_{12}^{23}\left(\varepsilon_e^p\right)\right)\left(1-d_{23}^{23}\left(\varepsilon_e^p\right)\right)\left(1-d_{13}^{23}\left(\varepsilon_e^p\right)\right)\sigma_{23}^{eff} \\
\sigma_{13} &= \left(1-d_{11}^{13}\left(\varepsilon_e^p\right)\right)\left(1-d_{22}^{23}\left(\varepsilon_e^p\right)\right)\left(1-d_{33}^{13}\left(\varepsilon_e^p\right)\right)\left(1-d_{12}^{12}\left(\varepsilon_e^p\right)\right)\left(1-d_{23}^{23}\left(\varepsilon_e^p\right)\right)\left(1-d_{13}^{13}\left(\varepsilon_e^p\right)\right)\sigma_{13}^{eff}
\end{aligned} \quad (3.26)$$

There are a total of 36 damage parameters not accounting for differences between tension and compression damage and loading terms. If tension and compression terms are identified separately for normal damage, i.e. $\left(\dfrac{E_{11}^{dam}}{E_{11}}\right)^T \neq \left(\dfrac{E_{11}^{dam}}{E_{11}}\right)^C$, then Eqn. (3.24) needs to be rewritten as

$$\left(1-d_{11_T}^{11_T}\left(\varepsilon_e^p\right)\right)\left(1-d_{22_T}^{11_T}\left(\varepsilon_e^p\right)\right)\left(1-d_{33_T}^{11_T}\left(\varepsilon_e^p\right)\right)\left(1-d_{11_C}^{11_T}\left(\varepsilon_e^p\right)\right)\left(1-d_{22_C}^{11_T}\left(\varepsilon_e^p\right)\right)\left(1-d_{33_C}^{11_T}\left(\varepsilon_e^p\right)\right)$$
$$\left(1-d_{12}^{11_T}\left(\varepsilon_e^p\right)\right)\left(1-d_{23}^{11_T}\left(\varepsilon_e^p\right)\right)\left(1-d_{13}^{11_T}\left(\varepsilon_e^p\right)\right)=\left(\frac{E_{11}^{dam}}{E_{11}}\right)^T \quad (3.24)\text{a}$$

$$\left(1-d_{11_T}^{11_C}\left(\varepsilon_e^p\right)\right)\left(1-d_{22_T}^{11_C}\left(\varepsilon_e^p\right)\right)\left(1-d_{33_T}^{11_C}\left(\varepsilon_e^p\right)\right)\left(1-d_{11_C}^{11_C}\left(\varepsilon_e^p\right)\right)\left(1-d_{22_C}^{11_C}\left(\varepsilon_e^p\right)\right)\left(1-d_{33_C}^{11_C}\left(\varepsilon_e^p\right)\right)$$
$$\left(1-d_{12}^{11_C}\left(\varepsilon_e^p\right)\right)\left(1-d_{23}^{11_C}\left(\varepsilon_e^p\right)\right)\left(1-d_{13}^{11_C}\left(\varepsilon_e^p\right)\right)=\left(\frac{E_{11}^{dam}}{E_{11}}\right)^C \quad (3.24)\text{b}$$

It should be noted that $d_{11_T}^{11_T}\left(\varepsilon_e^p\right)$ is a function of tensile plastic strains, $d_{11_C}^{11_T}\left(\varepsilon_e^p\right)$ is a function of compressive plastic strains, $d_{12}^{11_T}\left(\varepsilon_e^p\right)$ is a function of tensile plastic strains, etc. and are used as such depending on the current values in the strain tensor.

Similarly, Eqn. (3.25) needs to be rewritten as

$$\left(1-d_{11_T}^{12}\left(\varepsilon_e^p\right)\right)\left(1-d_{22_T}^{12}\left(\varepsilon_e^p\right)\right)\left(1-d_{33_T}^{12}\left(\varepsilon_e^p\right)\right)\left(1-d_{11_C}^{12}\left(\varepsilon_e^p\right)\right)\left(1-d_{22_C}^{12}\left(\varepsilon_e^p\right)\right)\left(1-d_{33_C}^{12}\left(\varepsilon_e^p\right)\right)$$
$$\left(1-d_{12}^{12}\left(\varepsilon_e^p\right)\right)\left(1-d_{23}^{12}\left(\varepsilon_e^p\right)\right)\left(1-d_{13}^{12}\left(\varepsilon_e^p\right)\right)=\frac{G_{12}^{dam}}{G_{12}} \quad (3.25)\text{a}$$

72

It should be noted that $d_{11_T}^{12}\left(\varepsilon_e^p\right)$ is a function of tensile plastic strains, $d_{11_C}^{12}\left(\varepsilon_e^p\right)$ is a function of compressive plastic strains, etc. and are used as such depending on the current values in the strain tensor. Hence there are 54 damage parameters for the normal equations and 27 damage parameters for the shear equations. In addition, we also have three uncoupled damage terms for the off-axis tests since these damage terms, $d_{12o}^{12o}\left(\varepsilon_e^p\right)$, $d_{23o}^{23o}\left(\varepsilon_e^p\right)$ and $d_{13o}^{13o}\left(\varepsilon_e^p\right)$ are used for only transforming the input stress-strain curves to effective stress-effective plastic strain curves. In conclusion, there are 84 damage parameters.

The damage tensor is utilized in the plasticity algorithm in which the true (damaged) stress state is transformed to the effective (undamaged) state at the beginning each time step. The current plasticity algorithm is then implemented in the same way. The yield stress update utilizes the effective stress versus effective plastic strain rather than the stress versus effective plastic strain. Once the plasticity algorithm has converged, the stresses are then transformed back to the true stress state prior to the stress update, and the damage parameters are updated for the next time step. The stress transformation process is illustrated below.

$$\boldsymbol{\sigma}^{eff} = \mathbf{M}^{-1}\boldsymbol{\sigma} \quad \xrightarrow{plasticity} \quad \boldsymbol{\sigma} = \mathbf{M}\boldsymbol{\sigma}^{eff} \tag{3.27}$$

The damage parameters are then updated similar to the yield stress values. However, the normal tension and compression parameters only accumulate for corresponding tension or compression loading, respectively. The damage vector is updated as

$$\hat{d}_{n+1} = \hat{d}\left(\lambda_n + \Delta\lambda\right) \tag{3.28}$$

A detailed algorithm that has been implemented as a computer code is presented below.

The following parameters are referenced in the algorithm.

δ_{tol} Tolerance value. Default is 10^{-3}.

$n_{\sec\max}$ Maximum number of iterations allowed in the secant method. Default is 100.

n_{double} Maximum times the value of $\Delta\lambda$ is double in order to find a negative value of yield function thus bounding the solution. Default is 100.

Step 1: *Preprocessing (this is executed once immediately after reading the material data)*

Read and store as many sets of 12 stress-strain curves obtained at constant strain rate and temperature as needed; read and store damage-strain curves for damage model, independent of strain rate and temperature. Convert these curves to effective stress versus effective plastic strain using Eqns. (3.1) and (3.21); normalize damage parameters to effective plastic strain. Store initial yield stresses in $\mathbf{q}$, based off the initial strain rate and temperature, and correct for convexity if necessary using Eqns. (2.44) and (2.46); initialize damage parameters in $\hat{\mathbf{d}}$ to zero. Compute optimal values of the flow rule coefficients so as to match the input curves as closely as possible.

The following steps are executed when the material model subroutine is called for each Gauss point in all the elements at every time step.

Step 2: *Initialization*

The following parameters are passed to the subroutine: $\boldsymbol{\sigma}_n$, $(\dot{\boldsymbol{\varepsilon}}_n, \Delta t_n)$.

74

Step 3: *Elastic predictor*

(a) Compute the yield function coefficients using Eqns. (2.5), (2.7), (2.8) and (2.9) for effective yield stresses (based on the current temperature and strain rate.), calculate off-axis coefficients based on convexity conditions using Eqns. (2.44) and (2.46), if necessary.

(b) Construct the elastic stiffness matrix using Eqns. (3.3), (3.24) and (3.25), interpolating the undamaged elastic moduli based on the current temperature and strain rate.

(c) Compute elastic trial stresses, $\boldsymbol{\sigma}_{n+1}^{e}$, using Eqn. (3.2), and transform to effective stress space with Eqns. (3.23) and (3.27).

(d) Compute the trial yield function, f_{n+1}^{trial}, using the elastic trial stresses in Eqn. (2.1). If $f_{n+1}^{trial} \leq \delta_{tol}$, the current state is elastic. Set $\Delta\lambda_{n} = 0$ and go to stress update (Step 5). Else go to plastic corrector (Step 4).

Step 4: *Plastic corrector*

(a) Set $\Delta\lambda^{1} = 0$.

(b) Calculate $\Delta\lambda^{2}$ from Eqn. (3.9).

(c) Compute the new estimate of the stress for each effective plastic strain increment $\left(\Delta\lambda^{1}, \Delta\lambda^{2}\right)$ using Eqn. (3.12).

(d) Calculate the effective plastic strains at the next time step as

$\lambda^{1} = \lambda_{n} + \Delta\lambda^{1}, \lambda^{2} = \lambda_{n} + \Delta\lambda^{2}$.

(e) Update the yield stresses using Eqn. (3.20).

(f) Determine the corresponding yield function coefficients for each increment based on the updated yield stresses using Eqns. (2.5), (2.7), (2.8) and (2.9), calculate off-axis coefficients based on convexity conditions using Eqns. (2.44) and (2.46), if necessary.

(g) Calculate the yield function values using Eqn. (2.1). For a negative $\Delta\lambda^2$: if $\lambda > 0$ set $\Delta\lambda^2 = \lambda$, else if $\lambda = 0$, $\Delta\lambda^2 = abs(\Delta\lambda^2)$.

(h) Calculate the yield function for $\Delta\lambda^2$: if $f_2 < 0$ then use the current value of $\Delta\lambda^2$, else double $\Delta\lambda^2$ until $f_2 < 0$. This doubling is done n_{double} times, to ensure the solution is bounded.

(i) Compute new plastic multiplier increment, $\Delta\lambda^3$ from Eqn. (3.13).

(j) Calculate the updated stresses using Eqn. (3.14) and the new estimate for the yield function, f^3. If $\left|f^3\right| \leq \delta_{tol}$, set $\Delta\lambda = \Delta\lambda^3$, exit the loop and go to stress update (Step 5). Else update secant iteration parameters using Eqn. (3.15) and proceed with secant iterations.

(k) Loop through secant iteration for $n_{sec\,max}$ iterations:

    (i) Calculate new estimate of the increment of effective plastic strain, $\Delta\lambda^{i+1}$, using Eqn. (3.16).

    (ii) Compute the updated stresses for the new estimate of the increment using Eqn. (3.12).

    (iii) Update total effective plastic strain $\lambda_{n+1}^{i+1} = \lambda_n + \Delta\lambda_{n+1}^{i+1}$.

    (iv) Update yield stresses using Eqn. (3.20).

(v) Calculate the yield function value, f^{i+1} using Eqn. (2.1), calculate off-axis coefficients based on convexity conditions using Eqns. (2.44) and (2.46), if necessary.

(vi) Update the derivative of the plastic potential, $\left.\dfrac{\partial h}{\partial \sigma}\right|_{n+1}^{i+1}$.

(vii) If $\left|f^{i+1}\right| \leq yieldtol$, set $\Delta\lambda = \Delta\lambda^{i+1}$, exit the loop and go to stress update. Else update secant iteration parameters using Eqn. (3.18) and go to next step of secant iteration.

 (viii) If secant method hits $n_{\sec\max}$, stop the run with an appropriate error message.

Step 5: *Stress Update*

Calculate $\boldsymbol{\sigma}_{n+1}$ using Eqn. (3.12) and transform back to the true stress space with Eqns. (3.23) and (3.27).

Step 6: *History Variable Update*

Update history variables for plastic work and work hardening parameters ($\mathbf{q}$, $\hat{\mathbf{d}}$ and λ).

(a) Set $\lambda_{n+1} = \lambda_n + \Delta\lambda_n$.

(b) Determine new yield stresses, $\mathbf{q}_{n+1}$, using Eqns. (3.20).

(c) Calculate and store updated damage parameters, $\hat{\mathbf{d}}$, with Eqn. (3.28).

It should be noted that $\boldsymbol{\sigma}_{n+1}$ is updated and passed back from the subroutine for use in the rest of LS-DYNA functionalities.

Chapter 4: Numerical Results

The composite material model is tested and verified using experimental data obtained from T800S/3900-2B[P2352W-19] BMS8-276 Rev-H-Unitape fiber/resin unidirectional composite (Raju and Acosta 2010). Toray describes T800S as an intermediate modulus, high tensile strength graphite fiber. The epoxy resin system is labeled F3900 where a toughened epoxy is combined with small elastomeric particles to form a compliant interface or interleaf between fiber plies to resist impact damage and delamination (Smith and Dow September 1991). Magnified views of the composite are shown in Fig. 11 and Fig. 12.
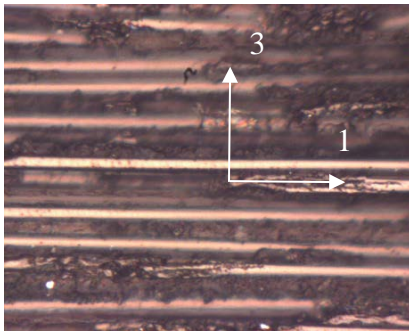
Fig. 11. Side view (Optical Microscopy)
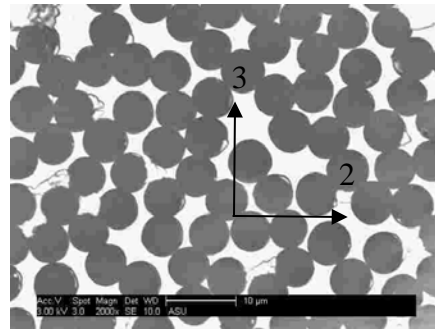
Fig. 12. Longitudinal View (SEM)

The source of the input data for the model (both experimental and virtual) is listed in Table 6. In the Data column, Experimental refers to experimental data generated at Wichita State (Raju and Acosta 2010). MAC-GMC (Bednarcyk and Arnold 2002) and VTSS (Harrington and Rajan 2014) refer to the use of numerical simulation techniques to generate the stress-strain curve at quasi-static (QS) and room temperature (RT) when experimental data are not available. The numerical experiments from MAC-GMC and VTSS were performed to fill in the gaps of available experimental tests, which can often be the case, due to difficulties in tests involving the through-thickness properties.

Table 6. Generation of QS-RT Input Data for T800-F3900 Composite

Curve	Data
Tension Test (1-Direction)	Experimental
Tension Test (2-Direction)	MAC-GMC and VTSS
Tension Test (3-Direction)	Transverse isotropy
Compression Test (1-Direction)	Experimental
Compression Test (2-Direction)	MAC-GMC and VTSS
Compression Test (3-Direction)	Transverse isotropy
Pure Shear Test (1-2 Plane)	Experimental
Pure Shear Test (2-3 Plane)	MAC-GMC and VTSS
Pure Shear Test (1-3 Plane)	Transverse isotropy
Off-Axis Test (45°, 1-2 Plane)	MAC-GMC and VTSS
Off-Axis Test (45°, 2-3 Plane)	MAC-GMC and VTSS
Off-Axis Test (45°, 1-3 Plane)	Transverse isotropy

The fiber (transversely isotropic, linear elastic) and the matrix (isotropic, elasto-plastic) properties are listed in Table 7. The properties for the latter are not publicly available. The procedure to calculate the values is shown in Section 4.3, with the fiver properties provided by the manufacturer.

Table 7. T800-F3900 Fiber and Matrix Properties (Volume Fraction = 0.54)

Property	Fiber	Matrix
E_1, psi	$4(10^7)$	$5(10^5)$
E_2, psi	$2.25(10^7)$	
E_3, psi	$2.25(10^7)$	
ν_{12}	0.2	0.35
ν_{23}	0.25	
ν_{13}	0.25	
G, psi	$1.5(10^7)$	$1.85(10^5)$
σ_y, psi		$2(10^4)$

4.1 Experimental Tests for Required Input

The twelve material curves required as input for MAT213 are obtained through coupon testing and are used as a part of the verification and validation tests described later.

Determination of Additional Input Parameters

The flow rule coefficients are calculated using (a) the flow law from Eqn. (2.19), and (b) the Poisson's ratio of the plastic strains to derive a set of functions relating the flow rule coefficients to the plastic Poisson's ratios. A general form of these equations was rewritten in terms of the plastic Poisson's ratios and H_{11} in Eqn. (2.40). However, this requires a known value of H_{11}. Since the T800/F3900 composite is unidirectional and transversely isotropic in the 2 and 3-directions, a simplified procedure described in Chapter 2 can be applied. The parameters H_{11}, H_{12} and H_{13} are assumed to be zero, from

$$\dot{\varepsilon}_{11}^{p} = \frac{\dot{\lambda}}{2h}\left(2H_{11}\sigma_{11} + 2H_{12}\sigma_{22} + 2H_{13}\sigma_{33}\right) = 0 \quad \Rightarrow \quad H_{11} = H_{12} = H_{13} = 0$$

and Eqn. (2.32) holds true so H_{22} must be equal to 1. The flow law coefficient, H_{33}, can be assumed to be one as well, due to the assumption of transverse isotopy. The remaining value, H_{23}, can be determined using Eqn. (2.33), and is computed as -0.3792. It should be noted that the flow law coefficients are assumed to be constant, which implies a constant value of the plastic Poisson's ratio, v_{23}^{p} and is determined as an average value from unidirectional transverse (2-direction) tension test data.

The final three flow law coefficients H_{44}, H_{55} and H_{66}, are determined using the same fit technique as in the simplified case, discussed in Chapter 2. However, each shear curve must be fit with the 2-direction test acting as the baseline. Using the same method as described with Eqn. (2.41), the objective function for the problem can be rewritten in terms of the 2-direction baseline as

$$f(\mathrm{H}_{ll}) = \sum_{k=1}^{n}\left[\left(\hat{\sigma}_{22}\right)_k - \left(\hat{\sigma}_{ij}\right)_k\right]^2 \tag{4.1}$$

Results from this exercise in terms of computing the optimal flow-rule coefficients (solution to Eqn. (4.1)) are shown in Fig. 13 and Fig. 14. These plots show the results for the minimized difference between the shear and base curve in the effective stress vs. effective plastic strain space, Eqn. (4.1). However, the two curves do not exactly match, as the effect of the flow rule coefficient values do not fundamentally change the shape of the shear curves.
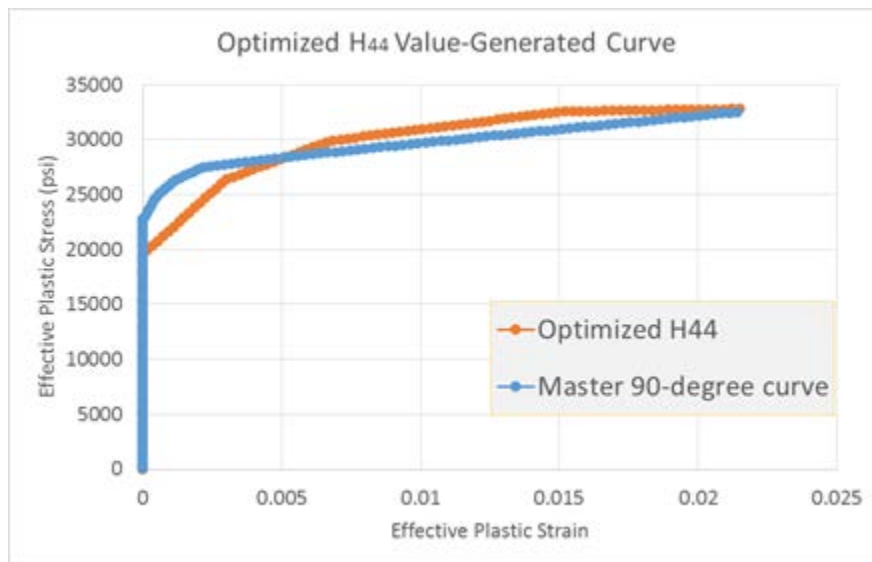
Fig. 13. Comparison of Master Curve with Optimized H_{44} (and H_{66}) Value
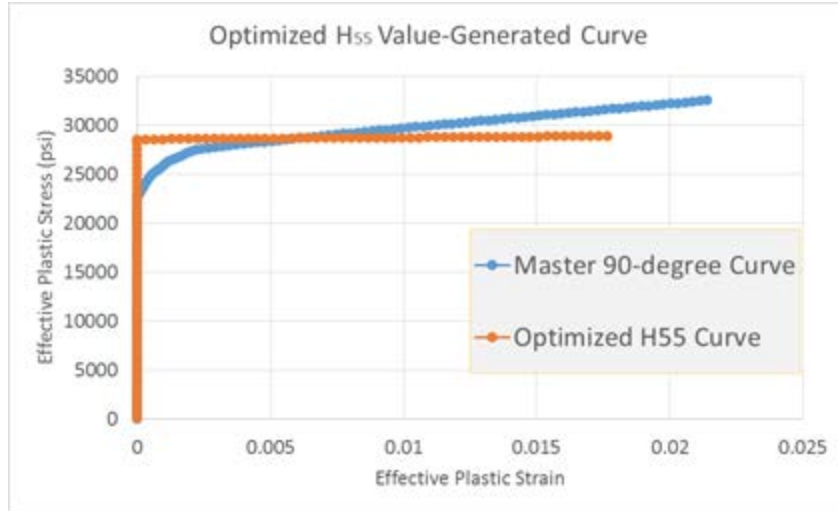
Fig. 14. Comparison of Master Curve with Optimized H_{55} Value

A summary of the all the flow law coefficient values is shown in Table 8 below.

Table 8. Flow Law Coefficients for T800-F3900 Composite

Coefficient	Value
H_{11}	0.0
H_{22}	1.0
H_{33}	1.0
H_{12}	0.0
H_{23}	-0.3792
H_{13}	0.0
H_{44}	7.7
H_{55}	6.1
H_{66}	7.7

4.2 Constitutive Model Verification

The experimental and computed supplemental data described earlier is used for verification tests. Since the experiments were performed under quasi-static, room

82

temperature (QS-RT) conditions only, fabricated temperature and strain rate dependent

data were created based on extrapolations from the QS-RT data. The fabricated data (at

increased temperature, 122, and strain rate, 0.1) were created for two strain rates (0.001

(QS) and 0.1 1/s) and two temperatures (21°C/70°F (RT) and 50°C/122°F) by scaling the

original stresses by 1.1 for the increased strain rate and 0.8 for the increased temperature.

Additionally, the verification simulation results in this sections are shown for a 64-

element model, with a representative convergence analysis shown for the 1-2 plane off-

axis case shown in Fig. 15.
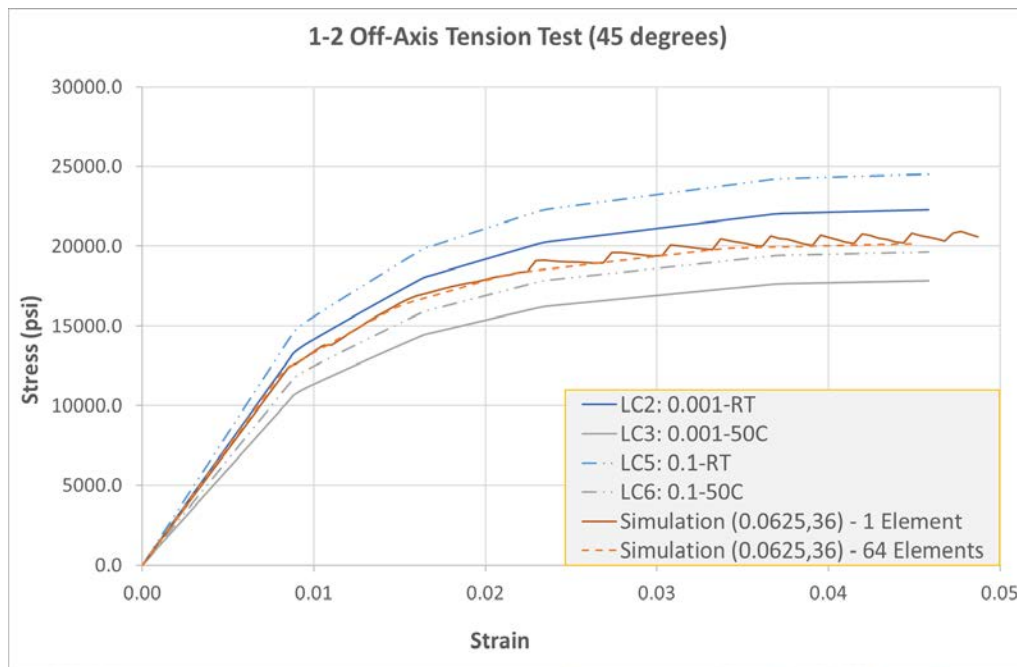
Fig. 15. Representative Convergence Study for Verification Tests

Schematics for the tension and compression tests are shown in Fig. 16 and Fig. 17,

respectively.

(a)   (b)
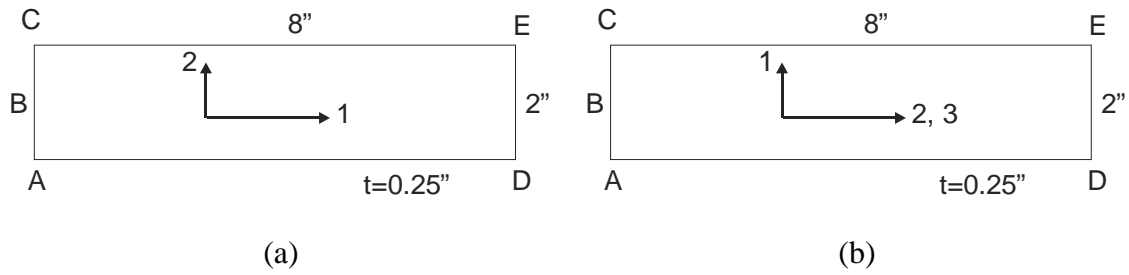
Fig. 16. Schematics for Tension Test Cases (a) 1-Direction (b) 2 and 3-Directions

(a)   (b)
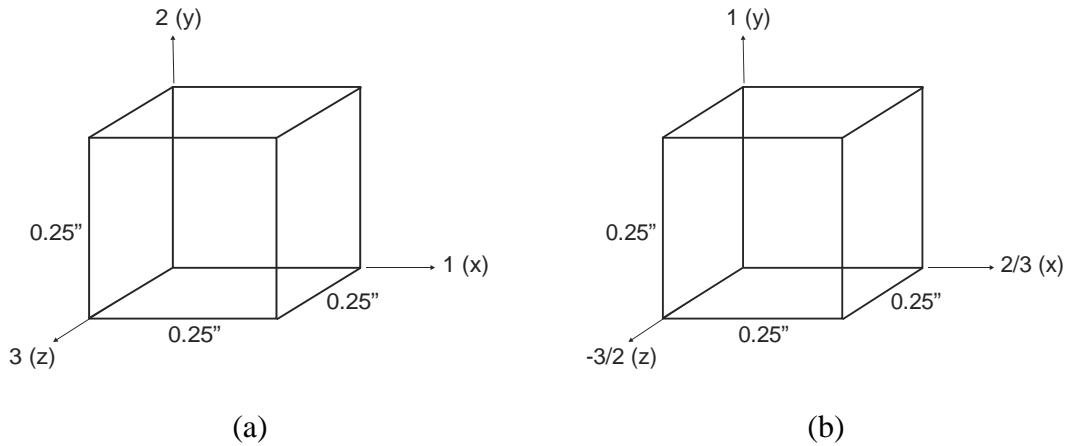
Fig. 17. Schematics for Compression Test Cases (a) 1-Direction (b) 2 and 3-Directions

The simulations for the tension and compression tests in all directions were executed using different mesh sizes ranging from 1 element to 64 elements. 64-element meshes for the tension and compression test cases are shown in Fig. 18 and Fig. 19, respectively.
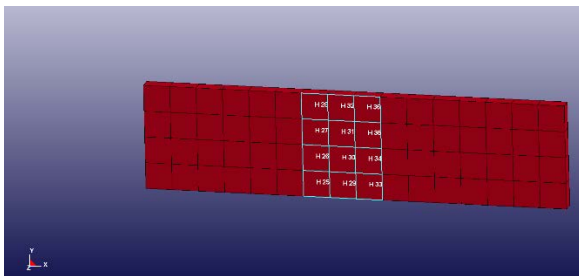
Fig. 18. 64-Element Mesh for Tension Test Cases
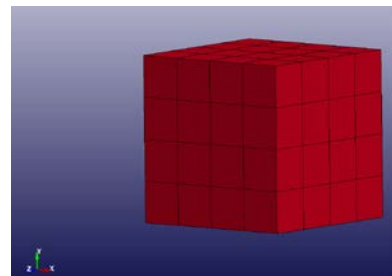
Fig. 19. 64-Element Mesh for Compression Test Cases

For both tension and compression tests, nodes on face ABC were constrained in the x-direction and the center node was also constrained in the y-direction. A 0.5 in/s displacement in the x-direction was applied to all the nodes on the right face, E-D. For the compression tests, care was taken to ensure that the model yielded but did not buckle. The simulated and experimental stress-strain curves for the tension and compression tests are shown in Fig. 20 and Fig. 21, with the simulation matching the input QS-RT data and correct interpolation for the temperature and strain rate dependent input.
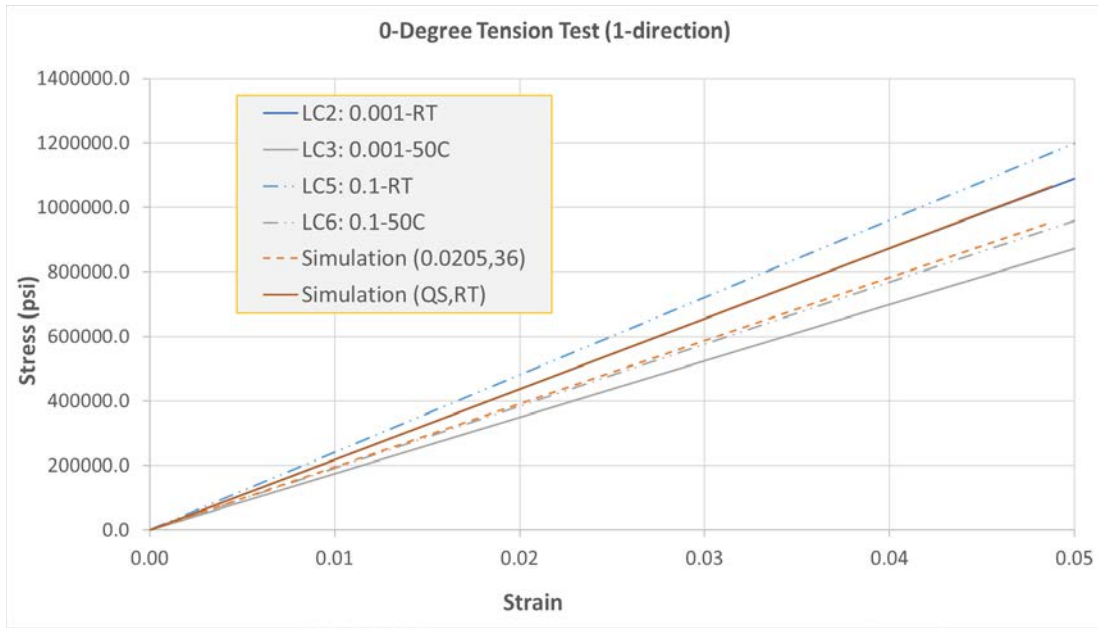
(a)
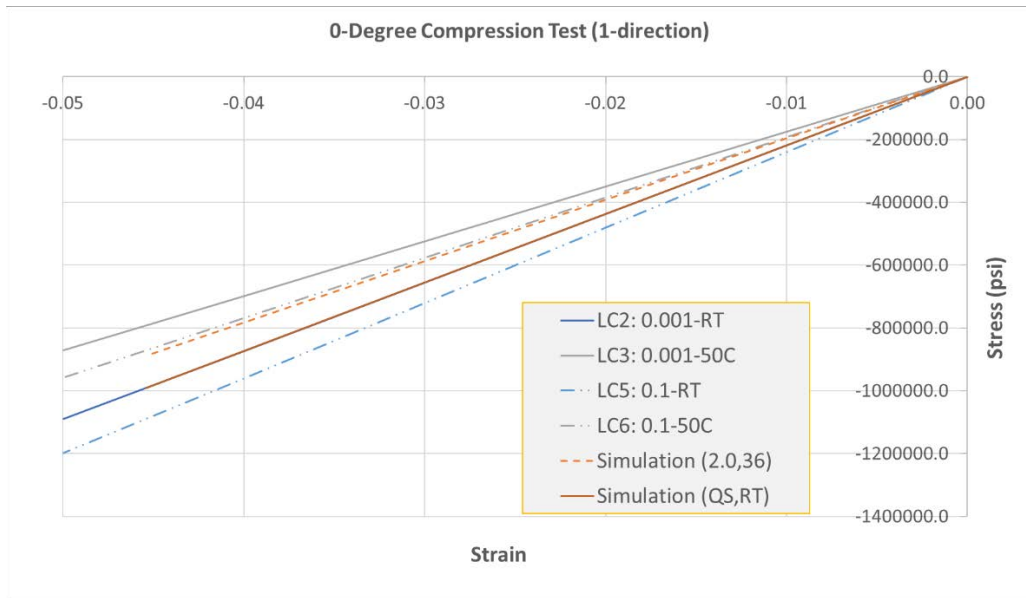
(b)

Fig. 20. Simulated and Experimental Stress-Strain Curves for 1-Direction (a) Tension and

(b) Compression

86
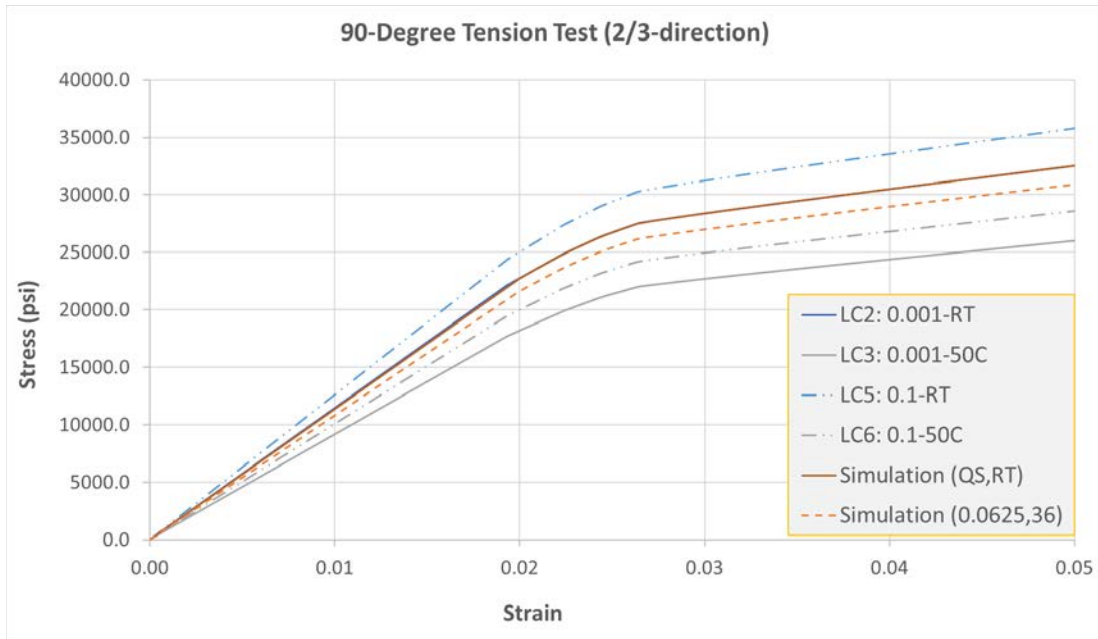
(a)
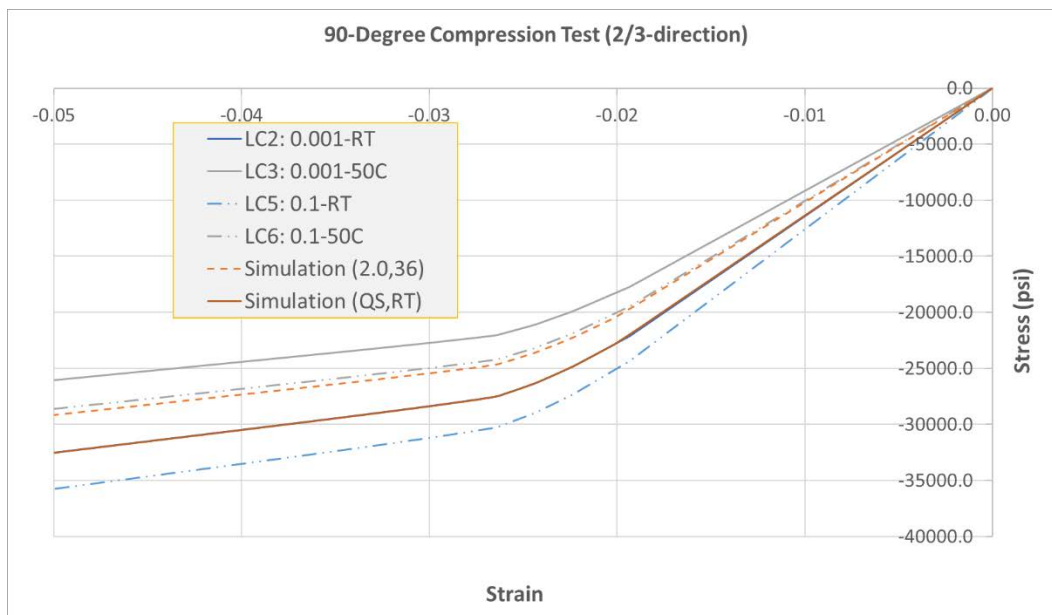
(b)

Fig. 21. Simulated and Experimental Stress-Strain Curves for 2/3-Eirections (a) Tension

and (b) Compression

A schematic for the pure shear test is shown in Fig. 22. Nodes on the bottom surface are restrained in the x and y-directions while nodes on the top surface are restrained in the y-direction. A displacement controlled loading of 0.5 in/s in the x-direction is applied to all the nodes on the top surface.
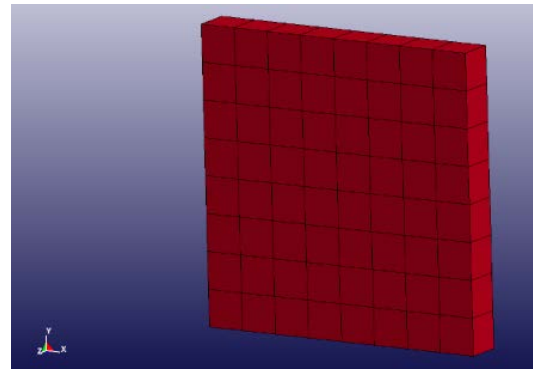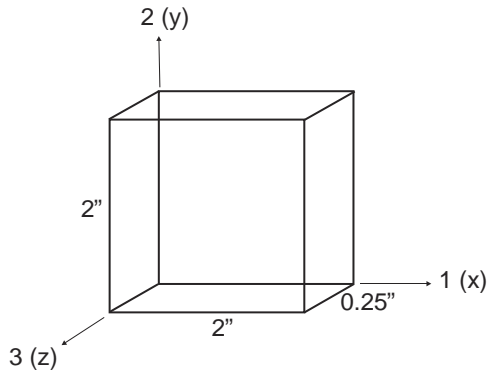
Fig. 22. Schematic for Pure Shear Test in 1-2/3-1 Plane

Fig. 23. 64-Element Mesh for Pure Shear Test Cases

The 64-element mesh is shown in Fig. 23. The simulated and experimental stress-strain curves in the 1-2/3-1 plane is shown in Fig. 24 and in the 2-3 plane in Fig. 25. All four simulations show good correlation with the input data.
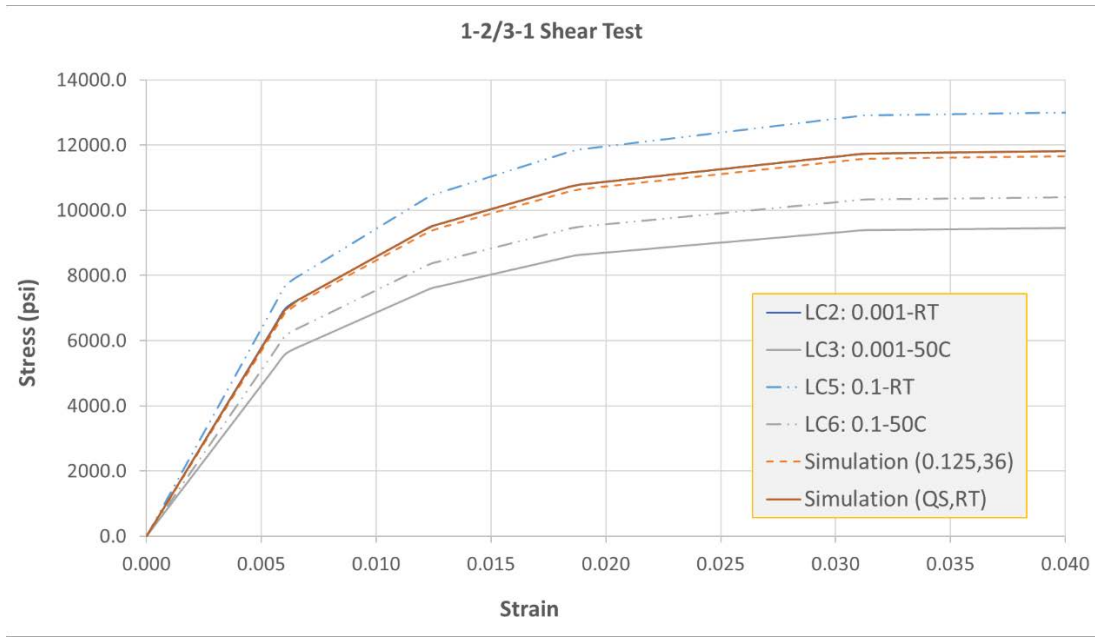
Fig. 24. Simulated and Experimental Stress-Strain Curves for Pure Shear in the 1-2/3-1

Plane
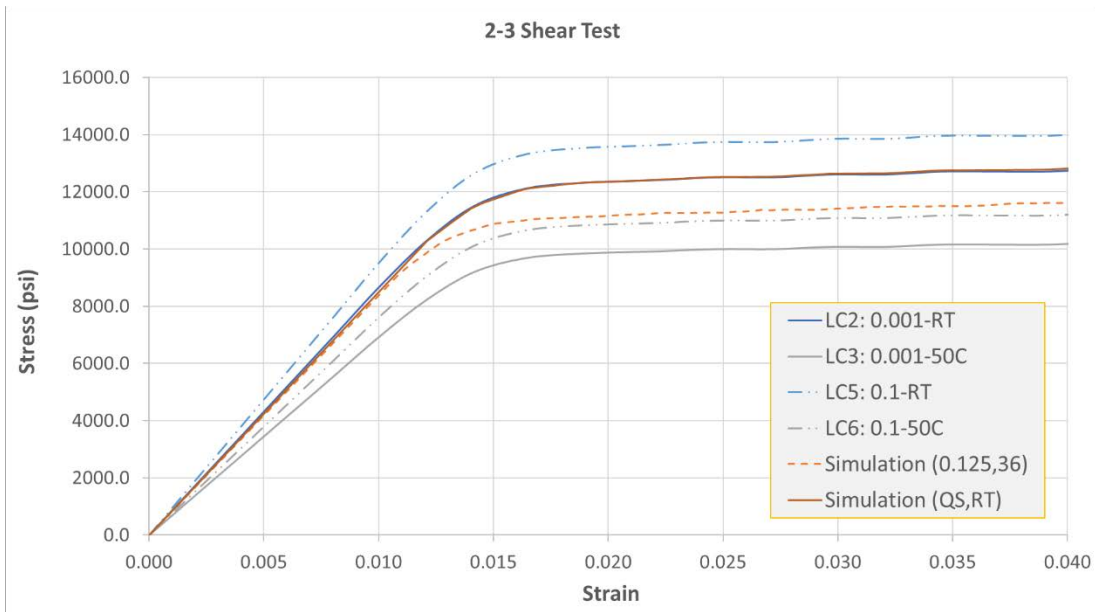
Fig. 25. Simulated and Experimental Stress-Strain Curves for Pure Shear in the 2-3

Plane

The (tension) off-axis test model is shown in Fig. 26. Nodes on face ABC were constrained in the x-direction and the center node was also constrained in the y-direction. The simulated and experimental stress-strain curves are compared for the 1-2/3-1 and 2-3 cases in Fig. 27 and Fig. 28, showing very little differences in the results.
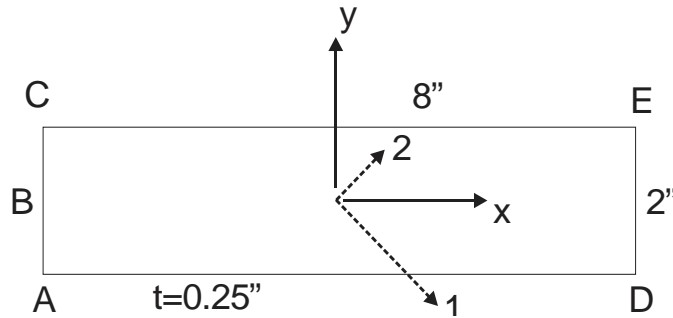
Fig. 26. Schematic for 45° Off-Axis Test in 1-2/3-1 Plane
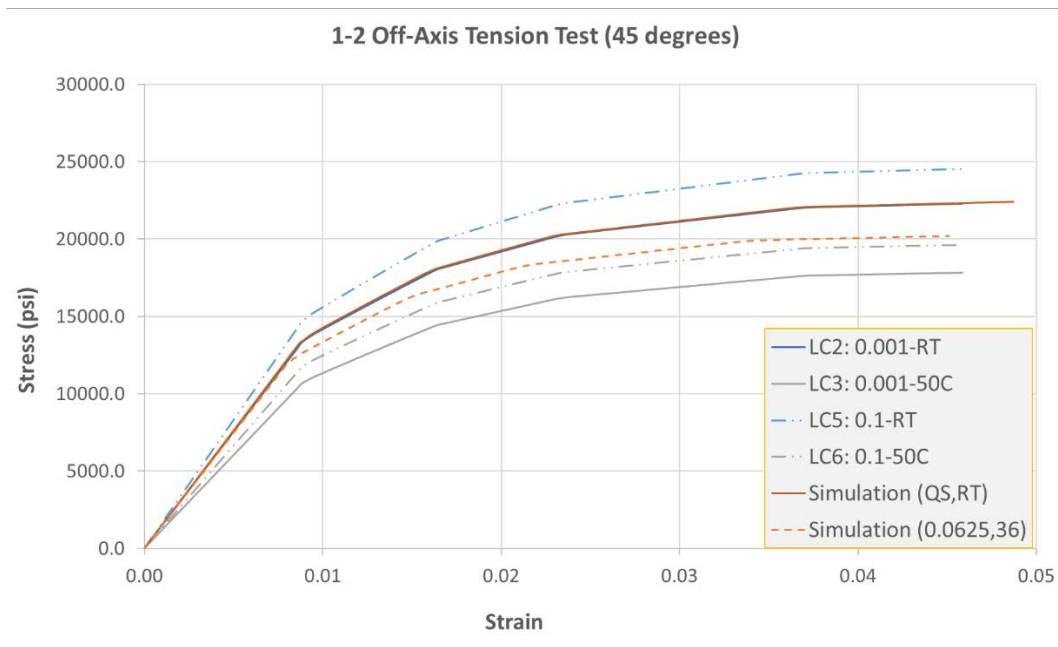
Fig. 27. Simulated and Experimental Stress-Strain Curves for 45° Off-Axis Test in 1-2/3-1 Plane
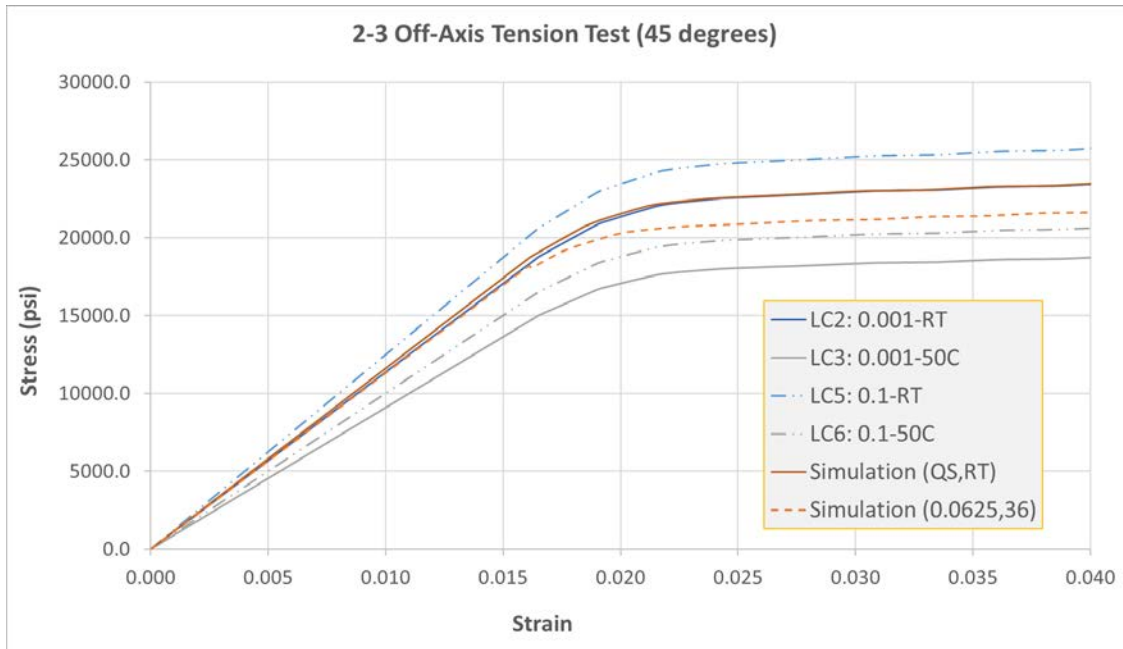
Fig. 28. Simulated and Experimental Stress-Strain Curves for 45° Off-Axis Test in 2-3

Plane

A simple loading-unloading-reloading test case was simulated using the 2-direction verification model, without damage, to verify the elastic unload/reload capabilities of the model, results shown in Fig. 29. The model shows the proper elastic unloading and reloading, matching the initial elastic modulus and plastic deformation.
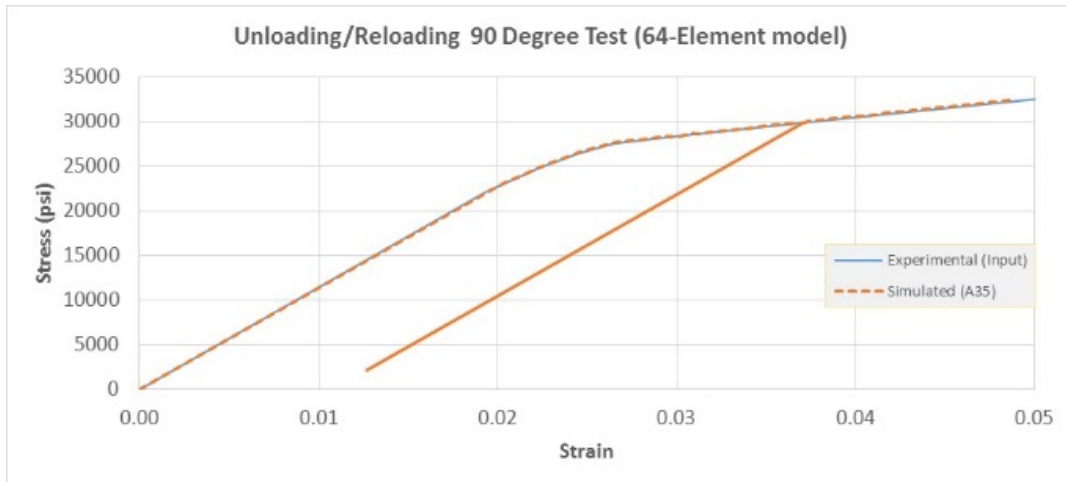
Fig. 29. Simulated and Experimental Stress-Strain Curves for Unloading/Reloading in the

2-Direction (No Damage)

Verification of the damage model was performed on the unidirectional 2-direction

tension test, using a fabricated psuedo damage-strain curve, d_{22}^{22} , that would typically be

obtained through damage characterization tests described in Chapter 3, shown in Fig. 30.
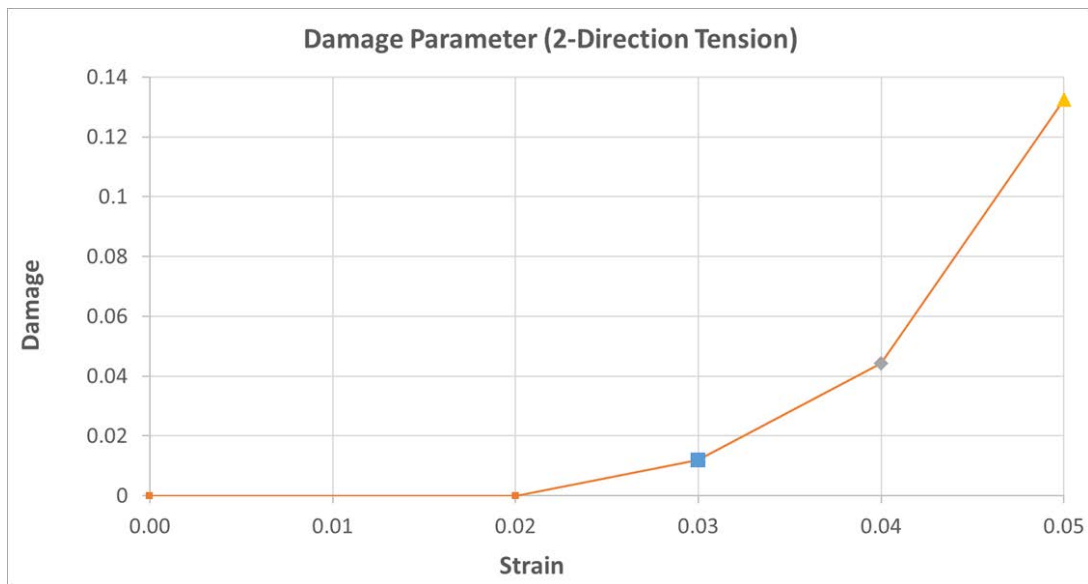
Fig. 30. Damage Versus Strain Curve with Three Unloading/Reloading Steps, Used in

Damage Verification Test

To test the damage model for this case, the same 2-direction tension verification simulation was used, but with the damage defined above (equivalent to a 1-D damage test case). Three unloading/reloading steps were created in the simulation corresponding to the total strain points of the damage curve in Fig. 30. The sumulation stress-strain curve was compared to the expected input stress-strain curve, shown in Fig. 31, with damaged unloading/reloading moduli corresponding to the degree of damage defined as input (Fig. 30). The simulation matches the expected stress-strain response, with the deformation response the same as the input 2-direction stress-strain curve, and is able to correctly model the reduced/damaged modulus effect.
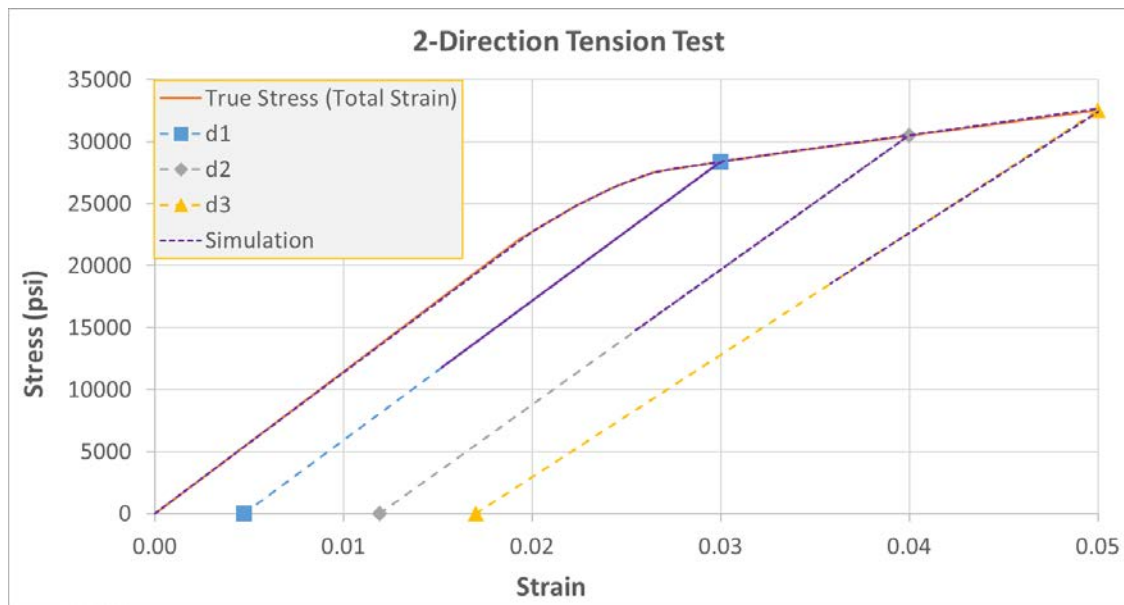
Fig. 31. Damage Verification Stress Versus Strain Plot with Three Unloading/Reloading Cycles

4.3 Constitutive Model Validation

The input data utilized for the verification and validation studies is a combination of actual experimental data obtained by (Raju and Acosta 2010) and numerical simulations. The numerical simulations were conducted to obtain required stress-strain curves which were not available from the provided experimental data. The specific experimental data that were available included tensile and compressive stress-strain curves in the longitudinal 1-direction and in-plane shear stress-strain curves in the 1-2 plane. To obtain the stress-strain curves required for input to the model that were not available from actual experimental data, an inverse analysis process was used. The unidirectional two-phase composite architecture was assumed based on publicly available data. A fiber volume fraction of 0.54 was assumed based on data presented in (Bogert, Satyanarayana and Chunchu 2006). The fiber was assumed to be transversely isotropic and linear elastic (Table 9), with properties determined using procedures described in (R. Goldberg, K. Carney and P. DuBois, et al. 2016). The matrix was assumed to be isotropic and elasto-plastic with a small strain-hardening component (Fig. 32). For convenience, the small amount of strain hardening was applied to the matrix for numerical stability purposes. The elastic properties of the matrix were determined using procedures described in (R. Goldberg, K. Carney and P. DuBois, et al. 2016). To determine the matrix yield stress, a micromechanics analyses of the pure shear test (1-2 plane) was conducted using the NASA Glenn developed MAC/GMC code based on the Generalized Method of Cells (Bednarcyk and Arnold 2002). The elasto-plastic properties of the matrix were adjusted so that the MAC/GMC results were reasonably close to the experimental results (Fig. 33). The correlation analyses were conducted for the cases of

94

(a) pure shear of a unidirectional composite, and (b) tensile loading of [+/-30]s and [+/-45]s laminates. The matrix yield stress was chosen such that the best possible match was obtained between the analytical results and the experimental curves for each of these cases. It should be noted that such an inverse analysis is not trivial. For example, in this case, if the material values were adjusted to match the shear curves, then the off-axis test curves could not be matched closely, and vice-versa. We suspect that this problem results from using a J2 plasticity model for the polymer that exhibits a different plasticity behavior due to hydrostatic stress effects.

Table 9. Fiber and Matrix Properties for T800S/3900 Composite

Engineering Constant	Fiber	Matrix
E_1 (psi)	$4(10^7)$	$5(10^5)$
E_2, E_3 (psi)	$2.25(10^7)$	$5(10^5)$
ν_{12}, ν_{13}	0.2	0.35
ν_{23}	0.25	0.35
G_1 (psi)	$1.5(10^7)$	$1.85(10^5)$
G_2, G_3 (psi)	$1.5(10^7)$	$1.85(10^5)$
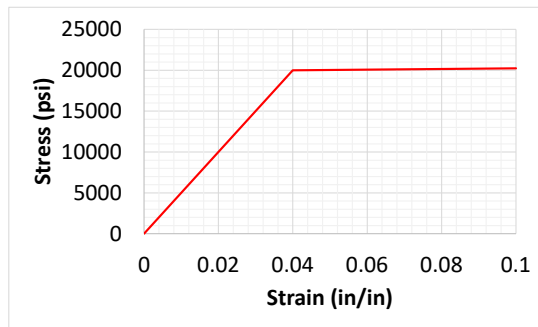
Fig. 32. Assumed Elasto-Plastic Behavior of the Matrix
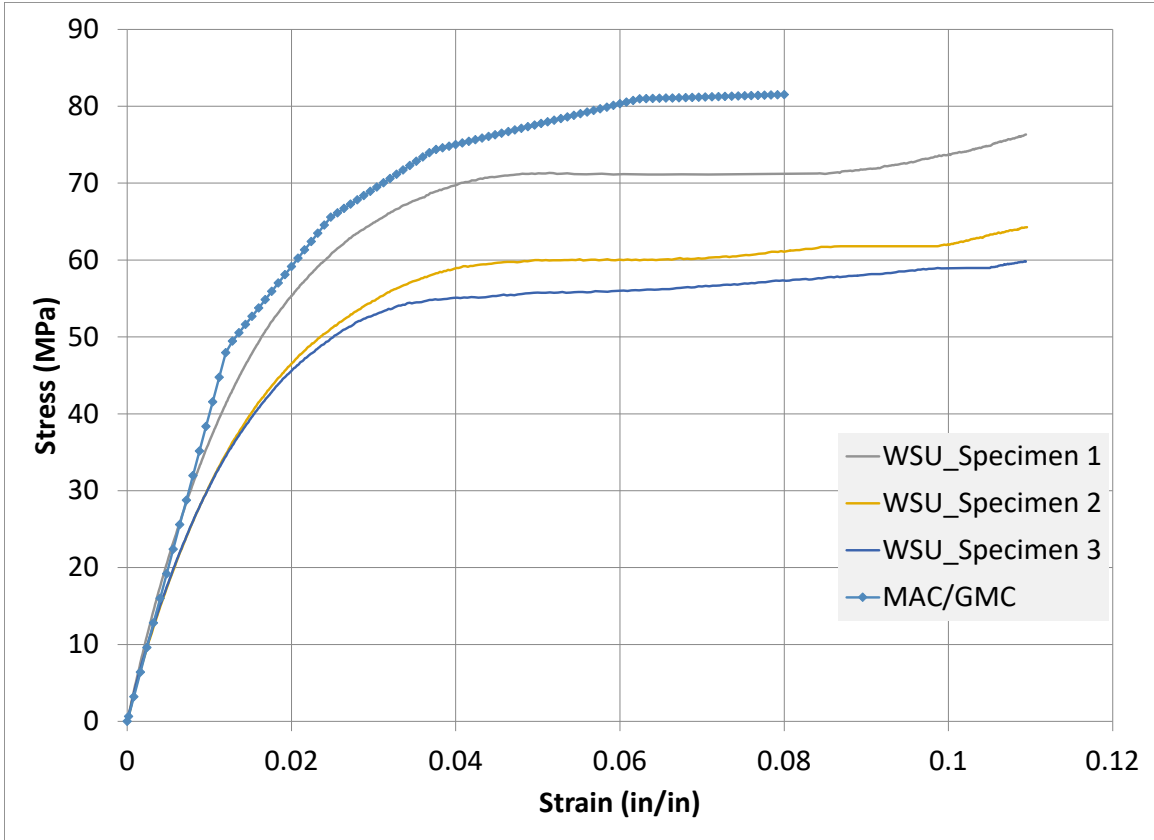
Fig. 33. Shear Stress-Strain Curves (1-2 Plane) Showing Three Experimental Curves (Raju and Acosta 2010) and the Curve Generated by Using MAC/GMC Program

Once the fiber and the matrix properties were obtained in this manner, additional micromechanics analyses were conducted using MAC/GMC code and implicit finite element analyses (Virtual Testing Software System or VTSS) which will be described in detail in a future paper, to obtain the remainder of the required input curves for the MAT213 simulations. Examples of these curves are shown in Fig. 34 and Fig. 35.
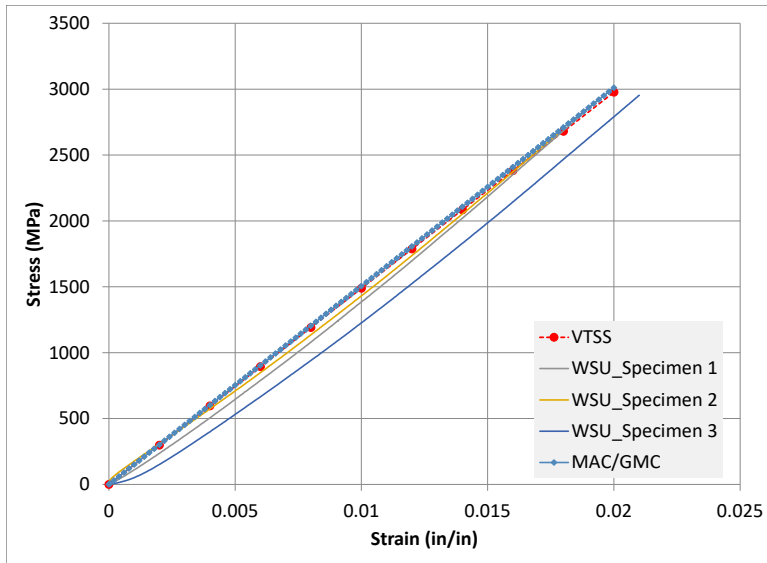
Fig. 34. 1-Direction Tension Stress-Strain Curves Showing Three Experimental Curves

(Raju and Acosta 2010) and the Curves Generated by Using MAC/GMC Program and
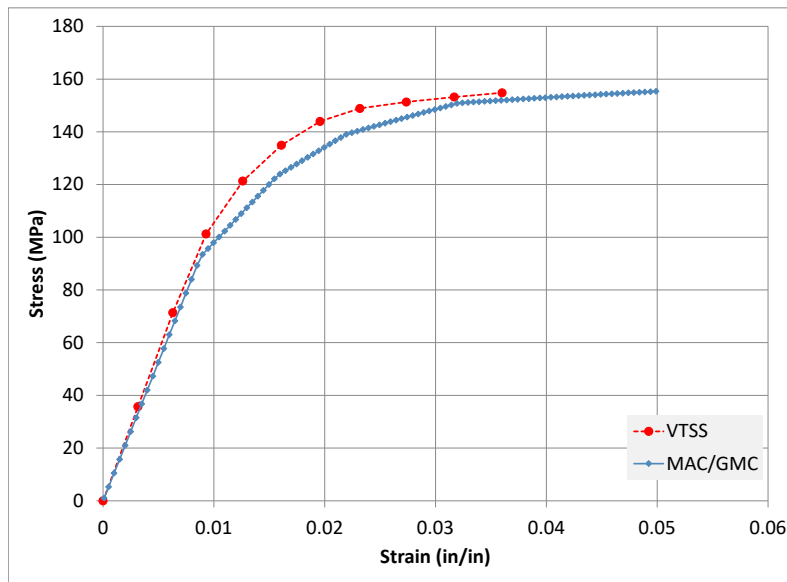
VTSS Program

Fig. 35. 1-2 Plane 45^0 Off-Axis Tension Stress-Strain Curves Showing the Curves

Generated by Using MAC/GMC Program and VTSS Programs (Experimental Curve is

Not Available)

Based on the actual and correlated input stress-strain curves, a series of

verification studies were conducted to demonstrate that the input data (12 input curves)

could be replicated using the material model, outlined above. These verification studies

are also described in detail in (Hoffarth, et al. 2014). Table 10 lists the computed elastic

properties of the composite.

Table 10. Properties of T800S/3900 Composite

Engineering Constant	Value
E_1 (psi)	$2.183(10^7)$
E_2, E_3 (psi)	$1.145(10^6)$
ν_{12}, $\nu_{21,}$ $\nu_{13,}$ ν_{31}	0.264
$\nu_{23,}$ ν_{32}	0.3792
G_{12}, G_{21} (psi)	$5.796(10^5)$
$G_{23,}$ G_{32} (psi)	$3.243(10^5)$
$G_{31,}$ G_{13} (psi)	$5.796(10^5)$

4.4 Validation Test Model: Laminated Coupon Tests

A set of validation tests were performed using data obtained for (+/- 15°)$_{2S}$, (+/-

30°)$_{2S}$ and (+/- 45°)$_{2S}$ laminates of the T800/F3900 composite described above. A series

of finite element models with 1, 4, 16 and 64 elements per ply with full integration solid

elements were created. The layups were created based on the experimental tests

performed in (Raju and Acosta 2010). The thickness of each ply was set to 0.1905

millimeters with a total lay-up thickness of 1.524 millimeters, with the specimen

dimensions set to match those of the experimental tests (50.8 mm x 12.7 mm). The

validation tests were executed using both the developed finite element constitutive model

and MAC/GMC and the results are compared against experimentally obtained data.

Comparing the finite element results to results obtained using the analytical MAC/GMC

micromechanics method assisted in determining whether the finite element based

material model could produce results to an appropriate level of precision based on a given

set of input data. The comparisons of the computed results to experimentally obtained

values allowed for a determination of the accuracy of both the material property

correlation procedure and the material model. A schematic of the ply geometry for the

(+/- 15°)$_{2S}$, (+/- 30°)$_{2S}$ and (+/- 45°)$_{2S}$ validation analyses is shown in Fig. 36. The

boundary conditions were chosen to mimic the experimental setup as closely as possible.

The value of α depends on the individual ply of the given layup, i.e. +/-15°, +/-30° or +/-

45°.
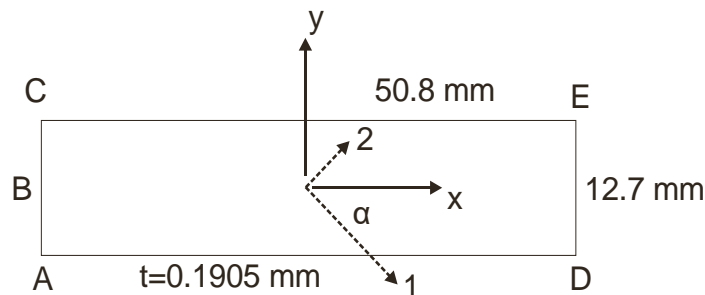
Fig. 36. Schematic of Individual Ply for Validation Analyses

Nodes on the edge ABC were fixed in the x-direction, with additional fixity in the

y/z-directions also enforced at the (center) node at B. Displacement-controlled

simulation was carried out - nodes on edge ED were moved in the positive x-direction at

a rate of 12.7 mm/s, and these nodes were restrained in the y and z-directions. The finite

element model is shown in Fig. 37 and is used with the implementation of the material

model in LS-DYNA.

<center>(a)　　　　　　　　　　　　　　　　　(b)</center>
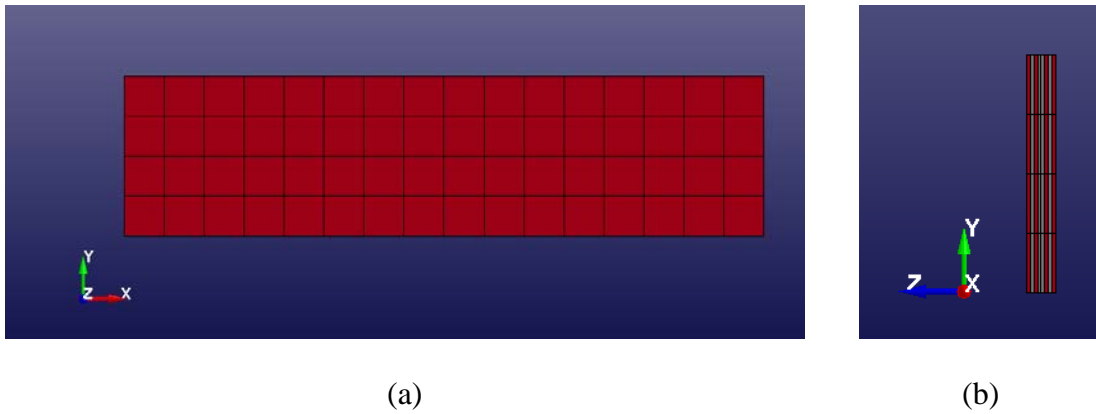
Fig. 37. Validation Model for the 64-Element Per Ply Test Case (a) Plan View and (b)

<center>Side View</center>

While the 1, 4, 16 and 64 finite element models were used to study the

convergence properties of the problem, only the results from the 64-element models are

discussed next, as this mesh density was found to produce sufficiently converged results.

The results for the (+/- 15°)$_{2s}$, (+/- 30°)$_{2s}$ and (+/- 45°)$_{2s}$ validation analyses are shown in

Fig. 38, Fig. 39 and Fig. 40. The finite element simulation results using MAT213

(labeled "Simulation") and the MAC/GMC results (labeled "MAC/GMC") are compared

against experimental data (labeled "WSU").
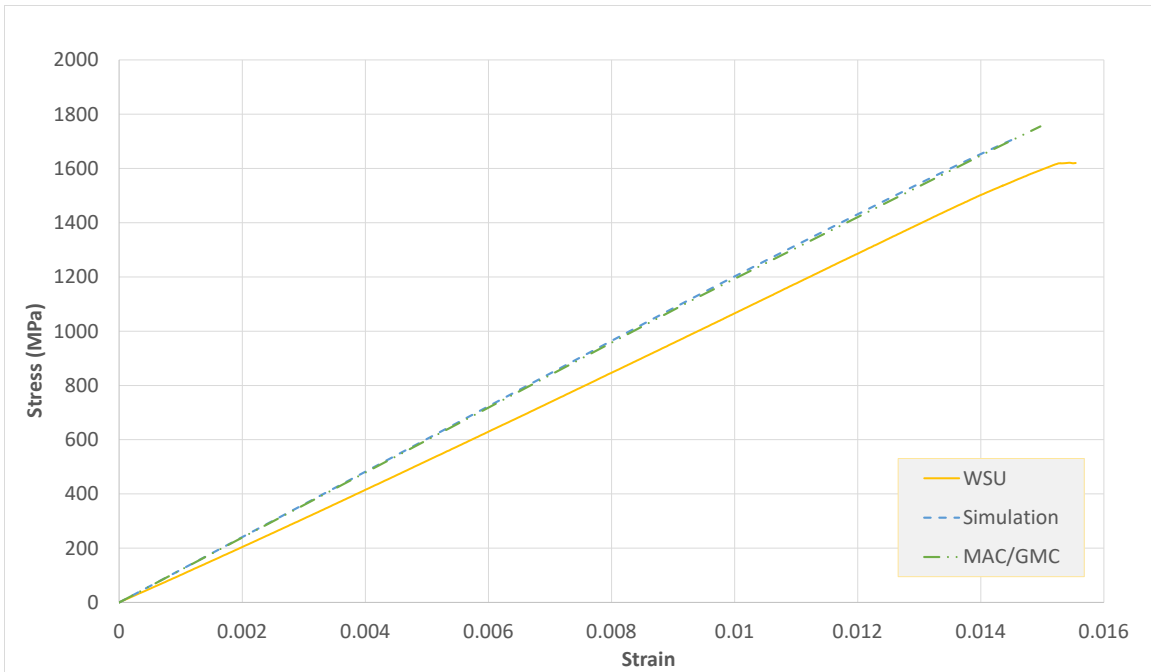
Fig. 38. Comparison of Experimental (Raju and Acosta 2010) and Numerical Solutions

for (+/- 15°)$_{2S}$ Validation Test
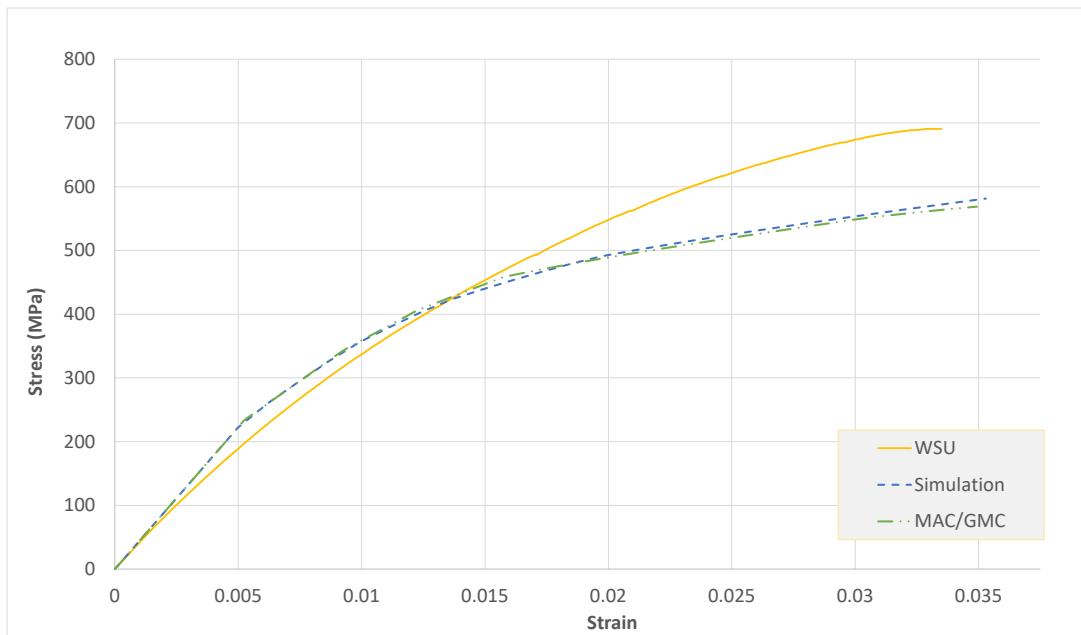
Fig. 39. Comparison of Experimental (Raju and Acosta 2010) and Numerical Solutions

for (+/- 30°)$_{2S}$ Validation Test
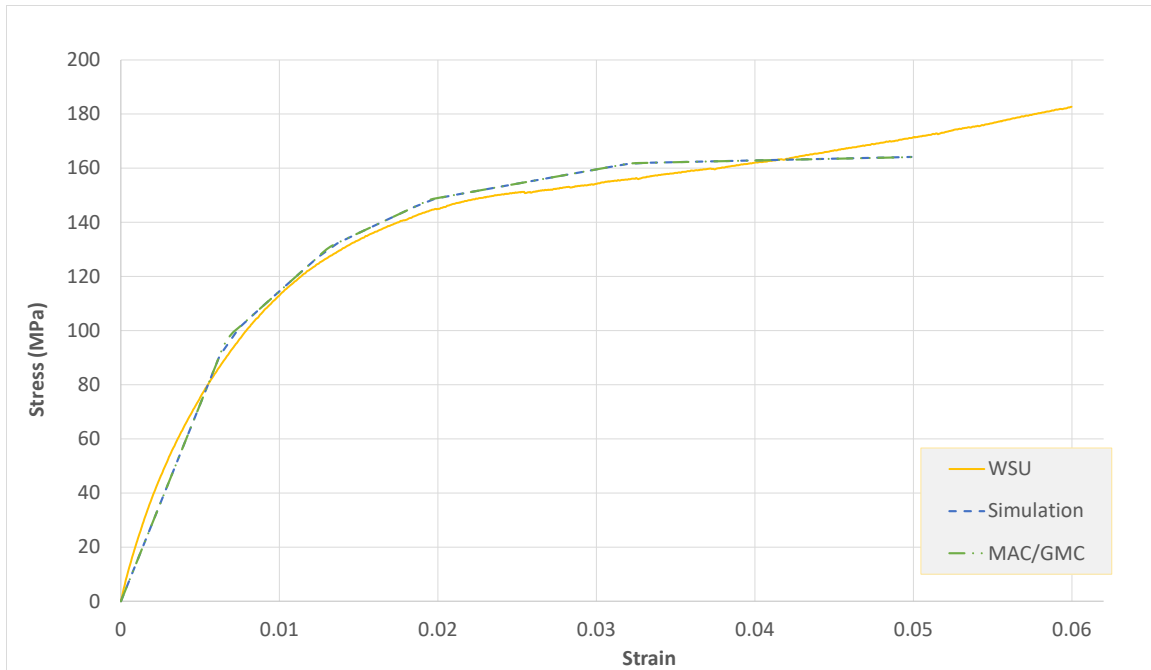
Fig. 40. Comparison of Experimental (Raju and Acosta 2010) and Numerical Solutions

for (+/- 45°)$_{2S}$ Validation Test

The results show several important facts. Since the implementation of the constitutive theory into a finite element program was able to exactly reproduce the MAC/GMC stress-strain curves (from which the input curves were generated), the results show that given a certain set of input data the developed material model can appropriately simulate the deformation response of composites given laminate layups more complicated than those used in the input curves. The accuracy of the simulations is based on the accuracy of the input curves. The differences between the experimental results and the simulation are probably due to several reasons. First, in Fig. 38, Fig. 39 and Fig. 40, only one experimental curve is shown, and thus any potential scatter in the experimental data is not captured. The computed results might be close to or within the statistical scatter in the experimental data. Second, in the off-axis tests there are stress

102

interactions between various modes (such as between normal and shear stresses) that might not be properly accounted for in the simulations. There might also be (coupled and uncoupled) damage mechanisms occurring in the actual composites which are not currently accounted for in the present deformation model. Finally, since the full suite of experimental data (12 stress-strain curves) was not available to generate the input stress-strain curves, the missing curves were approximated using an inverse analysis procedure with assumed data and simplifying assumptions. A simplified model was used in modeling the matrix in the micromechanics simulations – a nearly elastic-plastic model in which the tensile and compressive responses were assumed to be identical. It is likely that this simplifying assumption accounts for some of the errors in the +/-30° model and the lack of strain hardening at the end of the +/-45° model.

4.5 Validation Test Model: Low-Velocity Impact Structural Test

The second part of the validation tests involves a 12" x 12" x 0.122" T800/F3900 composite flat panel subjected to a low velocity impact. The physical test was performed by our project research colleagues at NASA Glen Research Center, with the schematics of the test shown in Fig. 41. The panel was fabricated with 16 plies with the fibers in the panel being aligned along the Y-direction (Fig. 42).

(a)

(b)

(c)

(d)

(e)
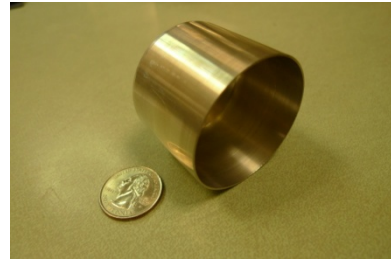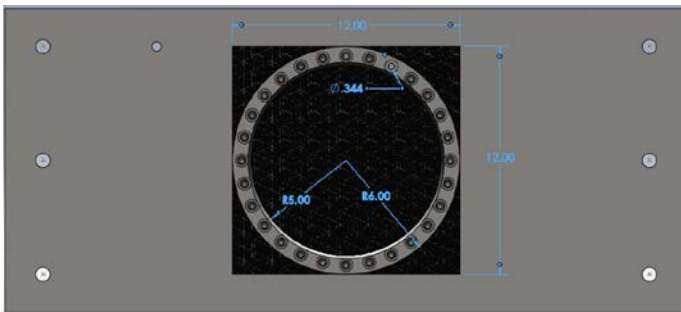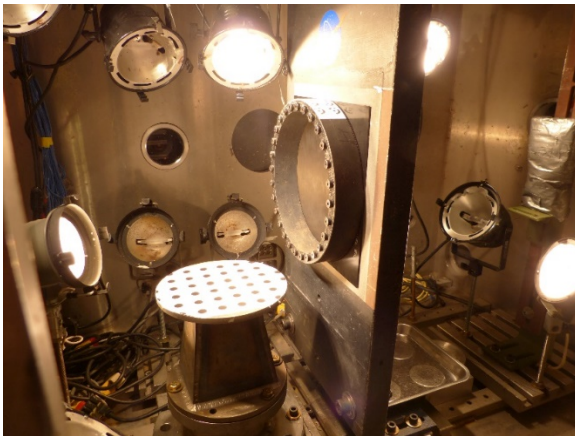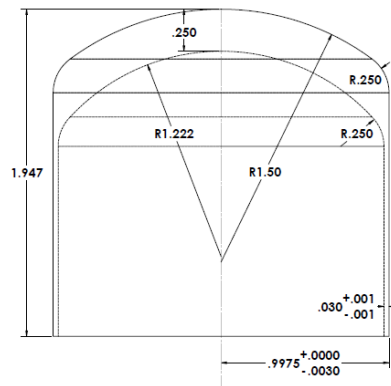
(f)

Fig. 41. Impact Structural Test (a) Small Impact Gun (b) 12" x 12" Panel with a 10"

Circular Clamping Pattern (c) Inside View of Test Chamber (d) 50 gm Hollow Al-2024

Projectile With Radiused Front Face (e) Another View of the Projectile (f) Engineering

Drawing of the Projectile (Units: Inches)

A 50.8 gm projectile (Fig. 41(d)-(f)) was fired at the panel at a velocity of 27.4

ft/s (projectile moves left to right in Fig. 41(c)) and impacted approximately 0.70 inches

below the center of the panel. The projectile did not impact the center due to its low

velocity and gravitational forces. Examination of the panel (LVG906) after impact

showed no visible damage or cracks. Experimental data was obtained using digital image

correlation (DIC) on the back side of the plate so as produce full-field displacements and

strains across the unsupported region. A finite element model of the test was created (Fig.

42) to replicate the test conditions.

(a)

(b)

(c)
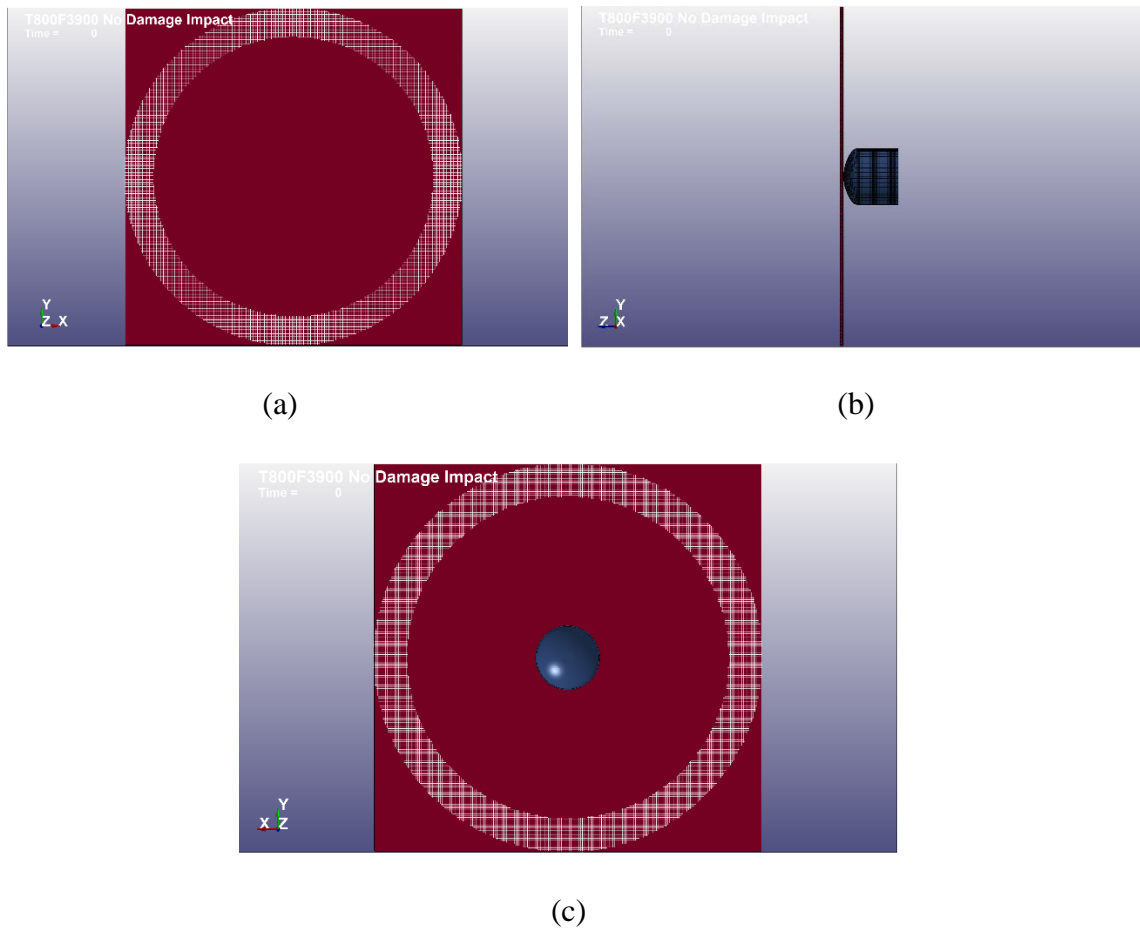
Fig. 42. LS-DYNA Finite Element Model (a) Back View, (b) Side View (c) Front View

The boundary conditions were applied to the plate in a way that mimicked the manner the plate was supported in the test frame. The bolted assembly shown in Fig. 41(c) was modeled by fixing the X,Y,Z translational displacements of the nodes in the gripping region of the panel. The composite plate was modeled with 288,000 8-noded hexahedral elements. A typical element is 0.05 x 0.05 x 0.0244 inches with 5 elements through the thickness of the panel. The aluminum impactor was modeled with 27,200 8-noded hexahedral elements. Two material models in LS-DYNA were used to model the composite plate in two separate finite element models so as to compare their performance - MAT22 (Table 11) and MAT213, current and new models, respectively. The aluminum impactor was modeled using MAT24 (Piecewise_Linear_Plasticity) with the material properties given in Table 12. Contact between the plate and the impactor was controlled using the LS-DYNA keyword *Contact_Eroding_Surface_To_Surface.

Table 11. MAT22 Material Parameters

Model Parameter	Value
Mass density (lb-s^2/in)	1.4507(10^{-4})
E_a (psi)	21.83(10^6)
E_b (psi)	1.145(10^6)
E_c (psi)	1.145(10^6)
V_{ba}	0.01385
V_{ba}	0.01385
V_{ba}	0.3792
G_{ab} (psi)	0.5796(10^6)
G_{bc} (psi)	0.3243(10^6)
G_{ca} (psi)	0.5796(10^6)
Shear Strength, SC (psi)	0.01376(10^6)
Longitudinal Tensile Strength, XT (psi)	0.412(10^6)
Transverse Tensile Strength, YT (psi)	0.00872(10^6)
Transverse Compressive Strength, YC (psi)	0.0243(10^6)
Alpha	0.0
Normal Tensile Strength, SN (psi)	0.00872(10^6)
Transverse Shear Strength, SYZ (psi)	0.015(10^6)
Transverse Shear Strength, SZX (psi)	0.01376(10^6)

Table 12. MAT24 Material Properties

Model Parameter	Value
Mass density (lb-s^2/in)	2.539(10^{-4})
E	10.30(10^6)
ν	0.334
Yield Stress, SIGY	42500
Tangent Modulus, ETAN	42000

Two comparison metrics were used - the maximum out-of-plane (Z-direction) displacement and the contour of the out-of-plane displacements, both on the back face of the plate. The contour plots are shown in Fig. 15 at the same time (0.0007s). The MAT213 results (Fig. 43(d)) are very similar to that of impact test (Fig. 43(b)), with a rounded shape that is slightly elongated in the fiber direction. The results from using MAT22 (Fig. 43(c)), shows a more elongated distribution of displacements in the fiber direction.

(a) (b)

(c) (d)
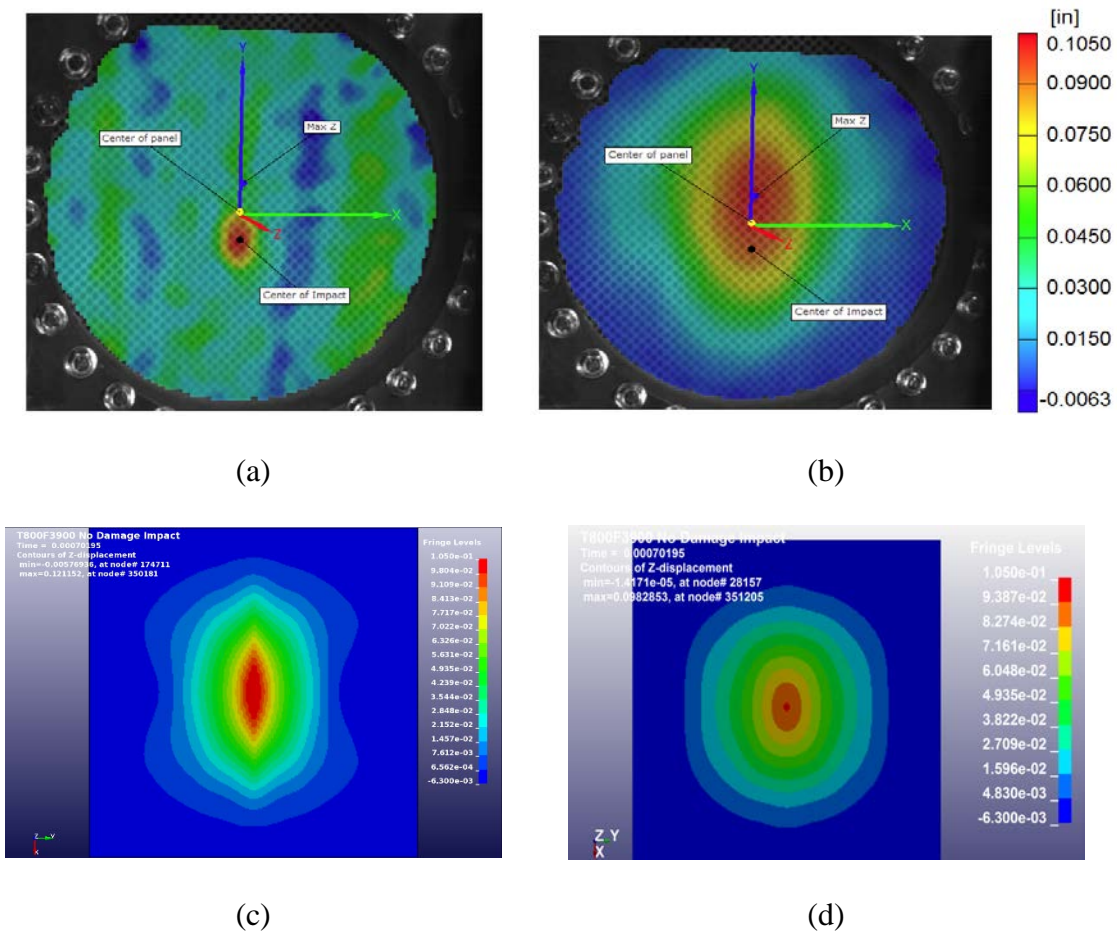
Fig. 43. (a) Plot of Experimental Data Showing Center of Panel, Point of Impact and Location of the Max. Z-Displacement; Out-of-Plane Displacement Contours at t=0.0007s for (b) Experiment (c) MAT22 Simulation and (d) MAT213 Simulation

A quantitative validation was performed by comparing the maximum out-of-plane (Z) displacement as a function of time. The out-of-plane displacement vs time results for the test and the simulations are plotted in Fig. 44. Two values from the test are used – one is the Z-displacement from the center of the plate and the other is the max. Z-displacement. As Fig. 43(a)-(b) show, in the experiment, the point of impact (POI) is approximately 0.7 inches below the center of the panel and the point of maximum Z-displacement is approximately 0.7 inches above the center of the panel. However, in the finite element models, the POI is taken as the center of the model.
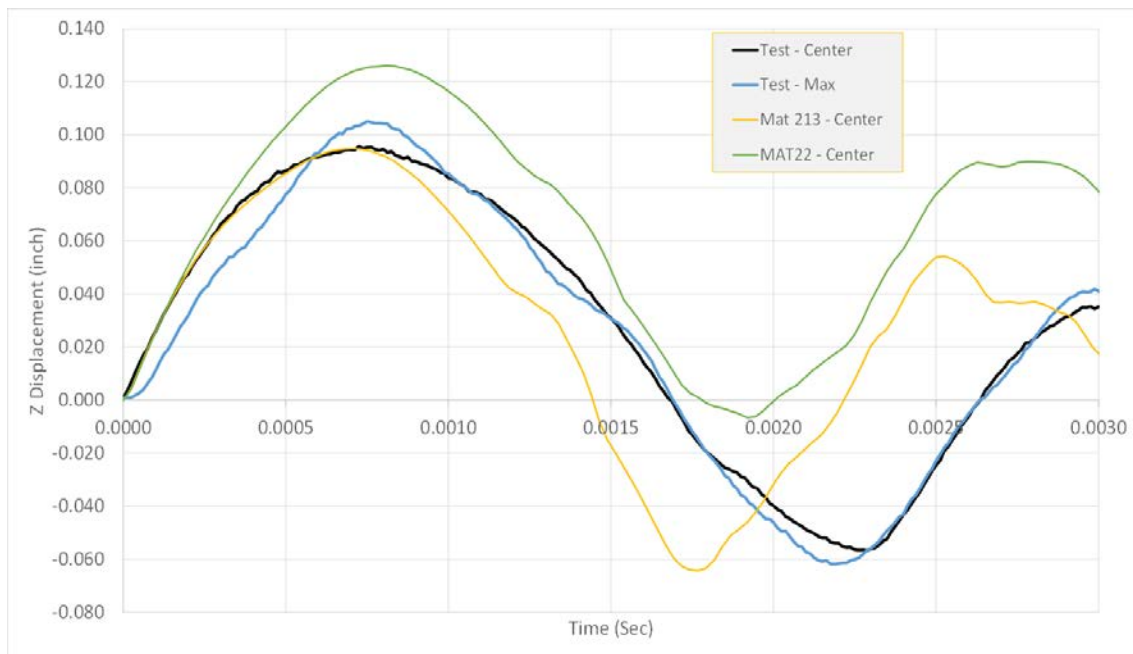
Fig. 44. Maximum Out-of-Plane (Z) Displacement Versus Time Plot for the Impact Test, and MAT22 and MAT213 Simulations. In Addition, the Z-Displacement at the Center of the Plate for the Impact Test is Also Shown.

In the finite element models, the maximum Z-displacement occurs at the center of the plate. The MAT213 results show a good agreement with the test results. The first (positive) peak displacement value is very close to the test value at the same time. The

first negative peak value is also close to the test value (marginally larger than test value) though it occurs at an earlier time. Similarly, the second positive peak value (that is about 40% of the first peak value) is larger than the test result and occurs at an earlier time. The MAT22 results show different trends. The first (positive) peak displacement value is higher by about 30% and occurs at about the same time as the test. The first negative peak value is substantially smaller than the test value and like MAT213, occurs at an earlier time. Similarly, the second positive peak value in the MAT22 curve is substantially larger than the test result and occurs at an earlier time. It should be noted that the MAT22 model is designed for use with composites exhibiting brittle failure ((Chang and Chang 1987a) (Chang and Chang 1987b)) and may require extensive tuning with its strength parameters for the T800/F3900 composite behavior.

There are a few differences between the impact test and finite element models that should be noted. First, the POI locations are not the same. Second, in the impact test, the projectile impact was not a direct hit, i.e. the roll, pitch and yaw angles were not all zero. However, zero roll, pitch and yaw angles were assumed in the finite element models. Third, while cracks were not visible on the tested panel, it is likely that the panel suffered permanent damage, albeit of small magnitudes near the center of the panel. The current implementation of MAT213 does not include a damage model, or rate sensitivity. Lastly, it is likely that the period differences in the test and FE models is partly due to no damping parameters being used in the FE models.

Chapter 5: Concluding Remarks

Composite materials are now beginning to provide uses hitherto reserved for metals, particularly in applications where impact resistance is critical. Such applications include structures such as airframes and engine containment systems, wraps for repair and rehabilitation, and ballistic/blast mitigation systems. While material models exist that can be used to simulate the response of a variety of materials in these demanding structural applications under impact conditions, the mature material models have focused on simulating the response of standard materials such as metals, elastomers and wood. Material models to simulate the nonlinear and/or impact response of composites have been developed, but the maturity and capabilities of these models are at a much lower level than those that have been developed for standard materials. General constitutive models designed for simulating the impact response of composite materials generally require three components – an elastic and inelastic deformation capability that relates deformations to strains and stresses, a damage capability that captures the stiffness degradation of the material, and a failure capability. Incorporating these three components - deformation, damage and failure (DDF), into a single unified model that is applicable for use for a wide variety of composite material systems and architectures is a significant challenge that this dissertation has addressed.

In this dissertation, a new orthotropic elasto-plastic computational constitutive material model has been developed to predict the response of composite materials during high velocity impact simulations. The model is driven by experimental stress-strain curve data stored as tabular input allowing for a very general material description. These stress-strain curves, in general, can be temperature and/or rate-dependent. The yield function is

based on the Tsai-Wu composite failure model, and a suitable nonassociated flow rule is defined. The current version has been implemented in a special version of LS-DYNA as MAT213 and supports the use of all solid finite elements. In addition to temperature and rate dependencies, the current model has the ability to handle user-specified damage parameters. For the damage model, a strain equivalent formulation is utilized to allow for the uncoupling of the deformation and damage analyses. In the damage model, a diagonal damage tensor is defined to account for the directionally dependent variation of damage. However, in composites it has been found that loading in one direction can lead to damage in multiple coordinate directions. To account for this phenomena, the terms in the damage matrix are semi-coupled such that the damage in a particular coordinate direction is a function of the stresses and plastic strains in all of the coordinate directions.

Several methods have been developed as a part of the implementation plan. First, tabulated stress-strain data is used to track the evolution of the yield stresses as a function of the effective plastic strain. This makes it possible to faithfully reproduce the experimental results without resorting to approximations. Second, procedures have been developed to adjust selected coefficients in the yield function in order to ensure a convex yield surface. Third, a numerical algorithm based on the radial return method has been developed to compute the evolution of the effective plastic strain, leading to the required computation of the stresses and the evolution of the yield stresses in each of the coordinate directions. The radial return methodology has been modified to account for the yield surface rotation that takes place due to the anisotropic plasticity law.

A rigorous verification and validation procedure has been followed to ensure that the computer implementation is correct as well as the theory can be validated against

112

experimental data. The validation tests have been used to verify both the deformation as well as the damage models using both real as well as synthetic data. The results from the validation tests are encouraging. The implemented constitutive model is able to reproduce the set of experimental stress-strain curves – the off-axis tension tests. The results at the tail end of the curves are likely to improve as the damage model is refined. In addition, a low-velocity impact modeling problem yields acceptable deformation and stress distributions.

Future work include the following – support for shell elements, addition of failure model to the implemented framework, validation of the entire DDF model using high-velocity impact data etc.

References

Allix, O. "A composite damage meso-model for impact problems." *J. Composites Science and Technology* 61 (2001): 2193-2205.

Barbero, E. J. *Finite element analysis of composite materials using Abaqus.* Boca Raton, FL: CRC Press, 2013.

Bednarcyk, B. A., and S. M. Arnold. *MAC/GMC 4.0 User's Manual - Keywords Manual.* Washington, D.C.: National Aeronautics and Space Administration, 2002.

Bergstrom, J. S. "Constitutive Modeling of Elastomers - Accuracy of Predictions and Numerical Efficiency." 2005. PolymerFEM. com.

Bogert, P. B., A. Satyanarayana, and P.B. Chunchu. "Comparison of Damage Path Predictions for Composite Laminates by Explicit and Standard Finite Element Analysis Tools." *47th AIAA/ASME/ASCE/AHS/ASC Structures, Structural Dynamics, and Materials Conference.* Washington D.C.: American Institute for Aeronautics and Astronautics, 2006.

Buyuk, M. *Development of a New Metal Material Model in LS-DYNA, Part 2: Development of a Tabulated Thermo-Viscoplastic Material Model with Regularized Failure for Dynamic Ductile Failure Prediction of Structures Under Impact Loading.* Final Report, Atlantic City: Federal Aviation Administration, 2014.

Chang, F. -K., and K. -Y. Chang. "A Progressive Damage Model for Laminated Composites Containing Stress Concentrations." *Journal of Composite Materials* 21 (1987b): 834-855.

Chang, F. K., and K. Y. Chang. "Post-failure Analysis of Bolted Composite Joints in Tension and Shear-Out Mode Failure." *J of Composite Materials*, no. 21 (1987a): 834-855.

Chen, Hsing-Sung, and Shun-Fa Hwang. "A Fatigue Damage Model for Composite Materials." *Polymer Composites*, 2009: 301-308.

Cheng, J. *Material Modeling of Strain Rate Dependent Polymer and 2D Triaxially Braided.* PhD Thesis, Akron, OH: University of Akron, 2006.

Cho, J., J. Fenner, B. Werner, and I. M. Daniel. "A Constitutive Model for Fiber-reinforced Polymer Composites." *Journal of Composite Materials* 44 (2010): 3133-3150.

Daniel, I. M., and O. Ishai. *Engineering Mechanics of Composite Materials.* New York: Oxford University Press, 2006.

Fouinneteau , M. R. C., and A. K. Pickett . "Shear mechanism modelling of heavy tow braided composites using a meso-mechanical damage model." *Composites: Part A* (Elsevier) 38, no. 11 (2007): 2294-2306.

Gama, Bazle A., Jia-Run Xiao, Md. J. Haque, Chian-Fong Yen, and John W., Jr. Gillespie. *Experimental and Numerical Investigations on Damage and Delamination in Thick Plain Weave S-2 Glass Composites Under Quasi-Static Punch Shear Loading.* Aberdeen Proving Ground: U.S. Army Research Laboratory, 2004.

Ganjiani, M., R. Naghdabadi, and M. Asghari. "An elastoplastic damage-induced anisotropic constitutive model at finite strains." *International Journal of Damage Mechanics* 22 (2012): 499-529.

Goldberg, R.K., et al. "Development of an Orthotropic Elasto-Plastic Generalized Composite Material Model Suitable for Impact Problems." *ASCE J of Aerospace Engineering* 29, no. 4 (July 2016).

—. "Theoretical Development of an Orthotropic Three-Dimensional Elasto-Plastic Generalized Composite Material Model." *13th International LS-DYNA User's Conference.* Detroit, MI, 2014.

Hallquist, J. *LS-DYNA Keyword User's Manual - Volume II: Material Models.* Livermore Software Technology Corporation, 2013.

Harrington, J., and S. D. Rajan. "Test Results from Virtual Testing Software System." Technical Report, School of Sustainable Engineering and the Built Environment, ASU, 2014.

Hoffarth, C., et al. "Verification and Validation of a Three-Dimensional Generalized Composite Material Model." *13th International LS-DYNA User's Conference.* Detroit, MI, 2014.

Holzapfel, Gerhard A., and Thomas C. Gasser. "A viscoelastic model for fiber-reinforced composites at finite strains: Continuum basis, computational aspects and applications." *Computer methods in applied mechanics and engineering* 190 (2001): 4379-4403.

Johnson, A. F., A. K. Pickett, and P. Rozycki. "Computational methods for predicting impact damage in composite structures." *Composites Science and Technology* 61 (2001): 2183-2192.

Khan, A. S., and S. Huang. *Continuum Theory of Plasticity.* New York: John Wiley and Sons, 1995.

Ladeveze, P., and E. Le Dantec. "Damage modeling of the elementary ply for laminated composites." *Compos. Sci. Technol.* (Elsevier Sci. LTD) 43, no. 3 (1992): 257-267.

Lemaitre, J, and R. Desmorat. *Engineering Damage Mechanics: Ductile, Creep and Brittle Failures.* Berlin: Springer, 2005.

Littell, Justin D., Wieslaw K. Binienda, William A. Arnold, Gary D. Roberts, and Robert K. Goldberg. *Effect of Microscopic Damage Events on Static and Ballistic Impact Strength of Triaxial Braid Composites.* Washington: NASA, 2010.

Lourenco, Paulo B., Rene De Borst, and Jan G. Rots. "A Plane Stress Softnening Plasticity Model for Orthotropic Materials." *International Journal for Numerical Methods in Engineering*, 1997: 4033-4057.

Maimi, P., P. P. Camanho, J. A. Mayugo, and C. G. Davila. "A continuum damage model for composite laminates: Part I – Constitutive model." *Mechanics of Materials* 39 (2007): 897-908.

Maimi, P., P. P. Camanho, J. A. Mayugo, and C. G. Davila. "A continuum damage model for composite laminates: Part II – Computational implementation and validation." *Mechanics of Materials* 39 (2007): 909-919.

Matzenmiller, A., J. Lubliner, and R. L. Taylor. "A constitutive model for anisotropic damage in fiber-composites." *Mechanics of Materials* 20 (1995): 125-152.

Micallef, K., A. S. Fallah, P. T. Curtis, and L. A. Louca. "A homogenised continuum constitutive model for visco-plastic deformation of uni-directional composites." *Composite Structures* 99 (2013): 404-418.

Moreira, Luciano P., and Gerard Ferron. "Finite element implementation of an orthotropic plasticity model for sheet metal forming simulations." *Latin American Journal of Solids and Structures* 4 (2007): 149-176.

Ogasawara, T., T. Ishikawa, T. Yokozeki, T. Shiraishi, and N. Watanabe. "Effect of on-axis tensile loading on shear properties of an orthogonal 3D woven SiC/SiC composite." *Comp. Sci. Technol.* 65, no. 15-16 (2005): 2541-2549.

Ozbolt, J., V. Lackovic, and J. Krolo. "Modeling fracture of fiber reinforced polymer." *International Journal of Fracture* 170 (2011): 13-26.

Pinho, S. T., L. Iannucci, and P. Robinson. "Physically-based failure models and criteria for laminated fibre-reinforced composites with emphasis on fibre kinking: Part I: Development." *Composites: Part A* 37 (2006): 63-73.

Pinho, S. T., L. Iannucci, and P. Robinson. "Physically-based failure models and criteria for laminated fibre-reinforced composites with emphasis on fibre kinking: Part II: FE implementation." *Composites: Part A* 37 (2006): 766-777.

Raju, K. S., and J. F. Acosta. *Crashworthiness of Composite Fuselage Structures - Material Dynamic Properties, Phase I.* Washington, DC: U.S. Department of Transportation: Federal Aviation Administration, 2010.

Roberts, Gary D., Robert K. Goldberg, Wieslaw K. Binienda, William A. Arnold, Justin D. Littell, and Lee W. Kohlman. *Characterization of Triaxial Braided Composite Material Properties for Impact Simulation.* NASA/TM—2009-215660, Washington: NASA, 2009.

Salavatian, M., and L. V. Smith. "The effect of transverse damage on the shear response of fiber reinforced laminates." *Comp. Sci. Technol.* (Elsevier) 95 (2014): 44-49.

Santhosh, U., J. Ahmad, G. Ojard, R. Miller, and Y. Gowayed. "Deformation and damage modeling of cermaic matrix composites under multiaxial stresses." *Composites Part B: Engineering* (Elsevier) 90 (2016): 97-106.

Smith, D. L., and M. B. Dow. *Properties of Three Graphite/Toughened Resin Composites.* NASA Technical Paper 3102, September 1991.

Solecki, Roman, and R. Jay Conant. *Advanced Mechanics of Materials.* New York, New York: Oxford University Press, Inc., 2003.

Song, S., A. M. Waas, K. W. Shahwan, O. Faruque, and X. Xiao. "Effects of Matrix Microcracking on the Response of 2D Braided Textile Composites Subjected to Compression Loads." *Journal of Composite Materials* 44, no. 2 (2010): 221-240.

Sun, C. T., and J. L. Chen. "A Simple Flow Rule for Characterizing Nonlinear Behavior of Fiber Composites." *Journal of Composite Materials*, 1989.

Tabiei, Ala, and Jin Wu. "Three-dimensional nonlinear orthotropic finite element material model for wood." *Composite Structures* 50 (2000): 143-149.

Tsai, S. W., and E. M. Wu. "A General Theory of Strength for Anisotropic Materials." *J. Composite Materials* 5 (1971): 58-80.

Van der Meer, Frans P. "Mesolevel Modeling of Failure in Composite Laminates: Constitutive, Kinematic and Algorithmic Aspects." *Archives of Computational Methods in Engineering* 19 (2012): 381-425.

Vaziri, R., M. D. Olson, and D. L. Anderson. "A Plasticity-Based Constitutive Model for Fibre-Reinforced Composite Laminates." *Journal of Composite Materials*, 1991: 512-535.

Wang, C., Z. Liu, B. Xia, S. Duan, X. Nie, and Z. Zhuang. "Development of a new constitutive model considering the shearing effect for anisotropic progressive damage in fiber-reinforced composites." *Composites Part B: Engineering* (Elsevier) 75 (2015): 288-297.

Williams, K. V., R. Vaziri, and A. Poursartip. "A physically based continuum damage mechanics model for thin laminated composite structures." *International Journal of Solids and Structures* 40 (2003): 2267-2300.

Wu, Fuqiang, and WeiXing Yao. "A fatigue damage model of composite materials." *International Journal of Fatigue*, 2010: 134-138.

Xiao, Xinran. "Modeling Energy Absorbtion with a Damage Mechanics Based Composite Material Model." *Journal of Composite Materials* 43 (2009): 427-444.

Xu, Jifeng, Abe Askari, Olaf Weckner, and Stewart Silling. "Peridynamic Analysis of Impact Damage in Composite Laminates." *J. Aerosp. Eng.* 21 (2008): 187-194.

Yang, W. H., and W. W. Feng. "General and Specific Quadratic Yield Functions." *Journal of Composites* 6, no. 1 (1984): 19-21.

Yen, Chian-Fong. "Ballistic Impact Modeling of Composite Materials." *7th International LS-DYNA Users Conference.* 2002. 15-26.

APPENDIX A

THEORY OF ORTHOTROPIC CONSTITUTIVE MATERIAL MODELING

The material model developed in this dissertation is built upon an orthotropic, or orthogonally anisotropic) constitutive material model. The model is general enough to model a large majority of composite (specifically PMC or FRC) materials with three mutually perpendicular (90 degrees apart) material planes. The orthotropic material model is a simplification of the most general anisotropic formulation relating the stresses and strains as

$$\{\sigma\} = [C]\{\varepsilon\}$$

$$
\begin{Bmatrix} \sigma_{11} \\ \sigma_{22} \\ \sigma_{33} \\ \sigma_{23} \\ \sigma_{31} \\ \sigma_{12} \end{Bmatrix} =
\begin{bmatrix}
C_{11} & C_{12} & C_{13} & C_{14} & C_{15} & C_{16} \\
 & C_{22} & C_{23} & C_{24} & C_{25} & C_{26} \\
 & & C_{33} & C_{34} & C_{35} & C_{36} \\
 & & & C_{44} & C_{45} & C_{46} \\
 & Sym & & & C_{55} & C_{56} \\
 & & & & & C_{66}
\end{bmatrix}
\begin{Bmatrix} \varepsilon_{11} \\ \varepsilon_{22} \\ \varepsilon_{33} \\ \gamma_{23} \\ \gamma_{31} \\ \gamma_{12} \end{Bmatrix}
\tag{A.1}
$$

where the stiffness matrix, C, is symmetric due to energy considerations, requiring 21 independent elastic constants (Solecki and Conant 2003). Therefore, assuming two or three mutually perpendicular planes of elastic symmetry, the anisotropic constitutive relationship defined in Eqn. (A.1), can be reduced the orthotropic relationship, with 9 independent elastic constants, defined as

$$
\begin{Bmatrix} \sigma_{11} \\ \sigma_{22} \\ \sigma_{33} \\ \sigma_{23} \\ \sigma_{31} \\ \sigma_{12} \end{Bmatrix} =
\begin{bmatrix}
C_{11} & C_{12} & C_{13} & 0 & 0 & 0 \\
 & C_{22} & C_{23} & 0 & 0 & 0 \\
 & & C_{33} & 0 & 0 & 0 \\
 & & & C_{44} & 0 & 0 \\
 & Sym & & & C_{55} & 0 \\
 & & & & & C_{66}
\end{bmatrix}
\begin{Bmatrix} \varepsilon_{11} \\ \varepsilon_{22} \\ \varepsilon_{33} \\ \gamma_{23} \\ \gamma_{31} \\ \gamma_{12} \end{Bmatrix}
\tag{A.2}
$$

The 9 stiffness matrix coefficients are defined in Eqn. (3.3), with respect to the 6 elastic moduli and 3 elastic Poisson's ratios. The dependencies of these parameters are described below.

APPENDIX B

NONASSOCIATED PLASTICITY

The classical plasticity theory using associated plasticity assumes that the increment of plastic strain be normal to the yield surface, where the plastic potential function is defined as

$$\dot{\boldsymbol{\varepsilon}}^p = \dot{\lambda}\frac{\partial f}{\partial \boldsymbol{\sigma}} \tag{B.1}$$

which is based on Drucker's stability postulate which works well for metals (Khan and Huang 1995). However, associated plasticity is not ideal for most composites with various degrees of plastic anisotropy. For example, the T800/F3900 unidirectional composite described in Chapter 4, exhibits linear elastic behavior, when a unidirectional load is applied in the fiber direction. This would indicate that there is no plastic flow, or strain accumulation with respect to the fiber direction, but the associated plastic potential function in Eqn. (B.1) cannot accommodate this. Thus, nonassociated plasticity is required in creating a generalized composite material model (defined in Eqns. (2.10) and (2.19)), as the flow law coefficents for the nonassociated plastic potential function can be determined through experimentation, described in Chapter 2, to accurately model the anisotropic plastic flow.

Additional proof[†] that non-associated plasticity must be used for a generalized composite model (with a Tsai-Wu yield surface) is shown here: Consider isotropic Tsai-Wu flow rule:

$$f = \sigma_{vm}^2 - A_1 p - A_2 p^2$$

$$\dot{\varepsilon}_{xx}^p \approx \frac{\partial f}{\partial \sigma_{xx}} = 2\sigma_{vm}\frac{3s_{xx}}{2\sigma_{vm}} - A_1\left(-\frac{1}{3}\right) - 2pA_2\left(-\frac{1}{3}\right) = 3s_{xx} + \frac{A_1}{3} + \frac{2pA_2}{3}$$

[†] Provided by Dr. Paul DuBois, private communications, March 2016.

$$\dot{\varepsilon}_{vol}^{p} \approx \frac{\partial f}{\partial \sigma_{xx}} + \frac{\partial f}{\partial \sigma_{yy}} + \frac{\partial f}{\partial \sigma_{zz}} = A_1 + 2pA_2$$

In uniaxial tension

$$\dot{\varepsilon}_{vol}^{p} = \left(1 - 2\nu_p\right)\dot{\varepsilon}_{xx}^{p} \quad and \quad s_{xx} = \sigma_{xx} + p = \frac{2}{3}\sigma_{xx} = -2p$$

$$A_1 + 2pA_2 = \frac{\left(1 - 2\nu_p\right)}{3}\left[9s_{xx} + A_1 + 2pA_2\right]$$

$$A_1 + 2pA_2 = \frac{\left(1 - 2\nu_p\right)}{3}\left[-18p + A_1 + 2pA_2\right]$$

$$IFF \quad A_1 = 0 \Rightarrow 2A_2 = \frac{\left(1 - 2\nu_p\right)}{3}\left[-18 + 2A_2\right] \Rightarrow \nu_p = \frac{9 + 2A_2}{18 - 2A_2}$$

The final equation above shows that the plastic Poisson's ratio can assume any value

which is non-physical.

APPENDIX C

CONSTITUTIVE PARAMETER DEPENDENCIES

The orthotropic stiffness or compliance matrix, shown in Eqn. (3.3), is symmetric with 9 independent coefficients. However, the symmetric indices of the normal components of the matrix are functions of the inverse elastic Poisson's ratios, with the expanded orthotropic compliance matrix defined as

$$\mathbf{S} = \begin{bmatrix} \dfrac{1}{E_{11}} & -\dfrac{v_{21}}{E_{22}} & -\dfrac{v_{31}}{E_{33}} & 0 & 0 & 0 \\[2ex] -\dfrac{v_{12}}{E_{11}} & \dfrac{1}{E_{22}} & -\dfrac{v_{32}}{E_{33}} & 0 & 0 & 0 \\[2ex] -\dfrac{v_{13}}{E_{11}} & -\dfrac{v_{23}}{E_{22}} & \dfrac{1}{E_{33}} & 0 & 0 & 0 \\[2ex] & & & \dfrac{1}{G_{23}} & 0 & 0 \\[2ex] & Sym & & & \dfrac{1}{G_{31}} & 0 \\[2ex] & & & & & \dfrac{1}{G_{12}} \end{bmatrix} \tag{C.1}$$

Therefore, there are a total of 12 elastic parameters, with 6 elastic moduli and 6 elastic Poisson's ratios, but the symmetry of the compliance matrix then produces the following relationships

$$S_{12} = S_{21} = -\frac{v_{21}}{E_{22}} = -\frac{v_{12}}{E_{11}} \implies \boxed{v_{21} = \frac{E_{22}}{E_{11}} v_{12}}$$

$$S_{13} = S_{31} = -\frac{v_{31}}{E_{33}} = -\frac{v_{13}}{E_{11}} \implies \boxed{v_{31} = \frac{E_{33}}{E_{11}} v_{13}} \tag{C.2}$$

$$S_{23} = S_{32} = -\frac{v_{32}}{E_{33}} = -\frac{v_{23}}{E_{22}} \implies \boxed{v_{32} = \frac{E_{33}}{E_{22}} v_{23}}$$

which shows that only 3 of the elastic Poisson's ratios are independent, resulting in the 9 independent elastic parameters for the orthotropic material model.

APPENDIX D

EXAMPLE OF TEMPERATURE AND STRAIN RATE INTERPOLATIONS

This section of the Appendix details the implementation of temperature and strain rate dependencies in the MAT213 deformation model, including input data structure and pertinent added functionalities. Below is a representative table showing the new structure used for the temperature and strain rate dependent input curves (stress-strain), as well as the LS-DYNA keyword definition of the 2D and 3D tables.

Table 13. Example Data Layout

Test (T1)	DEFINE_TABLE_3D (Strain Rate)			DEFINE_TABLE_2D (Temperature)		
Test (T1)	Table 1	SR$_1$		Table 2	Curve 1: T$_1$	
					Curve 2: T$_2$	
					Curve 3: T$_3$	
		SR$_2$		Table 3	Curve 4: T$_1$	
					Curve 5: T$_2$	
					Curve 6: T$_3$	
		SR$_3$		Table 4	Curve 7: T$_1$	
					Curve 8: T$_2$	
					Curve 9: T$_3$	

Table 14. LS-DYNA Table/Curve Definition Card

DEFINE_TABLE_2D/3D								
Card/Var	1	2	3	4	5	6	7	8
1	TBID	SFA	OFFA					
2	VALUE	CURVEID/ TABLEID						

Variable	Description
TBID	Table ID. Tables and Load curves may not share common ID's.

	LS-DYNA allows load curve ID's and table ID's to be used interchangeably.
SFA	Scale factor for VALUE.
OFFA	Offset for VALUE, see explanation below.
VALUE	Load curve will be defined corresponding to this value. The value could be, for example, a strain rate.
CURVEID/TABLEID	Load curve ID (2D); Table ID (3D).

D.1 Interpolation of Stress-Strain Data from Input Curves

Interpolation of stress-strain data that are dependent of strain rate and temperature will be carried out using the *DEFINE_TABLE_3D keyword in LS-DYNA. The concept map is shown in Table 15 where Table_3D is used to store rate dependent data and Table_2D is used to store the corresponding temperature dependent data.

Table 15. Conceptual Map of Strain Rate and Temperature Dependent Data

	DEFINE_TABLE_3D (Strain Rate)		DEFINE_TABLE_2D (Temperature)		
Test (T1)	Table 1	Table 2: SR_1	Table 2	Curve 1: T_1	
				Curve 2: T_2	
				Curve 3: T_3	
		Table 3: SR_2	Table 3	Curve 4: T_1	
				Curve 5: T_2	
				Curve 6: T_3	
		Table 4: SR_3	Table 4	Curve 7: T_1	
				Curve 8: T_2	
				Curve 9: T_3	

Functions to interpolate the ordinate (y-value) of the curve are available as current subroutines in LS-DYNA, e.g. crvval and tabval. The crvval function interpolates the

ordinate value using a given abscissa value of a curve, whereas the tabval function interpolates in a similar fashion but with using values from Table_2D. For example, given a value of effective plastic strain (λ_i) and temperature (T_i), an interpolated yield stress value (σ_{y_i}) is returned from tabval. However, currently there is no function with capabilities to interpolate an ordinate value from Table_3D, i.e. given effective plastic strain (λ_i), temperature (T_i) and strain rate $(\dot{\varepsilon}_i)$, an interpolated yield stress value (σ_{y_i}) cannot be interpolated.

This functionality has been built in a subroutine that is called from MAT213. The algorithm is described in detail below (refer to Table 15 for sample notation).

1. Input: Effective plastic strain (λ_i), temperature (T_i) and strain rate $(\dot{\varepsilon}_i)$ values.
2. Check if $\dot{\varepsilon}_i$ is between the strain rate values from the input as follows (note input to tabval are (λ_i) and (T_i) temperature):
   a. If $\dot{\varepsilon}_i \leq SR_1$, then use SR_1 data.
   b. Else if $SR_1 < \dot{\varepsilon}_i \leq SR_2$, then use tabval with data from Table 2 and Table 3.
   c. Else if $SR_2 \leq \dot{\varepsilon}_i \leq SR_3$, then use tabval with data from Table 3 and Table 4.
   d. Else if $\dot{\varepsilon}_i \geq SR_3$, then use SR_3 data.
   e. The reduced temperature interpolated data is shown in Table 16.

Table 16. Interpolated Values after Temperature Interpolation

	DEFINE_TABLE_3D (Strain Rate)		DEFINE_TABLE_2D (Temperature)
Test (T1)	Table 1	SR$_1$	$\sigma_{y_i}^{SR_1}$
		SR$_2$	$\sigma_{y_i}^{SR_2}$
		SR$_3$	$\sigma_{y_i}^{SR_3}$

3. With the yield stress (σ_{y_i}) values interpolated for the lower and upper bounds of the strain rate (Table 16), the yield stress can then be interpolated between the two strain rates (linearly) as

$$\sigma_{y_i} = \sigma_{y_i}^{SR^-} + \frac{\sigma_{y_i}^{SR^+} - \sigma_{y_i}^{SR^-}}{SR^+ - SR^-}\left(\dot{\varepsilon}_i - SR^-\right)$$

where SR^- and SR^+ are the lower and upper bounds on the strain rate $\dot{\varepsilon}_i$ with

corresponding yield stresses as $\sigma_{y_i}^{SR^-}$ and $\sigma_{y_i}^{SR^+}$.

Numerical Example:

A plot of the 9 curves representing the example data structure from Table 15 is

shown below in Fig. 45, with curves of like temperature having the same color and like

strain rate having the same line type.
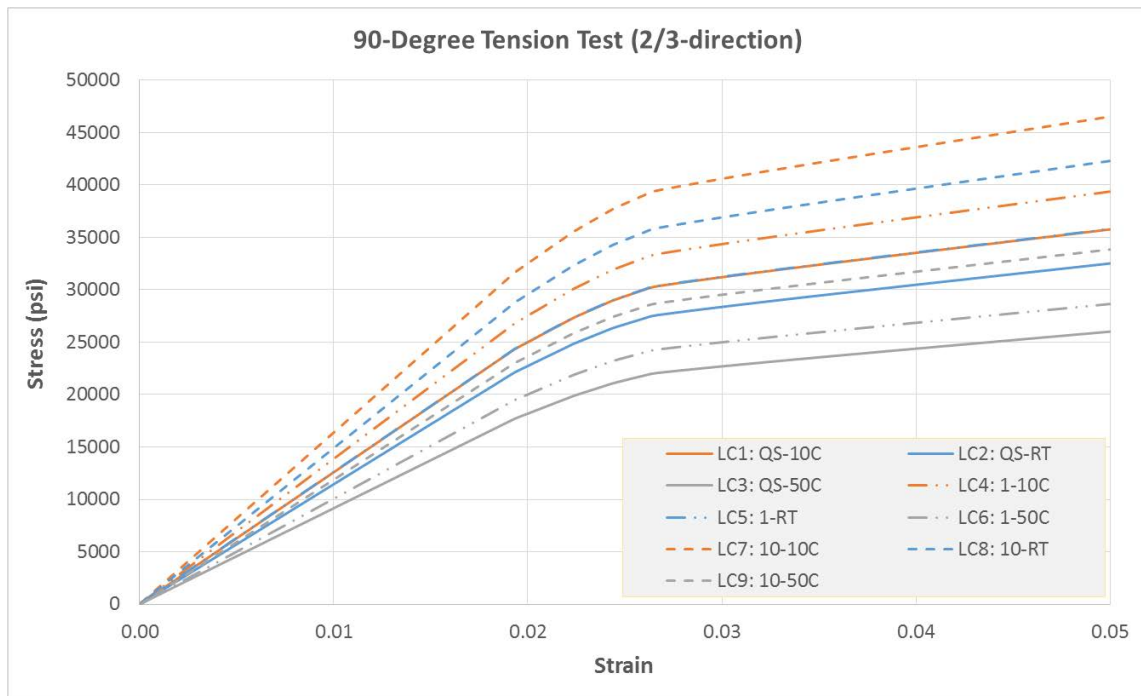
Fig. 45. Stress Strain Curves at Variable Temperature and Strain Rates

Using the data structure from Table 15 and assuming an effective plastic strain value of $\lambda_i = 0.04$, temperature of $T_i = 40^o C$ and strain rate of $\dot{\varepsilon}_i = 4/s$, the values of each curve at this value of effective plastic strain are shown in Table 17 below.

Table 17. Example Map of Strain Rate and Temperature Dependent Data

Test (T1)	DEFINE_TABLE_3D (Strain Rate)		DEFINE_TABLE_2D (Temperature)	
	Table 1	Table 2: 10⁻³/s	Table 2	Curve 1 (10C) : 33,536
				Curve 2 (21C): 30,487
				Curve 3 (50C): 24,390
		Table 3: 1/s	Table 3	Curve 4 (10C): 36,890
				Curve 5 (21C): 33,536
				Curve 6 (50C): 26,829
		Table 4: 10/s	Table 4	Curve 7 (10C): 43,597
				Curve 8 (21C): 39,633
				Curve 9 (50C): 31,707

The function tabval in LS-DYNA utilizes the effective plastic strain and temperature values to interpolate the corresponding yield stresses from the lower and upper bounds of the strain rate (Table 17 and Table 18), which are shown in Table 18 below.

Table 18. Example Interpolated Values after Temperature Interpolation

Test (T1)	DEFINE_TABLE_3D (Strain Rate)		DEFINE_TABLE_2D (Temperature)
	Table 1	1/s	29,142
		10/s	34,440

Finally, the yield stress values obtained from tabval (interpolation for temperature and effective plastic strain of curves) can be used to interpolate between the lower and

upper bound strain rates for $\dot{\varepsilon}_i = 4/s$, which results in a final yield stress value of

$$\sigma_{y_i}\left(0.04, 40^o\,\text{C}, 4/\text{s}\right) = \mathbf{30,908\ psi}\,.$$

D.2 Interpolation of Modulus from Stress-Strain Data from Input Curves

The addition of temperature and strain rate dependency in MAT213 required the addition of 3D interpolation to determine the yield stress from the input stress strain curves. This also requires the interpolation of the elastic modulus for the 12 directions given a temperature and strain rate. The first step to determining the elastic modulus for a specific curve of one of the directions is to define the initial yield strain which can then be used to determine the corresponding initial yield stress value from the input stress strain curve. The modulus is then calculated as this initial yield stress divided by the defined initial yield strain value. Due to the multiple stress-strain curves associated with each direction, the number of inputs for the individual initial plastic strain values is equal to the number of curves, which can increase quickly with additional temperatures and strain rates. Thus, it is not possible to have all the initial yield strain values as direct input in the material card, so the values will be defined using a curve (*Define_Curve) with the abscissa and ordinate values being the stress-strain curve ID and the corresponding initial yield strain, respectively. This curve can then be used to convert the curves from true strain to effective plastic strain, as well as determining the elastic modulus. An example structure for this table, following the same data from above is shown below in Table 19.

133

Table 19. Input Curve Containing Initial Strain Rate Values

Load Curve	Initial Plastic Strain
LC1	ε_{y0}^{LC1}
LC2	ε_{y0}^{LC2}
LC3	ε_{y0}^{LC3}
LC4	ε_{y0}^{LC4}
LC5	ε_{y0}^{LC5}
LC6	ε_{y0}^{LC6}
LC7	ε_{y0}^{LC7}
LC8	ε_{y0}^{LC8}
LC9	ε_{y0}^{LC8}

In order to interpolate the elastic modulus for a given temperature and strain rate, the 3D table containing the stress-strain data with respect to temperature, Table 15, and strain rate is utilized along with the initial plastic strain curve, Table 19.

The elastic modulus interpolation is implemented in a subroutine that will be called from MAT213. The proposed algorithm is described in detail below (refer to Tables A and E for sample notation).

1. Input: Plastic strain curve ID, temperature (T_i) and strain rate $(\dot{\varepsilon}_i)$ values.
2. Check if $\dot{\varepsilon}_i$ and T_i is between the strain rate and temperature values from the input as follows:
    a. If $\dot{\varepsilon}_i \leq SR_1$, then use SR_1 data.
        i. If $T_i \leq T_1$, then use T_1 data to calculate the modulus.
        ii. Else if $T_1 < T_i \leq T_2$, then interpolate modulus with data from Curve 1 and Curve 2.
        iii. Else if $T_2 \leq T_i \leq T_3$, then interpolate modulus with data from Curve 2 and Table 3.
        iv. Else if $T_i \geq T_3$, then use T_3 data to calculate the modulus.
    b. Else if $SR_1 < \dot{\varepsilon}_i \leq SR_2$, then interpolate with data from Table 2 and Table 3 using the same temperature checks as steps a.i-a.iv above.

c. Else if $SR_2 \leq \dot{\varepsilon}_i \leq SR_3$, then interpolate with data from Table 3 and Table 4 using the same temperature checks as steps a.i-a.iv above.

d. Else if $\dot{\varepsilon}_i \geq SR_3$, then use SR_3 data using the same temperature checks as steps a.i-a.iv above.

e. The reduced temperature interpolated data is shown in Table 20.

Table 20. Interpolated Modulus Values after Temperature Interpolation

		DEFINE_TABLE_3D (Strain Rate)	DEFINE_TABLE_2D (Temperature)
Test (T1)	Table 1	SR_1	E^{SR_1}
		SR_2	E^{SR_2}
		SR_3	E^{SR_3}

3. With the elastic modulus (E) values interpolated for the lower and upper bounds of the strain rate (Table 20), the elastic modulus can then be interpolated between the two strain rates (linearly) as

$$E = E^{SR^-} + \frac{E^{SR^+} - E^{SR^-}}{SR^+ - SR^-}\left(\dot{\varepsilon}_i - SR^-\right)$$

where SR^- and SR^+ are the lower and upper bounds on the strain rate $\dot{\varepsilon}_i$ with

corresponding elastic modulus as E^{SR^-} and E^{SR^+}.

Numerical Example:

The same data from the yield stress interpolation is used here, with a plot of the 9

curves representing the example data structure from Table 15 is shown below in Fig. 1,

with curves of like temperature having the same color and like strain rate having the same

line type. Using the data structure from Table 15 and assuming the initial plastic strain

values are 0.02, a temperature of $T_i = 40^o C$ and strain rate of $\dot{\varepsilon}_i = 4/s$, the elastic

modulus values of each curve are shown in Table 21 below.

135

Table 21. Example Map of Strain Rate and Temperature Dependent Data (Modulus)

	DEFINE_TABLE_3D (Strain Rate)		DEFINE_TABLE_2D (Temperature)	
Test (T1)	Table 1	Table 2: 10^{-3}/s	Table 2	Curve 1 (10C): 1,250,663
				Curve 2 (21C): 1,136,966
				Curve 3 (50C): 909,573
		Table 3: 1/s	Table 3	Curve 4 (10C): 1,375729
				Curve 5 (21C): 1,250,663
				Curve 6 (50C): 1,000,530
		Table 4: 10/s	Table 4	Curve 7 (10C): 1,625,861
				Curve 8 (21C): 1,478,056
				Curve 9 (50C): 1,182,445

Utilizing the interpolation algorithm outlined above, the elastic modulus values after temperature interpolation are shown below in Table 22.

Table 22. Example Interpolated Values after Temperature Interpolation

	DEFINE_TABLE_3D (Strain Rate)		DEFINE_TABLE_2D (Temperature)
Test (T1)	Table 1	1/s	1,086,783
		10/s	1,284,280

Finally, the elastic modulus values obtained (interpolation for temperature and effective plastic strain of curves) can be used to interpolate between the lower and upper bound strain rates for $\dot{\varepsilon}_i = 4/s$, which results in a final elastic modulus value of

$$E_{22}\left(40^o\,\text{C}, 4/\text{s}\right) = \mathbf{1,152,648\ psi}\,.$$

D.3 Verification Tests for Temperature and Strain Rate Dependencies in MAT213

Verification of the temperature and strain rate dependent functionality in
MAT213 was initially performed using the tension 2-direction verification test used in
the deformation model, with the original input curves as well as scaled curves to
represent temperature and strain rate dependent data. The updated user input for the
model is shown in Table 23 below, with the original input variables equal to those used in
the deformation model.

Table 23. Example Interpolated Values after Temperature Interpolation

Card/Var	1	2	3	4	5	6	7	8
1	MID	RO	EA	EB	EC	PRBA	PRCA	PRCB
2	GAB	GCB	GCA	KFAIL	AOPT	MACF		
3	XP	YP	ZP	A1	A2	A3		
4	V1	V2	V3	D1	D2	D3	BETA	
5								
6	PR12	PR23	PR13	H11	H22	H33	G12	G23
7	G13	G44	G55	G66	LT1	LT2	LT3	LT4
8	LT5	LT6	LT7	LT8	LT9	LT10	LT11	LT12
9	YSC	TEMP						
10								
11								

```
*MAT_AWG_COMPOSITE_DAMAGE
$#     mid         ro         Ea         Eb         Ec       PRba       PRca       PRcb
       213  1.4570E-4    21.83E6    1.145E6    1.145E6   0.013847   0.013847     0.3792
$#     Gab        Gbc        Gca      Kfail       AOPT       MACF
  0.5796E6   0.3243E6   0.5796E6   0.000000      2.000      0.000
$#      xp         yp         zp         a1         a2         a3
     0.000      0.000      0.000   1.000000  -0.577350      0.000
$#      v1         v2         v3         d1         d2         d3       beta
     0.000      0.000      0.000   1.000000   1.732050      0.000      0.000
$#      sc         xt         yt         yc       alph         sn        syz        szx
  1.000000   0.000000   0.000000   0.000000   0.000000   0.000000   0.000000   0.000000
$#    pr12       pr23       pr13        G11        G22        G33        G12        G23
  0.264000   0.379200   0.264000    0.00000    1.00000    1.00000   0.000000   -0.66840
$#     G13        G44        G55        G66        LT1        LT2        LT3        LT4
  0.000000    7.70000    6.10000    7.70000       1001       1002       1003       1004
$#     LT5        LT6        LT7        LT8        LT9       LT10       LT11       LT12
      1005       1006       1007       1008       1009       1010       1011       1012
$#     YSC       TEMP
       100       36.0
```

Verification Test 1: Temperature and Strain Rate Independent (Same as Before)

In order to mimic the original verification test with the new temperature and rate dependent input, the same quasi-static, room temperature data is used. However, LS-DYNA requires a minimum of two curves in the 2D table definition, but only one table in the 3D table definition. Thus, a minimum of two curves must be defined for each of the 12 input test cases; which, in the case of temperature and strain rate independent data, will just be two identical copies. A sample input data defined for this case is shown below, note the actual curve data is not shown.

```
*DEFINE_CURVE
$$ Curve of initial yield strain values
$$ a-Curve ID's    o-Initial Yield Strain Values
$#    lcid      sidr       sfa       sfo      offa      offo    dattyp
       100         0     0.000     0.000     0.000     0.000         0
$#               a1                  o1
$Strain Rate:0.001; Temp:21
                   1               1.000
                   2               0.020
                   3               0.020
                   4               1.000
                   5               0.020
                   6               0.020
                   7               0.006
                   8             0.01210
                   9               0.006
                  10             0.00898
                  11               0.020
                  12             0.00898
$ Strain Rate:0.001; Temp:50
                  13               1.000
                  14               0.020
                  15               0.020
                  16               1.000
                  17               0.020
                  18               0.020
                  19               0.006
                  20             0.01210
                  21               0.006
                  22             0.00898
                  23               0.020
                  24             0.00898
$
*DEFINE_TABLE_3D
```

138

```
$$ T2
$$ Strain Rate Values
$#    tbid       sfa      offa
     1002         0     0.000
$#            value            tableid
             0.001               1014
*DEFINE_TABLE
$$ Temperature Values at 0.001
$#    tbid       sfa      offa
     1014         0     0.000
$#            value
                21
                50
*DEFINE_CURVE
$$ Stress Strain Curve for 0.001,21
$#    lcid      sidr       sfa       sfo      offa      offo    dattyp
         2         0     0.000     0.000     0.000     0.000        0$#
               a1                   o1
              0.0                  0.0
              1.0                  0.0
*DEFINE_CURVE
$$ Stress Strain Curve for 0.001,50
$#    lcid      sidr       sfa       sfo      offa      offo    dattyp
        14         0     0.000     0.000     0.000     0.000        0$#
               a1                   o1
              0.0                  0.0
              1.0                  0.0
```

The results for 2-direction tension test with temperature and strain rate
independent data are shown in Fig. 46. The simulation was run with the same parameters
as the original 2-direction tension verification test, resulting in a strain rate of 0.0625 1/s
and an arbitrary constant temperature of 36° C. These results match the quasi-static,
room temperature input curve, which was copied as input for 21° C and 50° C degrees.

Fig. 46. Temperature and Strain Rate Independent Verification Test

Verification Test 2: Temperature Independent with 2 Strain Rates

The second varication test performed, included strain dependent data defined at two strain rates with no effect from temperature. The same quasi-static, room temperature 2-direction tension stress-strain curve was scaled to demonstrate strain rate dependent data. To represent strain dependent only data, two strain rate values of 0.001 and 0.1 1/s were used with a scale factor of 1.1 applied to the base curve, used for the latter. Like the first verification test, a minimum of two curves must be defined for each of the 12 input test cases, but with an additional strain rate, a total of 4 curves are defined for each test case. Thus the 2 curves associated with the strain rate of 0.1 are copies of the base curve scaled by a factor of 1.1, whereas the 2 curves representing a strain rate of 0.001 are unmodified copies of the base curve. A sample input data defined for this case is shown below, note the actual curve data is not shown.

140

```
*DEFINE_CURVE
$$ Curve of initial yield strain values
$$ a-Curve ID's    o-Initial Yield Strain Values
$#   lcid     sidr      sfa      sfo     offa     offo   dattyp
      100        0    0.000    0.000    0.000    0.000        0
$#               a1                o1
$Strain Rate:0.001; Temp:21
                  1             1.000
                  2             0.020
                  3             0.020
                  4             1.000
                  5             0.020
                  6             0.020
                  7             0.006
                  8           0.01210
                  9             0.006
                 10           0.00898
                 11             0.020
                 12           0.00898
$ Strain Rate:0.001; Temp:50
                 13             1.000
                 14             0.020
                 15             0.020
                 16             1.000
                 17             0.020
                 18             0.020
                 19             0.006
                 20           0.01210
                 21             0.006
                 22           0.00898
                 23             0.020
                 24           0.00898
$ T2/T4 Strain Rate:0.1; Temp:21/50
                 25              0.02
                 26              0.02
                 27              0.02
                 28              0.02
$
*DEFINE_TABLE_3D
$$ T2
$$ Strain Rate Values
$#   tbid      sfa     offa
     1002        0    0.000
$#             value           tableid
              0.001              1014
                0.1              1025
*DEFINE_TABLE
$$ Temperature Values at 0.001
$#   tbid      sfa     offa
     1014        0    0.000
$#             value
                 21
                 50
*DEFINE_CURVE
```

```
$$ Stress Strain Curve for 0.001,21
$#    lcid      sidr       sfa        sfo       offa       offo     dattyp
         2         0     0.000      0.000      0.000      0.000         0$#
                    a1                    o1
                   0.0                   0.0
                   1.0                   0.0
*DEFINE_CURVE
$$ Stress Strain Curve for 0.001,50
$#    lcid      sidr       sfa        sfo       offa       offo     dattyp
        14         0     0.000      0.000      0.000      0.000         0$#
                    a1                    o1
                   0.0                   0.0
                   1.0                   0.0
*DEFINE_TABLE
$$ Temperature Values at 0.001
$#    tbid       sfa       offa
      1025         0     0.000
$#            value
                   21
                   50
*DEFINE_CURVE
$$ Stress Strain Curve for 0.1,21
$#    lcid      sidr       sfa        sfo       offa       offo     dattyp
        25         0     0.000      1.100      0.000      0.000         0$#
                    a1                    o1
                   0.0                   0.0
                   1.0                   0.0
*DEFINE_CURVE
$$ Stress Strain Curve for 0.1,50
$#    lcid      sidr       sfa        sfo       offa       offo     dattyp
        26         0     0.000      1.100      0.000      0.000         0$#
                    a1                    o1
                   0.0                   0.0
                   1.0                   0.0
```

The results for 2-direction tension test with strain rate only dependent data are shown in Fig. 47. The simulation was run with the same parameters as the original 2-direction tension verification test, resulting in a strain rate of 0.0625 1/s and an arbitrary constant temperature of 36° C. The simulated curve is correctly interpolated between the quasi-static and increased 1.1 1/s strain rate curves.
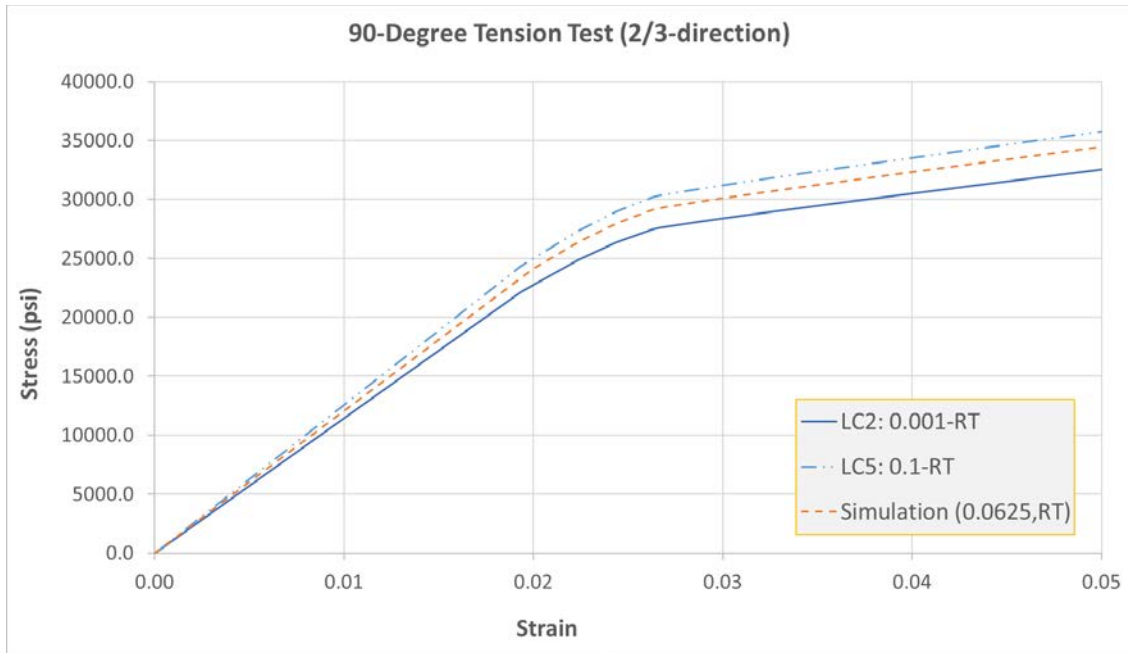
Fig. 47. Verification Test with Two Strain Rates and Independent of Temperature

Verification Test 3: Strain Rate Independent with 2 Temperatures

The third verification test performed included temperature dependent data defined at two temperatures with no effect from strain rate. The same input curves as in the first verification test (2 input curves per test case) were used, but the curve defined for 50° C was scaled by 0.8 for the base 2-direction tension curve. A sample input data defined for this case is shown below, note the actual curve data is not shown.

```
*DEFINE_TABLE_3D
$$ T2
$$ Strain Rate Values
$#    tbid        sfa       offa
      1002          0      0.000
$#              value           tableid
              0.001              1014
*DEFINE_TABLE
$$ Temperature Values at 0.001
$#    tbid        sfa       offa
      1014          0      0.000
$#              value
```

```
                 21
                 50
*DEFINE_CURVE
$$ Stress Strain Curve for 0.001,21
$#    lcid      sidr       sfa       sfo      offa      offo    dattyp
         2         0     0.000     0.000     0.000     0.000        0$#
                   a1                  o1
                  0.0                 0.0
                  1.0                 0.0
*DEFINE_CURVE
$$ Stress Strain Curve for 0.001,50
$#    lcid      sidr       sfa       sfo      offa      offo    dattyp
        14         0     0.000     0.800     0.000     0.000        0$#
                   a1                  o1
                  0.0                 0.0
                  1.0                 0.0
```

The results for 2-direction tension test with temperature only dependent data are shown in Fig. 48. The simulation was run with the same parameters as the original 2-direction tension verification test, with a constant temperature of 36° C defined. The simulated curve is correctly interpolated between the 21° C (RT) and increased 50° C temperature curves.
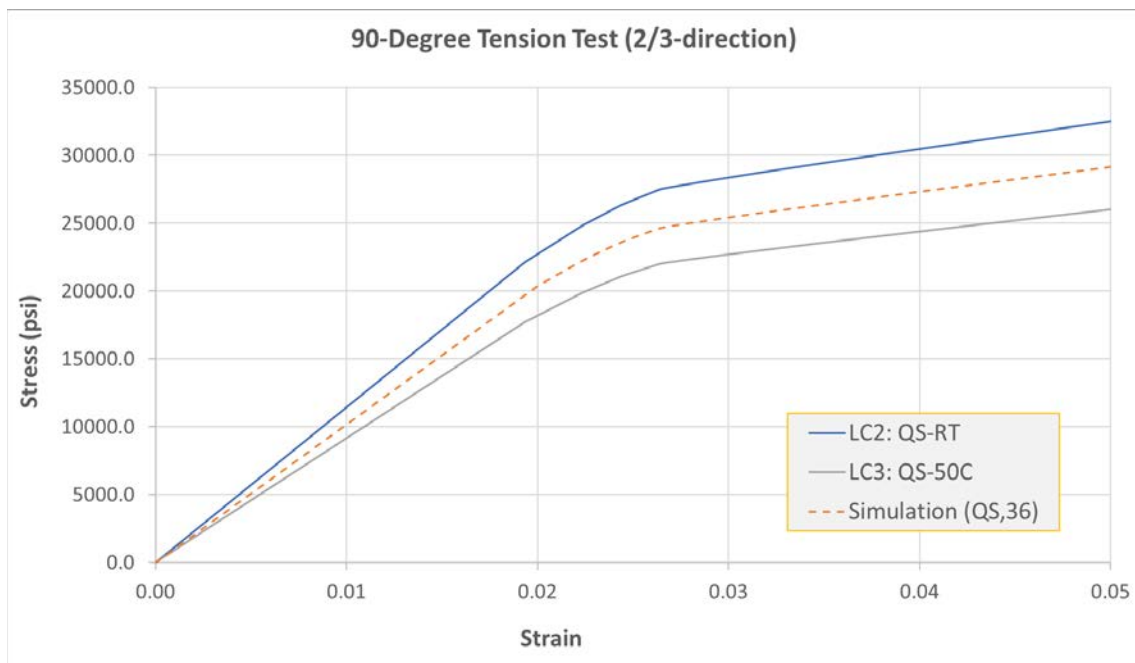

Fig. 48. Verification Test with Two Temperatures and Independent of Strain Rate

144

Verification Test 4: 2 Strain Rate with 2 Temperatures

The final verification test performed included both temperature and strain

dependent data defined at two temperatures and two strain rates. The same input curves

as in the second verification test (4 input curves per test case) were used, but the curves

defined for 50° C were scaled by 0.8 and the curves defined for a strain rate of 0.1 were

scaled by 1.1, from the base 2-direction tension curve. A sample input data defined for

this case is shown below, note the actual curve data is not shown.

```
*DEFINE_TABLE_3D
$$ T2
$$ Strain Rate Values
$#    tbid        sfa       offa
      1002          0      0.000
$#              value             tableid
              0.001                 1014
                0.1                 1025
*DEFINE_TABLE
$$ Temperature Values at 0.001
$#    tbid        sfa       offa
      1014          0      0.000
$#              value
                 21
                 50
*DEFINE_CURVE
$$ Stress Strain Curve for 0.001,21
$#    lcid       sidr        sfa        sfo       offa       offo     dattyp
         2          0      0.000      0.000      0.000      0.000         0$#
                   a1                   o1
                  0.0                  0.0
                  1.0                  0.0
*DEFINE_CURVE
$$ Stress Strain Curve for 0.001,50
$#    lcid       sidr        sfa        sfo       offa       offo     dattyp
        14          0      0.000      0.800      0.000      0.000         0$#
                   a1                   o1
                  0.0                  0.0
                  1.0                  0.0
*DEFINE_TABLE
$$ Temperature Values at 0.001
$#    tbid        sfa       offa
      1025          0      0.000
$#              value
```

```
                    21
                    50
*DEFINE_CURVE
$$ Stress Strain Curve for 0.1,21
$#    lcid      sidr        sfa        sfo       offa       offo     dattyp
        25         0      0.000      1.100      0.000      0.000         0$#
                    a1                   o1
                   0.0                  0.0
                   1.0                  0.0
*DEFINE_CURVE
$$ Stress Strain Curve for 0.1,50
$#    lcid      sidr        sfa        sfo       offa       offo     dattyp
        26         0      0.000      0.880      0.000      0.000         0$#
                    a1                   o1
                   0.0                  0.0
                   1.0                  0.0
```

The results for 2-direction tension test with both temperature and strain rate

dependent data are shown in Fig. 49. The simulation was run with the same parameters

as the original 2-direction tension verification test, resulting in a strain rate of 0.0625 1/s

with a constant temperature of 36° C defined. The simulated curve is correctly

interpolated between the coupled temperature (21° C (RT) and 50° C) and strain rate
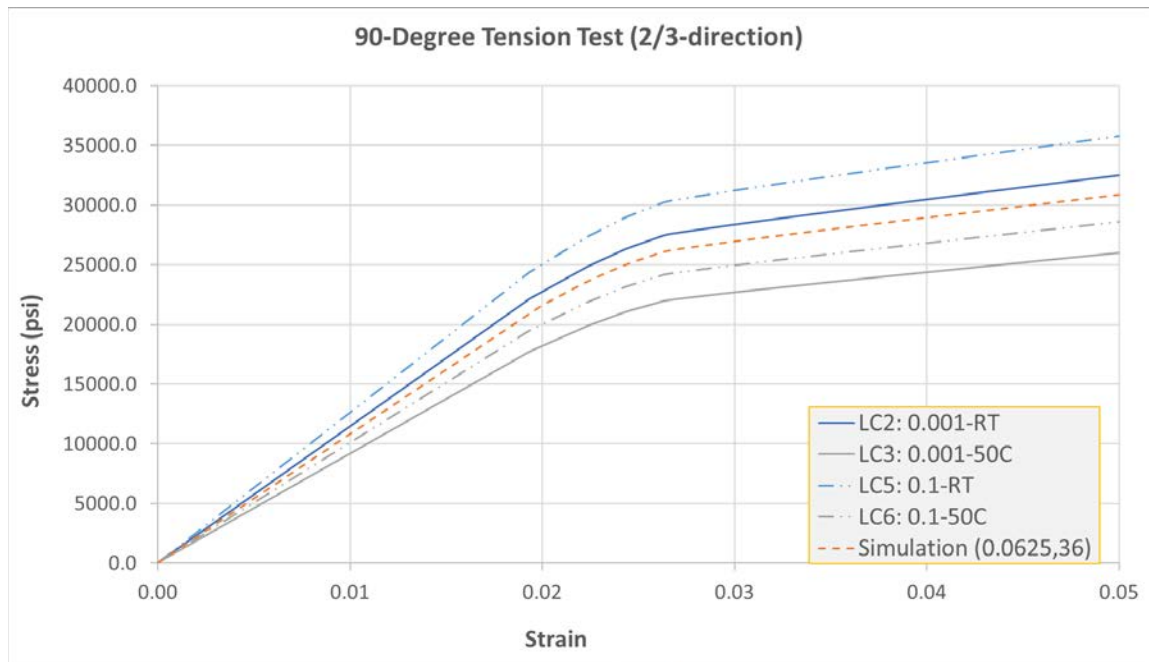
dependent (0.001 and 0.1 1/s) input curves.

Fig. 49. Verification Test with Two Temperatures and Two Strain Rates